Heat Assisted Magnetic Recording using Exchange Bias

Manginas Georgios

Master by Research

University of York

Physics Department

December 2019

Abstract

In this work a study of a new paradigm for the recording layer in a heat assisted magnetic recording (HAMR) media based on the use of exchange bias is presented. Exchange bias occurs when an antiferromagnetic (AF) layer such as IrMn is grown in contact with a ferromagnetic (FM) layer, which in our case happens to be also the recording layer resulting in a hysteresis loop shifted along the field axis. The FM layer when magnetised, serves to align the AF layer in the direction required to store the information and then provides a readout signal indicating in which direction the AF layer is oriented. Hence in a complex way the "recording layer" is actually part of the read/write head. By achieving spin alignment of the IrMn such that the spins are aligned perpendicular to the plane of the film, the required perpendicular exchange bias can be induced for information storage in the AF layer. A series of 14 set of samples have been prepared and evaluated to determine the optimised structure.

A segregated CoCrPt-SiO_2 sample was used as the recording layer from a pressed powder target in a HiTUS deposition system. Several seed layers were tested such as Ru, Pt and Cu for their ability to favour perpendicular anisotropy in double or combined form of 8 nm and 12 nm thicknesses respectively. They were deposited using 3 mTorr and 30 mTorr process pressure. XRD and XRR techniques were used in order to evaluate the structural properties of the multilayers. Alternating gradient force magnetometry and vibrating sample magnetometry at room and low temperature measurements were also used to characterise their magnetic response.

The key feature of this media is that the recorded information is impossible to be erased by a demagnetising field. In order to achieve this requirement, the hysteresis loop has to be completely shifted to a negative field. In the current study a small shift up to H_{ex}=325 Oe was achieved at 100K without the need of a Co interlayer. A complementary attempt was made to induce the desired exchange bias by depositing an ultrathin (0.8 nm) Co interlayer above a Pt and a Ru seed layer resulting in an exchange field of H_{ex}=40 Oe. In addition, mixed seed layers were deposited using Ru/Pt and Ru/Cu with the first case showing the most promising results of squareness around 70% and coercivities of 1800 Oe. Because of the fact that loop shifts were observed at 100K, further work is required to optimise those structures.

Table of Contents

List of figures

List of Tables

Acknowledgements

For the completion of this work a certain amount of persistence was needed, which would never be achieved without the constant support from my family and especially my father Konstantinos, my mother Evangelia and my brother John to whom I owe the most. I would also like to thank my supervisor Dr Gonzalo Vallejo Fernandez for his guidance through the project and Dr Kevin O'Grady for his valuable advice and notifications. I would also like to thank the members of the Magnetics group of the University of York with their support and guidance through the instruments' operation. Moreover, the support of 2nd TAP member Dr Roddy Vann was decisive and important. Finally, I would like to thank the examiners Prof Atsufumi Hirohata and Prof Sam Ladak for their comments and corrections.

Authors Declaration

I declare that this thesis is a presentation of original work and I am the sole author. This work has not previously been presented for an award at this, or any other, University. All sources are acknowledged as References.

Signed:

Manginas Georgios

1. Introduction

1.1 Background and motivation

The current density of conventional Hard Disk Drives (HDD) using Perpendicular Recording Media (PRM) is about 1 TB/inch^2 and is approaching its limit [1]. As a result, further solutions are needed in order to increase the storage capacity. In conventional magnetic recording media, the areal data density is limited by the thermal loss effect which means that when the volume of the grains is reduced, the magnetisation of a particle can reverse due to the demagnetising field of the bit and even from neighbouring bits despite of the absence of an external magnetic field. This fact sets a limit on the size of the ferromagnetic particles that can be used in the storage media called the superparamagnetic limit. Below this limit the particles appear to behave as paramagnetic with their magnetisation appearing to be in average zero but with much higher susceptibility than the usual paramagnetic materials. In order to improve the thermal stability higher anisotropic materials must be used but this means that higher writing fields are needed to reverse the magnetisation of the bits. In order to reduce the writing field of the reading head several advanced recording technologies have been proposed such as bit patterned media (BPM), heat assisted magnetic recording (HAMR) and microwave assisted magnetic recording (MAMR).

The first HAMR devices were introduced in the market in 2019 with 16 TB storage capacity, with 20 TB expected in 2020 [2]. The principle of HAMR is that a laser delivers heat pulses to the surface of the recording media with grains oriented in the perpendicular direction like in the depiction of figure 1.1. By heating the disc near the Curie temperature of the recording layer one can reduce the anisotropy of the material so that a conventional write head can switch the magnetisation direction of the grains enabling the write process. This technology enables the use of even higher anisotropic recording media like FePt which means smaller bit sizes and higher recording densities can be achieved.

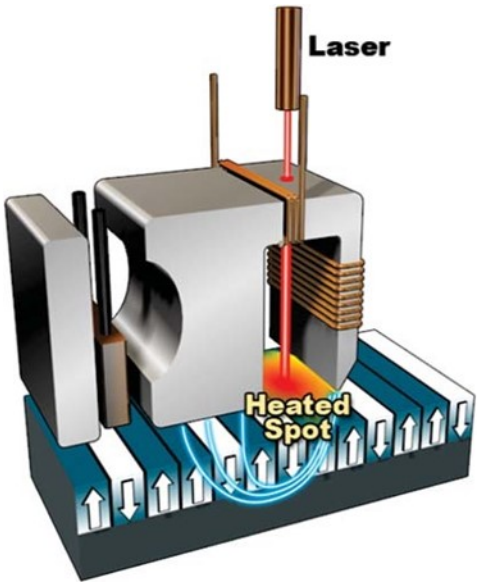

Figure 1.1 : Principle of operation of HAMR depicting the laser beam hitting the surface of the recording layer and the magnetic field generated by the head which switches the bits [3]

Although a simple technology in principle, there are many technical challenges that have prevented the commercialisation of HAMR to date, many of which are directly and indirectly associated with the use of FePt as a recording layer. In particular, it is very difficult to fully crystallise some of the nanometre-sized grains that are present in the film (<4 nm), in order to achieve recording densities beyond 3 Tbit/in^2 [4]. It has been recently shown that for a film consisting of 5 nm grains the proportion of thermally written-in errors can be as large as 12%.[5] This happens because of the reduced magnetisation of the grains during the high temperature writing process and the external thermal energy generated in the media. In order to achieve a recording density of 4 Tbit/in^2 grains as small as 4.3 nm are needed [1]. Another key challenge in the implementation of HAMR is to develop a near-field transducer capable of delivering 50 μW into a spot diameter of 30 nm. Such high-power densities, 7x10^{10} W/m^2, are needed to reach the right temperature to switch the FePt grains.

Regarding the storage media, perpendicular recording using CoCrPt is more attractive for many reasons. First of all it is inherently more stable as adjacent bits reinforce magnetisation with typical loop and formation like in figure 1.2, while in FePt the demagnetising field of neighbouring bits can reverse the magnetisation. Secondly there is a larger stray field than conventional perpendicular media to read and finally it is easier to generate perpendicular write field. The characteristics of the CoCrPt alloys currently used are

the high uniaxial anisotropy from the hcp (hexagonal) crystal structure with easy direction along the c-axis, the thin film thickness that is typically 15-20 nm thick, the physical segregation that can be achieved due to inter-granular non-magnetic Cr rich alloy and oxides and the grain size which is typically smaller than 10 nm. As grains and consequently bits get smaller, to achieve thermal stability of the bits, higher anisotropy is needed. But this means then that higher fields are required to write the information. To be able to reduce this writing field then something else needs to be added to the recording layer. This could be achieved by exchange coupling to a magnetically softer underlayer.

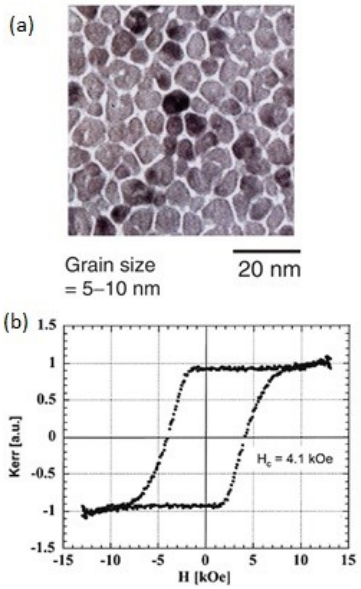

Figure 1.2: Schematic illustration of CoCrPt perpendicular segregated media (a) and its characteristic Kerr loop perpendicular to the plane (b) [6]

One way to do that is using the exchange bias which results in a unidirectional anisotropy being induced to the ferromagnetic layer when it is grown in contact with an antiferromagnetic (AF) layer. The hysteresis loop is then shifted so that both coercivities can lie in negative fields. For this system the application of a large negative field cannot demagnetise the system. In the case of a thermally induced reversal the loop would be shifted completely to a positive field. In this way it is much more difficult to lose the information thermally and the information is stored in the antiferromagnet.

To achieve a proof of principle of a perpendicular medium with exchange bias it is necessary to achieve several goals. Firstly, is to show that it is possible to induce exchange

coupling between the normal AF alloy like IrMn to a CoCrPt – SiO_2 medium. The second requirement is that the texture of the IrMn (111) planes is oriented in the perpendicular direction. Finally that the segregation of the CoCrPt is achieved by the SiO_2 by depositing the right seed layers with the appropriate thicknesses and deposition pressures [7]. There are several advantages to this approach which include an easy implementation of the required technology, lower power consumption, a significantly lower writing temperature of the order of 500K, minimally thermally written-in errors which result at high magnetisation at the writing temperature and that no phase transformation is required which means that small grains are not an issue.

1.2 Objectives

The main aim of this project was to optimise the multilayer structure and produce a system that can act as a recording medium. In order to achieve this, the main milestone that had to be achieved during the MRes year, was the optimisation of the seed layer. As mentioned earlier, this initial structure does not result in segregated films. Segregated CoCrPt-SiO_2 grains are usually achieved via the use of a dual Ru seed layer. An initial 8 nm layer is deposited at low pressure followed by a high pressure, 10 times higher, 12 nm layer. Hence the intention was to grow a voided Ru layer but then use further seed layers which would hopefully grow in a voided structure to give the necessary orientation in the stack and cause the segregation on the recording layer. Different combination of materials as seed layers were also tested to see if the desirable squareness and coercivity, could be achieved. A range of deposition pressures for these layers have been evaluated in order to try and maintain the spatial segregation of the grains. These multilayers were evaluated using X-ray diffraction (XRD) and magnetic measurements where a significant exchange bias is achieved at room temperature. Segregation of the solute SiO_2 to grain boundaries in a solid produces a section of material with a discrete composition and its own set of properties that can have important effects on the overall properties of the material. Equilibrium segregation is a process associated with the lattice disorder at interfaces, where there are sites of energy different from those within the lattice at which the solute atoms can deposit themselves. The equilibrium segregation is so termed because the solute atoms segregate themselves to the interface or surface in accordance with the statistics of thermodynamics in order to minimize

the overall free energy of the system [8]. Non-equilibrium segregation, first theorized by Westbrook in 1964, is a process that occurs as a result of solutes coupling to vacancies which are moving to grain boundary sources or sinks during quenching or application of stress. It can also occur as a result of solute pile-up at a moving interface. There are two main features of non-equilibrium segregation, by which it is most easily distinguished from equilibrium segregation. In the non-equilibrium effect, the magnitude of the segregation increases with increasing temperature and the alloy can be homogenized without further quenching because its lowest energy state corresponds to a uniform solute distribution [8]. In contrast, the equilibrium segregated state, by definition, is the lowest energy state in a system that exhibits equilibrium segregation, and the extent of the segregation effect decreases with increasing temperature. Figure 1.3 illustrates the equilibrium process which results in a structure similar to that of bricks and mortar as grains are separated by the solute SiO_2.

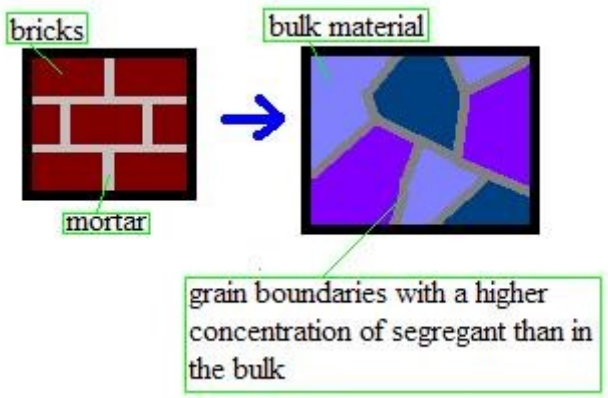

Figure 1.3: Illustration of what segregation of the SiO_2 solute in grain boundaries looks like and parallelization of the formation with the structure of bricks and mortar.[8]

2. Theory

2.1 Origin of magnetic moments

The microscopic origin of magnetism in materials lies in the existence of atomic magnetic dipoles due to the circular currents at the atomic level resulting from the rotational movements of uncontrolled electrons both around the atoms (orbits) and around themselves (spin). The magnitude of the magnetic field strength in matter B acquires a maximum if, for a magnetic material, all atomic magnetic moments are aligned [9]. But the truth is that atomic magnetic moments are not necessarily aligned in all materials.

More specifically there are two contributions to the magnetic moment of an atom, those due to the orbital angular momentum and the intrinsic spin angular momentum of the electron. The magnetisation M or magnetic moment per unit volume of a material can result from a combination of orbital and spin moments, or from just one of these contributions. The different electronic configurations of different materials result in a variety of magnetic phenomena, which include diamagnetism, paramagnetism, ferromagnetism, and anti-ferromagnetism.

If the matter is approached quantum mechanically, the eigenvalues L of the orbital angular momentum operator $\hat{L}$ for an electron in a centrally symmetric potential are$[l(l+1)]^{\frac{1}{2}}\hbar$ in which the quantum number l takes the values 0, 1, 2, …, (n − 1) and are associated with the s, p, d, f and g electrons respectively. The principle quantum number n primarily determines the energy of a particular orbit. In a magnetic field $\boldsymbol{H} = H_z\hat{z}$, the eigenvalues of the operator representing the Cartesian component of the orbital angular momentum along the direction of the field $\widehat{L_z}$ are $m_l\hbar$. For a given value of l, m_l may take the (2l +1) possible values l, (l – 1),…, 0, – (l – 1), and – l. For example, the eigenvalues of $\widehat{L_z}$ for a d electron are 2ħ, ħ, 0, − ħ and − 2ħ. Quantisation of the orbital angular momentum leads to a spatially quantised atom since the electron orbits are restricted to particular plane orientations, Figure 2.1.

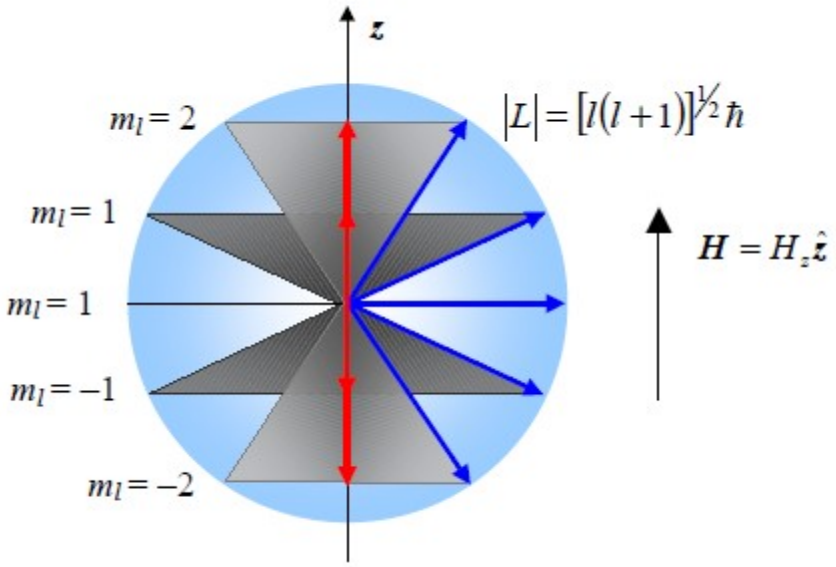

Figure 2.1: The vector model of orbital angular momentum for a d electron (l = 2). In a magnetic field H, the component of the orbital angular momentum $\widehat{L_z}$ is quantised taking values $m_l\hbar$ [10].

The magnetic moment μ generated by an electron with orbital angular momentum quantum number l is given by:

$$|\mu| = \frac{|e|\hbar}{2m_e c}[l(l+1)]^{\frac{1}{2}} \qquad (2.1.1)$$

where $e\hbar/2m_e c$ is the Bohr magneton (m_B = -0.927×10^{-20} ergOe^{-1}). Similarly, the component of the orbital magnetic moment along the direction of the applied field is:

$$\mu_z = \left(\frac{e\,\hbar}{2m_e c}\right) m_l \qquad (2.1.2)$$

Electrons also have an intrinsic spin angular momentum S. The eigenvalues of the spin angular momentum operator $\hat{S}$ are $m_s\hbar$. The spin quantum number m_s (= ± ½) determines the eigenvalue of the component of the spin angular momentum (= ± ħ/2) along the direction of the applied field. The component of the magnetic moment along the direction of the applied field μ_{sz} due to the electron spin angular momentum is then:

$$\mu_{sz} = g\left(\frac{e\,\hbar}{2m_e c}\right) m_s \qquad (2.1.3)$$

where g is the spectroscopic splitting factor or g-factor.

2.2 Diamagnetism-Paramagnetism

Most materials exhibit diamagnetism. The effect of an external magnetic field H on the electron movement of an atom is equivalent to inducing an extra current to the atom, which produces a magnetic bipolar moment that did not exist before, opposite to the direction of the field. Since this effect is independent of the atomic arrangement and applies independently to all atoms, one can conclude that the material acquires magnetism opposite the applied field. This behaviour is called diamagnetism and occurs in most of the materials, although it is sometimes overcome by the paramagnetic phenomenon described immediately thereafter. There is the possibility that the diamagnetic effect is strong enough that the total induced magnetic field H in the material is zero (perfect diamagnetism). This is the case with superconductors.

In paramagnetic materials, the interaction between permanent atomic moments is weak or zero. In the absence of a magnetic field the moments are randomly oriented and the magnetisation is zero. When an external field is applied, the moments tend to align along H and the magnetisation becomes non-zero in the direction of the field. This phenomenon is called paramagnetism. In this phenomenon of the orientation of the moments caused by the outer field, resists the tendency to reshape the moments to a more disordered delimitation due to thermal movement of the atoms. The overall result, however, is that the paramagnetic materials exhibit magnetisation in the same direction as the magnetic field.

2.3 Ferromagnetism

The main feature of ferromagnetic materials is that they exhibit a very large spontaneous magnetisation, which implies a natural tendency for adjacent atomic or molecular magnetic moments to be arranged under the interactions between them. As a phenomenon, ferromagnetism is related to the exchange interactions between the electron spins of atoms. The result is a parallel arrangement of the electrons or spins in microscopic domains called ferromagnetic domains. In particular, the direction of magnetisation in a region of a material also depends on the crystal structure of this material.

More specifically, a ferromagnetic material exhibits a spontaneous total magnetic moment in the absence of a magnetic field. The experiments show that in such a material the

magnetic momentum due to the orbital motion of the electron is negligible in front of that coming from the spin of the electron [11]. As a result, single electrons can be considered as microscopic magnets with the direction of their magnetic field being determined by their spin direction.

Initial attempts to explain the phenomenon of ferromagnetism were made on the basis of the dipole-dipole interaction. However, the energy of this interaction was much smaller than the one observed, and this approach was not enough to interpret the phenomenon. In 1928 Heisenberg developed a theory based on the Heitler-London model of the H_2 molecule to introduce the concept of the exchange interaction. Here, the explanation arises if the monoelectronic atom of hydrogen is considered. ψ_a (r1) represents the wavefunction of electron 1 in atom a while ψ_b (r2) represents the wavefunction of electron 2 in atom b. These separate wavefunctions can be either symmetric or antisymmetric with the combined wavefunction written as Ψ(r1,r2) which can have four solutions-possibilities. The solution that is needed is the one which gives unaltered observed properties by interchanging electrons, while the electrons remain distinct. That is when ΨΨ* is antisymmetric [12]. Pauli's exclusion principle dictates that never two electrons can be in exactly the same quantum state. So, consequence of this is that if there are two e.g. adjacent hydrogen atoms, their single spin electrons will be oriented so that their tracks tend to maximise the distance between them. The depiction of antisymmetric and symmetric wavefunctions and how their combination ΨΨ* can be symmetric is shown on figure 2.2.

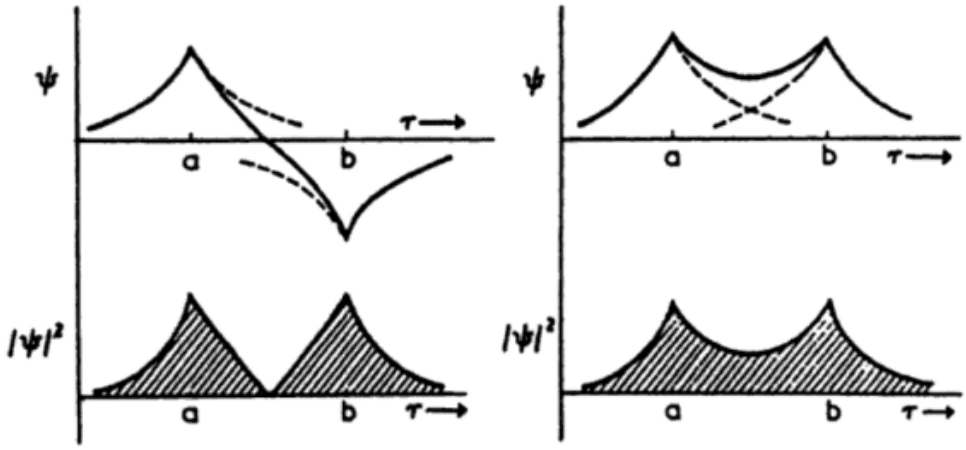

Figure 2.2: The two cases where two separate atomic wavefunctions of a and b can be whether antisymmetric (left), or symmetric (right). Their combination though ΨΨ in both cases is symmetric. This means that a wavefunction of the type of left is needed* [12].

The wave function of a two-electron system that is a fermion can also be written in the form ψ (r1, s1; r2, s2) with r_1 and r_2 expressing the spatial coordinates and s1, s2 the spin parameters of the two electrons. The non-discrimination of the electrons requires that, upon alternation, an anti-symmetric wave function [13] arises, so that

$$\psi(r_1,s_1;r_2,s_2) = -\psi(r_2,s_2;r_1,s_1) \quad (2.3.1)$$

The single-electron wavefunctions are functions of spatial and spin co-ordinates and may be written as:

$$\Psi^{(-)}(r_1,s_1;r_2,s_2) = \Phi_{space}(r_1,r_2)X_{spin} \quad (2.3.2)$$

where $\Psi^{(-)}(r_1,s_1;r_2,s_2)$ indicates that for an antisymmetric single-electron wavefunction, the spatial Φ and spinor X parts must be of opposite symmetry. The spatial wavefunction is a solution to the Schrödinger equation for an electron without spin and the spinor is a function of spin co-ordinates only. There are two combinations that give an antisymmetric two-electron wavefunction,

$$\Psi_{\mathrm{I}}^{(-)}(r_1,r_2) = \Phi_{space}^{(+)}(r_1,r_2)\mathrm{X}_{spin}^{(-)} \quad (2.3.3)$$

and

$$\Psi_{\mathrm{I}}^{(-)}(r_1,r_2) = \Phi_{space}^{(-)}(r_1,r_2)\mathrm{X}_{spin}^{(+)} \quad (2.3.4)$$

As a result, appears an additional term of electrostatic energy in the Hamiltonian function of the two electron system. This term, which is dependent on the overlapping of waveforms of neighbouring particles, is called an electrostatic exchange interaction and the exchange energy per pair of atoms can be written as:

$$E_{int} = -2J_{int}\, S_i S_j \cos\phi_{ij} \quad (2.3.5)$$

where S_i, S_j are the total spin angular momenta of atoms, ϕ is the angle between the spins of adjacent atoms and J_{int} is a coefficient called exchange integral and has a positive value for

ferromagnetic materials. One can observe that this function is minimised for a positive J_{int} when $\cos\phi_{ij} = 1$ or $\phi = 0$

This approach also helps to interpret the formation of ferromagnetic regions through the so-called "walls between the regions", as one will see below.

The arrangement of spins in a ferromagnetic material is also affected by the thermal energy inside a solid. It increases the movement of atoms around their balance position and disorients the spin of the electrons. Above a critical temperature value, known as the Curie temperature or the ferromagnetic transition temperature T_c, the thermal fluctuations of atomic spins overcomes the magnetic arrangement preferred in the material, thus stopping the material from displaying its original magnetic properties and behave as paramagnetic. One can obtain an equation for this temperature by making an approximate connection to the exchange integral J. It can be assumed that the atom with spin S is considered to have its closest neighbours z, that each binds to the central spin through the J interaction. The result of the theory of Weiss's mean field gives for T_c [21]:

$$Tc = \frac{2zJS(S+1)}{3k_B} \tag{2.3.6}$$

with $k_B = 1.38 \times 10^{-23}$ J K^{-1} being the Boltzmann constant.

Thus, some well-known ferromagnetic materials, such as iron, have relatively high Curie temperatures (e.g. 1043K for Fe, 627K for Ni) and thus remain ferromagnetic at room temperatures [7]. In this study the CoCrPt alloy was used which has a Curie temperature around 874K or 600°C [14]. However, ferromagnetic materials, in their natural state, are demagnetised at any temperature, even below T_c. To explain this fact, Weiss made the case of magnetic regions.

2.4 Ferromagnetic free energy contributions

The total magnetic free energy of a ferromagnet (E_{tot}) is depending on a number of contributions of different energies in the material which some of them compete and some supplement to obtain the minimum possible energy state. The most significant contributions to the free energy are the so-called exchange interaction (E_{ex}), the Zeeman energy (E_Z), the magnetostatic energy (E_{ms}) and the anisotropy energy (E_{ani}). The total magnetic energy can be written as:

$$E_{tot} = E_{ex} + E_Z + E_{ms} + E_{ani} \quad (2.4.1)$$

2.4.1 The exchange interaction

Heisenberg formulated an exchange interaction energy with the help of quantum physics which explains why in ferromagnetic materials the spins and consequently the moments tend to align parallel to each other and this minimises this energy. In terms of the Heisenberg Hamiltonian one can obtain for the energy:

$$H_{ex} = -2J_{ex}\sum_{i\neq j} S_i S_j \quad (2.4.2)$$

This interaction is considered to be short range therefore accounts for the nearest neighbour spins and is negligible when the distance becomes larger and reduces by a factor of $1/r^6$. The exchange integral J_{ex} has positive sign giving parallel alignment of neighbouring spins the minimum energy.

2.4.2 The Zeeman energy

The Zeeman energy results from the interaction between the magnetisation M of the system and an external applied field H. When an external field is applied, the magnetisation will tend to align with the field in order to minimise the potential energy. The rise in energy is directionally proportional to the angle θ between the magnetisation and the applied field thus it can be given by:

$$E_z = -M \cdot H \cos\theta \quad (2.4.3)$$

2.4.3 The magnetostatic energy

The magnetostatic energy is concerned with long range magnetostatic interactions of atomic moments which generate an internal strong field opposite to the magnetisation which

is known as the demagnetisation field H_d. The demagnetising field may be written as $\mathbf{H}_d = -N\mathbf{M}$ where N is a 2nd rank tensor represented by a matrix. The energy can be written as:

$$E_{ms} = -\frac{1}{2}\mathbf{H}_d \cdot \mathbf{M} \qquad (2.4.4)$$

The ½ factor appears in the equation so that the moments are not counted twice. The strength of the magnetostatic interaction is several orders of magnitude weaker than that of the exchange interaction. However, the exchange interaction is short range and isotropic while the magnetostatic interaction is long range and sensitive to the shape of a sample. Therefore, the magnetostatic energy is an important contribution to the total free energy and by minimising it gives rise to anisotropic effects in which the magnetisation prefers to align along a particular axis of a ferromagnetic sample. Ferromagnetic domains may also develop in order to minimise the magnetostatic energy further.

2.4.4 Anisotropy energy contributions

The anisotropy energy arises from the fact that in magnetic materials the magnetisation prefers to orient along an easy axis comparing to other directions and it requires some energy to direct the magnetisation along a hard axis. There are several contributions to the magnetic anisotropy which include magnetostatic shape anisotropy, magnetocrystalline anisotropy, and surface anisotropy.

2.4.5 Shape anisotropy

The geometry of a sample plays an important role in decreasing or increasing the anisotropy energy of a system. As it was seen before the magnetostatic contributions to the material give rise to a stray field which promotes a high energy state and the system tends to reduce this energy by setting the magnetisation to align along an axis where the demagnetising field H_d is smaller.

2.4.6 Magnetocrystalline anisotropy

The preference for the magnetisation to be oriented along particular crystallographic axes of a sample is called magnetocrystalline anisotropy. The origin of magnetocrystalline

anisotropy is the spin-orbit interaction. When the spin-orbit interaction is present, a small orbital moment is induced which couples the total (spin + orbital) moment to the crystal axes. As a result, the energy depends on the direction of the magnetisation relative to the crystal axes, and the energy reflects the symmetry of the crystal structure. There are two common types of magnetocrystalline anisotropy known as uniaxial and cubic anisotropy. In hexagonal cobalt where uniaxial anisotropy occurs the energy can be written as a function of the angle between the c- easy axis and the magnetisation θ and can be expressed by anisotropy constants (K_1 and K_2) which can be determined experimentally:

$$E_u = -K_1 \sin^2(\theta) + K_2 \sin^4(\theta) = -K_1 \hat{u}_z^2 + K_2 \hat{u}_z^4 \qquad (2.4.5)$$

where $\hat{u}_z = \frac{\vec{M}}{|M|}$ is the unit vector of the magnetisation along the z axis which is the c axis of the hexagonal structure. CoCrPt comes with a perpendicular magnetic anisotropy of approximately 8 x 10^6 erg/cm^3 [14].

For cubic Fe and Ni, the expression of anisotropy energy is:

$$E_C = K_1(u_x^2 u_y^2 + u_y^2 u_z^2 + u_x^2 u_z^2) + K_2(u_x^2 u_y^2 u_z^2) + \ldots \qquad (2.4.6)$$

where u_i ($i = x, y, z$) are the components of the unit vector of the magnetisation along the *x*, *y*, and *z*-directions which are defined along the crystallographic axes.

2.4.7 Surface anisotropy

The surface anisotropy energy represents the tendency of the surface moments to align either parallel or perpendicular to the surface of the material because a magnetic moment of the surface layer of atoms has nearest neighbours from one side of the material but not any neighbours from the other side and therefore the exchange interaction of these atoms is not the same as of those inside the bulk material. The surface anisotropy energy per unit area may then be written as:

$$E_S = \frac{1}{2} K_S (\hat{u} \cdot \hat{n})^2 \qquad (2.4.7)$$

where K_S is the anisotropy constant of the surface and can be determined experimentally by several techniques such as FMR [15], [16] and rotational MOKE measurements [17], û is the unit vector parallel to the magnetisation and $\hat{n}$ the unit vector perpendicular to the surface respectively.

2.5 Perpendicular magnetic anisotropy

The material I studied in this work was mainly CoCrPt which exhibits perpendicular anisotropy. This is because of the hexagonal structure that it crystallises in where the easy axis of crystallization is along the c-axis of the unit cell. The lattice constants for this material have been estimated as, $a \cong 0.255$ nm and $c \cong 0.415$ nm [14]. If a seed layer of proper structure lies underneath then this c-axis will grow out-of-plane and will result in an out of plane anisotropy. In Figure 2.3 it is depicted the places in the unit hexagonal cell that Co and Pt atoms arrange. This is the known as $L1_0$ phase which enhances the anisotropy K_U to $> 8 \times 10^6$ ergs/cm^3 and it is favourable for hard disc applications. The grain size of the media is about 6nm. The stoichiometry of the alloy in the target was $Co_{66}Cr_{10}Pt_{18}(SiO_2)_6$ following the structure of the CoPt alloy with the Cr tending to segregate to the grain boundaries to reduce M_S so that the anisotropy field is higher than the demagnetisation field. As a result, the demagnetisation field is not able to bring the magnetisation back into the plane of the substrate.

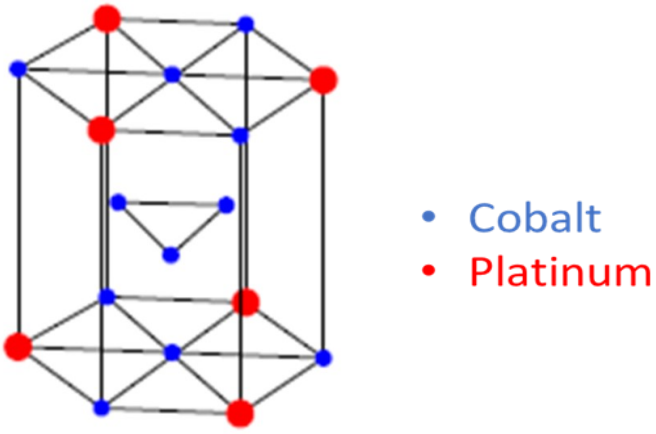

Figure 2.3: The hexagonal structure of CoPt which exhibits perpendicular magnetic anisotropy[18]. *CoCrPt follows a similar structure with the Cr atoms segregated to the grain boundaries.*

In a structure like this all directions in the basal plane are equally hard so that anisotropy is only dependent on a single angle θ_U and it is uniaxial. As a result, the anisotropy energy can be given by the equation:

$$E_K/V = K_0 + K_1 \sin^2\theta_U + K_2 \sin^4\theta_U + \cdots \qquad (2.5.1)$$

where θ_U is the angle between the easy axis direction and the magnetisation. Anisotropy energy E_K is still dependent on the K_1 term and the third term is small due to $\sin^4\theta_U$ and is neglected.

2.6 Interfacial anisotropy

At some point of our work a Co interlayer was introduced between the seed layers and the antiferromagnet in our multilayer structure. This fact enhanced the perpendicular anisotropy by a mechanism called interfacial anisotropy. In order to activate the anisotropy of such a system the Co layer must be no more than 2 atoms thick or else it would collapse. This means that the typical thickness of such a layer must be limited in a range of 0.3 to 1 nm. The main cause of such an anisotropy enhancement is through structural anisotropies of the interlayer [19] . Barton et al. showed that the interfacial anisotropy of Co/Pd multilayers is controlled by the interface roughness [20]. However, the interfacial roughness is dependent on the atomic size as depicted in the following figure. For a thin film sample the atomic growth is not evenly distributed across the surface. Assuming the layer thickness is 0.6nm, which is approximately 2 atoms thick, there are areas which have only 1 or more than 2 atoms. In Figure 2.4 it can be seen that the blue atoms are bigger than the red ones. Hence the surface roughness of the red area is lower than that of the blue area. Hence the grain size is proportional to the surface roughness Δt. In a study Vopsaroiu et al. [21], showed that the grain size was shown to be proportional to the deposition rate using the HiTUS deposition system. Hence the surface roughness of a multilayer sample can be controlled. In order to achieve low surface roughness a low deposition rate is required.

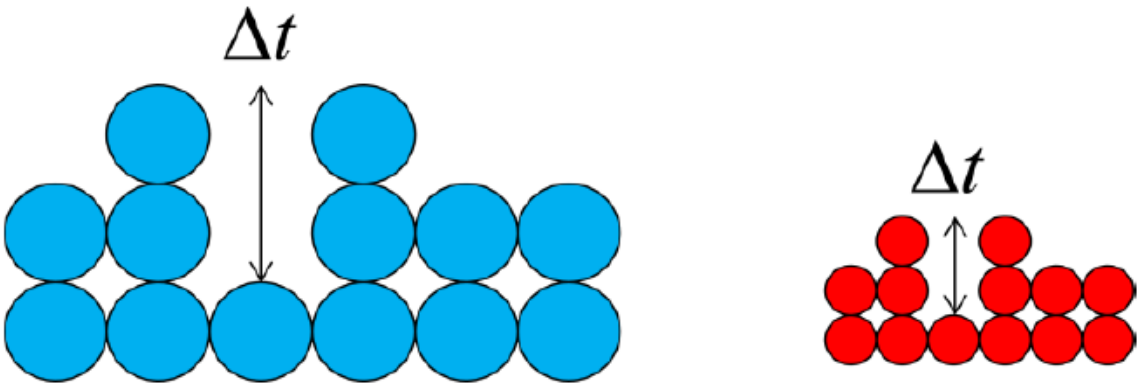

Figure 2.4: Schematic diagram of the effect of atomic size on surface roughness of two different materials (red and blue) [22].

2.7 Magnetic domains and walls

Ferromagnetic materials consist of magnetic domains, which are small sections of the magnetic material consisting of groups of 10^9 to 10^{15} atoms in which the atomic magnetic dipoles are arranged in the same direction. The magnetic dipoles are arranged in this way to minimise the magnetic energy within the material.

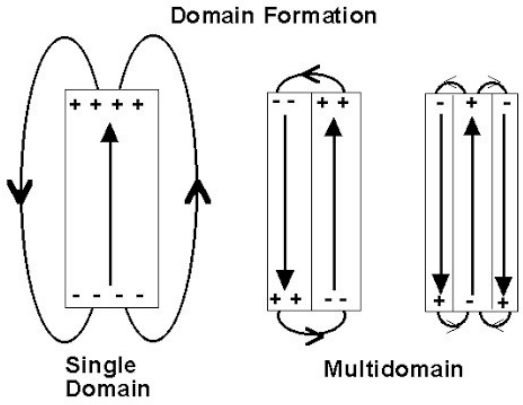

Figure 2.5: Depiction of how the formation of multiple domains affects the reduction of the magnetostatic field and consequently energy in a ferromagnet.

If a material consisted of a single magnetic region, then a very powerful magnetic field (called a demagnetisation field) would be produced and the total energy would be directly related to it. Thus, although there is a total magnetisation within each magnetic region, its

direction from the neighbouring domains differs (Figure 2.5). As a result, in a continuous material, there is a clear reduction of the magnetisation and therefore the total energy. When, however, a ferromagnet is placed in an external magnetic field H, the field will exert a force so that the magnetic dipoles are oriented in the direction of the field. Those regions with a magnetisation component parallel to the external field will favour by increasing their limits by rotating some magnetic dipoles from those neighbouring regions that are not favourably oriented. When the external field becomes strong enough, all regions will be joined together and lattice magnetisation will be forced to follow the direction of the applied field. If the external field is removed, some of the electrons "remember" the original favourable condition.

The majority, however, of the electrons keep the field-induced change in direction and thus remains a net total lattice magnetic moment. A simple schematic diagram, similar to that used by Rudden and J. Wilson, is shown in Figure 2.6. Without the external field exercise (Figure 2.6a), the different magnetic regions are oriented in different directions and the total magnetisation of the solid is zero. When an external field is applied, areas 1 and 2 are expanded to the detriment of regions 3 and 4 which do not have magnetic moment components in the direction of the field (Figure 2.6b). When the external field becomes strong enough, all areas are joined together and aligned with the field (Figure 2.6c). At that point the specimen has reached the so-called saturation magnetisation, which is the maximum magnetisation that the sample can display. Then, the outer field is removed and only a few of the electrons return to their original, random state (Figure 2.6d). The sample retains a magnetisation called remanence magnetisation.

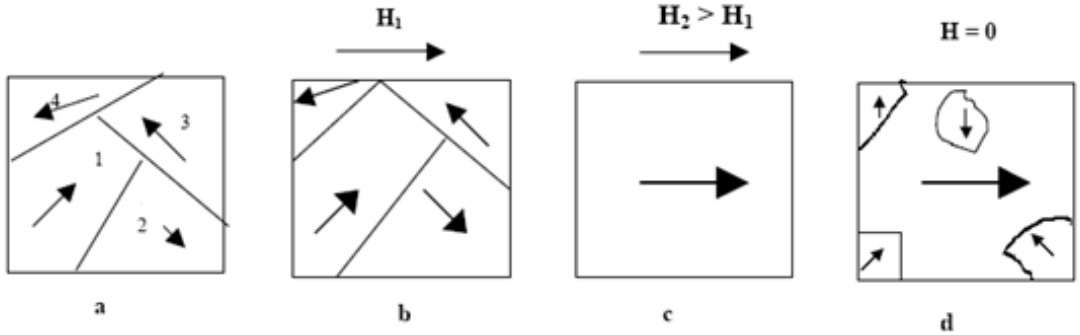

Figure 2.6: A schematic representation of the magnetisation procedure of a ferromagnet, showing the diffent magnetisation directions that domains take through the whole process [11]

Since the magnetic materials are considered to have some sort of memory of their original state, the magnetisation of a ferromagnetic material M with respect to the externally applied field H shows a loop of hysteresis. This is the result of two effects: rotation of magnetisation and changes in size or number of magnetic domains.

To form these walls in the material, some energy is required since the directions of the spin change from one side of the wall to the other. Here is also the relation (2.4.2) for the exchange energy, which is $E_{int} = -2J_{int}\, S_i S_j \cos\phi_{ij}$ per pair. If one considers the wall infinitely thin, then $\theta = \pi$ for two spins on the opposite sides of the wall, and therefore the exchange energy per pair is made $|E_{int}| = 2J_{int}\, S^2$, whereby the exchange energy per unit area of the wall is very large. This contrasts with the reduction in magnetostatic energy that occurs with the increase of the areas. One way to reduce exchange energy for the system to be energy-stable is to gradually rotate the spins from the direction of one region to that of the other. The wall between the regions has a finite thickness and is called the Bloch wall (Figure 2.7.).

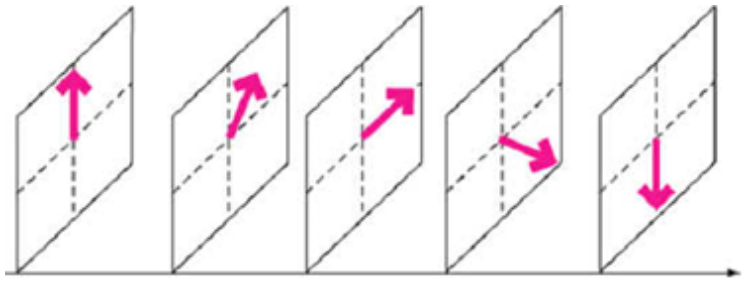

Figure 2.7: Gradual change of spin (in steps at the same angle each time) in one Bloch wall of finite thickness [23].

The change of spin in N steps, i.e. in N consecutive turns at the same always angle, reduces the energy of exchange by $JS^2\phi^2$

$$|E_{int}| = |-2JS^2\cos\phi| \approx |-2JS^2 + JS^2\phi^2| \qquad (2.7.1)$$

The reason why the wall does not become unlimitedly wide is the opposite effect that the magnetocrystalline anisotropy energy has on the lattice which tends to be as low as possible so as to be in a more favourable energetic state. The anisotropy energy is lowest when the individual magnetic moments are aligned with the crystal lattice axes thus reducing the width of the domain wall.

2.8 Hysteresis loop of a magnetic material

As mentioned earlier, because of a kind of "memory" which ferromagnetic materials display, in terms of their original state, even when magnetised from an external field, a typical hysteresis loop is developed in the M-H diagram. This property is readily apparent from the diagram and states that the magnetic state of a ferromagnetic material does not follow the same path when the intensity of an externally applied field increases and then decreases. M is the magnetisation of the material and H the external magnetic field. When the external field value grows, the magnetic moments of the atoms inside the walls are rotated to magnify the favoured magnetic regions. When a field is drawn in the opposite direction to the original, the material remains magnetised at the originally prevailing magnetisation time, unless the field grows sufficiently and acquires a certain value. Then the action-movement of the magnetic regions is reversed and soon the process will be repeated with the material being magnetised in the new direction of the field, unlike its original. Finally, if the field drops to zero, one can complete the path to the hysteresis loop depicted in Figure 2.8. Basic parameters in a hysteresis loop are as follows:

(a) Saturation Magnetisation

Typically, in its original state, a ferromagnetic material is in its demagnetised state. But if the external applied field is increased then the magnetisation of the material will begin to increase until it reaches its maximum value. This is the saturation magnetisation M_S which states that all the magnetic moments of the atoms in the material have been aligned in the direction of the field. This means that saturation magnetisation is a property dependent only on the type of material and not on its structure.

$$M_S = nm, \quad n = \text{atoms per unit volume} \qquad (2.8.1)$$

$$m = \text{atomic magnetic moment}$$

b) Remanence

When the field value is reset, after it has magnetised the ferromagnetic material, then there is a residual magnetic induction B_r and thus a residual magnetisation M_r in the material:

$$B_r = \mu_0 M_r \qquad (2.8.2)$$

where $\mu_0 = 4\pi\times10^{-7}$ N/A^2 is the vacuum permeability. Usually, however, as a remanence is considered the remaining magnetisation, after the material has been magnetised to saturation.

c) Coercivity

The magnetisation of the material can be reset by applying a negative magnetic field H_C. This value of the outer field that negates the magnetisation of the material is called coercivity and is usually calculated in the second quadrant of the B -H diagram. In Figure 2.8 the coercive field can also be calculated by the relationship

$$H_C = \frac{Hc_1 - Hc_2}{2} \qquad (2.8.3)$$

where H_{C1} is given by point c and H_{C2} from point f of the figure.

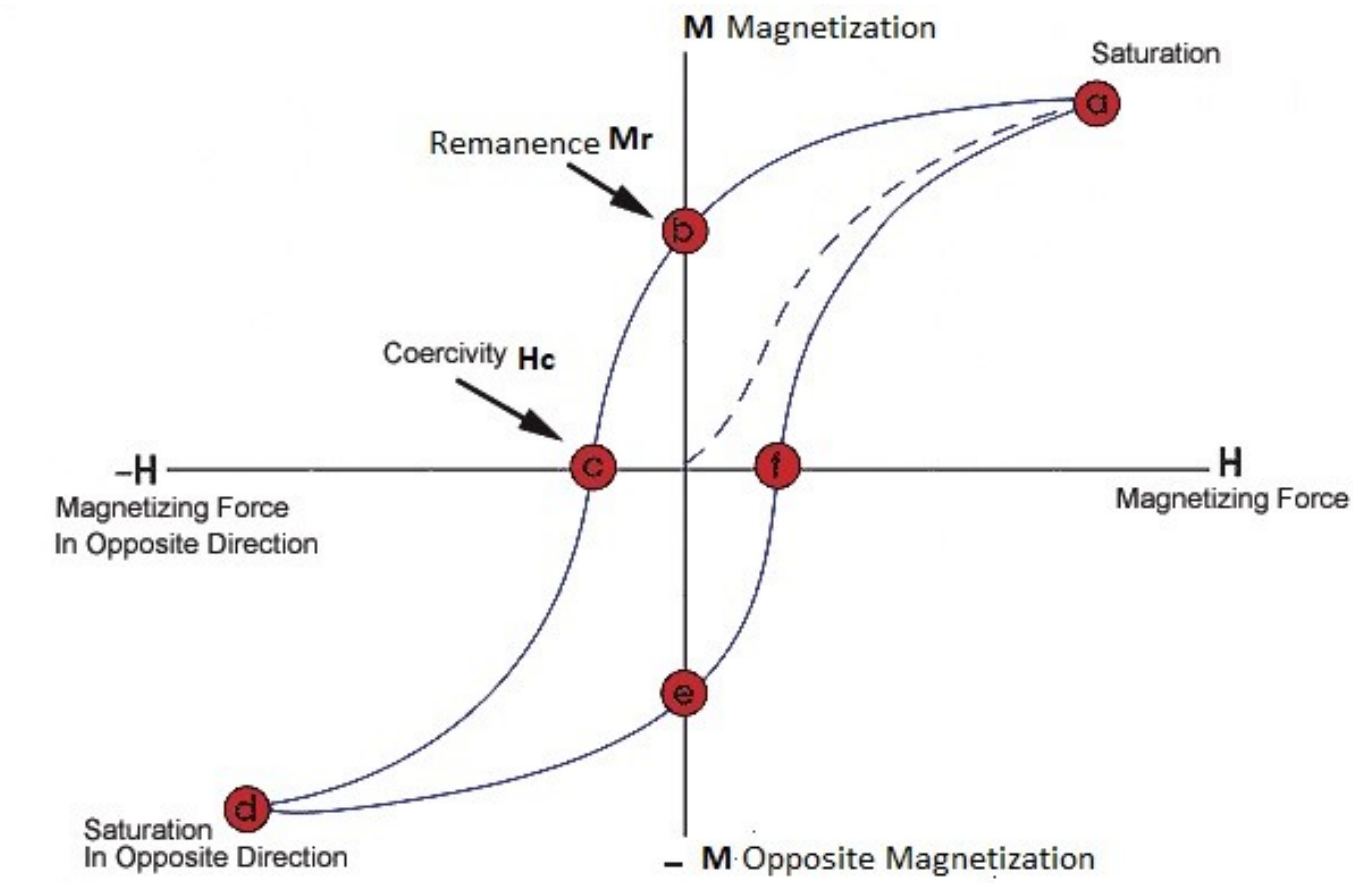

Figure *2.8*: An example of a magnetic hysteresis loop. The values of remanence (M_r) and saturation magnetisation (MS) are shown. The points c and f give respectively the values H_{C1} and H_{C2} from which the coercive field (H_C) is calculated *[24]*.

2.9 Exchange interactions in thin films

The magnetic behaviour of the thin films in this project could not be studied without taking into consideration the different mechanisms that lead to the different types of ordered magnetism. These interactions are called exchange interactions and are divided in three types: the direct exchange, the RKKY exchange and the superexchange. Superexchange has its origin in the antiferromagnetism in oxides where there is antiparallel coupling between the metal orbitals via the p-orbital of an oxygen atom. Therefore, it is not discussed further in this work.

2.9.1 Direct exchange

The Direct exchange also called Heisenberg exchange was mentioned earlier in section 2.4.1 and is a result of very close distance interactions between spins. The effect of the coupling falls as of $1/r^6$, where r is the atomic separation and therefore is significantly affected by structural changes. The exchange energy E_{ex} between the two adjacent ns $S_{1,2}$ is given by equation 2.4.2. The curve known as Bethe-Slater curve shown in Figure 2.9 shows the exchange integral plotted against the ratio r_{ab}/r_d where r_d is the radius of the 3d orbital and r_{ab} the interatomic distance. This curve actually separates the ferromagnetic 3d elements from the antiferromagnetic 3d elements.

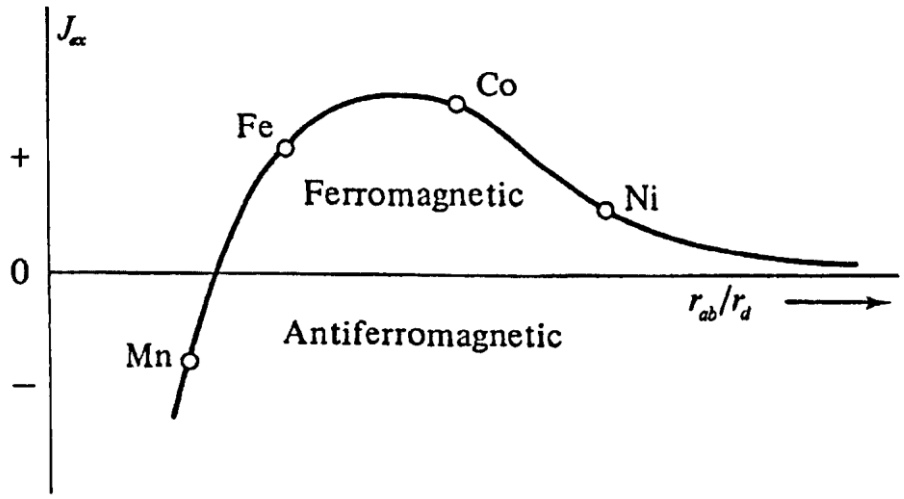

Figure 2.9: The Bethe-Slater curve showing variation of exchange integral with atomic distance ratio. Depending on the position on the curve some elements can behave as Ferromagnetic and some as Antiferromagnetic [25]

What one can conduct from this figure is that for a selected few elements like Fe, Co and Ni the J_{ex} is maximum when the spins lie in a parallel direction and thus the material behaves as a ferromagnet. For other elements like Mn or Cr an antiparallel alignment is preferred which gives a negative value of J_{ex}. Considering the electrostatic interaction Hamiltonian for the H_2 molecule one can see that it depends inversely on the distance between the two atoms r_{ab}. J_{ex} will be positive if the positive contributions of the Hamiltonian exceed those from the negative terms. These conditions are met if the r_{ab} is large compared to the orbital radii. J_{ex} is then likely to be positive for d and f wavefunctions for the atoms of some iron and rare earth metals like mentioned before [10].

2.9.2 Indirect exchange

The indirect exchange also known as RKKY interaction was initially proposed by Ruderman and Kittel [26], Kasuya [27] and Yoshida when trying to explain the exchange coupling in rare earth metals. This indirect exchange originates from the local magnetic moment polarising the conduction electrons which align nearby moments even across grain boundaries. Therefore, it is a long-range coupling and the exchange integral oscillates between positive and negative values as the separation between atoms varies. In advanced recording media inside the grain direct exchange interaction between the atoms is exhibited while the RKKY coupling is present between the different grains (Figure 2.10).

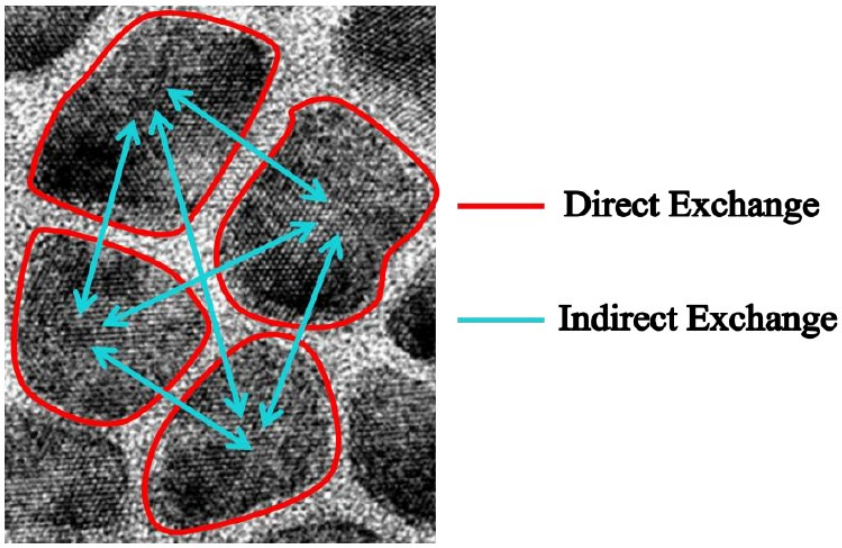

Figure 2.10: Depiction of direct (inside red areas) and indirect exchange interaction between neighbouring grains in a high resolution TEM image of advanced recording media. [28]

Hence the SiO_2 insulator is used in our segregated recording material CoCrPt to eliminate the RKKY coupling and fill the gap between the grains in the voided structure. A characteristic of this indirect exchange coupling is that it exhibits oscillation in its values with respect to the spacer thickness, which in our case is Ru. It can get both negative and positive values and behave either as ferromagnetic or as antiferromagnetic exchange respectively. In Figure 2.11 this oscillation is being shown.

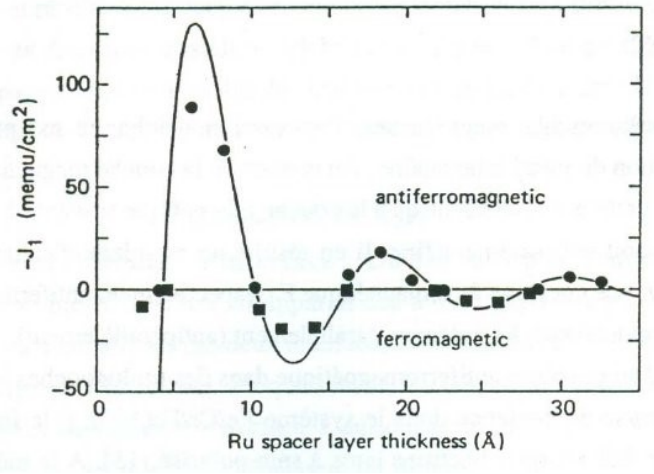

Figure 2.11: Intensity of indirect exchange coupling J1 between layers of $Ni_{80}Co_{20}$ as a function of the Ruthenium interlayer thickness [29].

2.10 Magnetisation reversal mechanisms

At the coercive field, the vector component of the magnetisation of a ferromagnet measured along the applied field direction is zero. There are two primary modes of magnetisation reversal: single-domain rotation and domain wall motion.

2.10.1 The Stoner-Wohlfarth theory.

The theory established in 1948 by Stoner and Wohlfarth [30] describes the main reversal mechanism for a magnetic single domain with a critical size which is material dependent. The theory can be applied to the hysteretic processes in a thin film with small grains which means that the small grain size is needed so that each grain can act as a single magnetic entity without the presence of magnetic walls in between. In the simplest case, an ellipsoid like in the figure 2.12 is taken into consideration, so that the vectors of H and M_S are under an angle with the easy axis c of the domain.

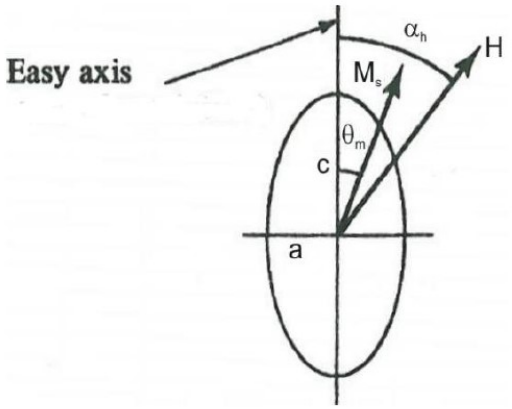

Figure 2.12: Definition of angles in the Stoner-Wohlfarth model. The two angles are ϑ_m which is the angle between the saturation magnetisation and the easy axis of the domain and a_h which is the angle between the external field and the easy axis c [25].

In this way there are only two energy terms taken into consideration for a given particle, the anisotropy energy E_a and the Zeeman energy E_Z that contribute to the total energy. For the anisotropy energy is considered only the first term of equation 2.4.5 so that:

$$E_\alpha = - K_u \sin^2(\theta_m) \qquad (2.10.1)$$

where K_u is the uniaxial anisotropy and θ_m is the angle between the c-axis and the magnetisation direction. The Zeeman energy is given by:

$$E_Z = -HM_S\cos(\alpha_h - \theta_m) \qquad (2.10.2)$$

where H is the applied field, M_S is the saturation magnetisation and $\alpha_h - \theta_m$ the angle between them. The total energy in this simpler system is $E_{tot} = E_a + E_Z$. In order to achieve equilibrium position of the moment direction one can differentiate the E_{tot} with respect to the angle θ_m. Assuming that the field is normal to the easy axis $\alpha_h = 90^o$ one can get the following expression for the anisotropy field:

$$H_a = \frac{2K_u}{M_S} \qquad (2.10.3)$$

where M_S is the saturation magnetisation and K_u the uniaxial anisotropy. This means that reversal will only occur when the magneto-static energy from the applied field overcomes the anisotropy energy (E_α). When this point is reached all of the particles will reverse

simultaneously with their atomic spins parallel, called coherent rotation. The applied field required to do this is H_K. This results in a hysteresis loop are shown in Figure 2.13. It shows different angles, one of which is α=90°.

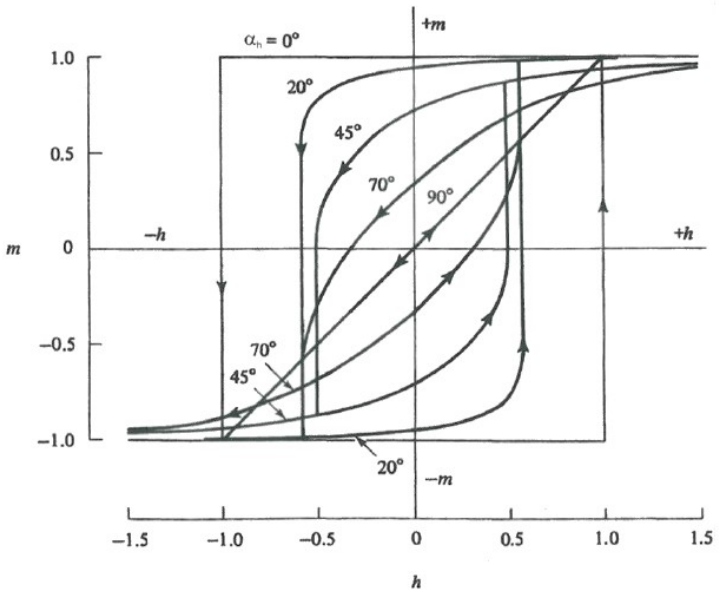

Figure 2.13: Hysteresis loop calculations for different values of angles between the easy axis and the applied field α_h, with one of them being α_h=90° [18].

Figure 2.13 shows that a small deviation of the easy axis direction from that of the applied field leads to a significant reduction of switching field. In the case of a deviation of 10° this leads to a reduction of the switching field of 30%. In perpendicular recording media (PMR) the deviation of the easy axis direction of the grains largely determines the thermal stability [7]. The standard deviation of the grain size distribution and that of the anisotropy constant are the factors which affect the switching field distribution in recording media [22]. In advanced recording media the standard deviation of the grain size distribution is lower than 0.2 [17]. The media is now deposited using heated substrates [7] and results in fully crystalline grains in the CoCrPt-SiO_2 layer. Therefore, the distribution of the anisotropy constants is very small. Hence the key factor that affects the switching field is the orientation of the grains.

2.10.2 Coercivity Mechanism.

In the nucleation type magnets, domain wall motion inside almost perfect grains is easy, but the nucleation field necessary to create new Bloch walls is high, as no extended defects lower the Bloch wall energy. When magnetising this type of material in a field below the saturation field, the remaining domain walls cause a lower remanence than when magnetising by a field strong enough to remove all domain walls. This coercivity mechanism is usually valid when relatively large and perfect grains exist and can be used to describe annealed $Nd_2Fe_{14}B$ films on Ta/Si(111) (a system showing no intermixing) and films grown on heated W/Si(111) where only few neodymium-rich precipitates are observed [31].

In pinning type magnets, the nucleation of reversed domains is not inhibited, but a lot of defects exist—preferably with a size comparable to the Bloch wall thickness—where the domain walls are pinned. Magnetisation reversal occurs when the force exerted on the domain wall (pinned at the inhomogeneities) becomes sufficiently strong. In $Nd_2Fe_{14}B$ films deposited on heated Pt/Si(111) and in annealed samples on silicon pinning seems to control the coercivity [31].

2.11 Antiferromagnetism

In some materials the spins of the electrons are arranged in antiparallel directions resulting in a zero-total magnetisation of the material. In this case, the phenomenon of antiferromagnetism takes place. However, the susceptibility $\chi(0K) \neq 0$. To explain this behaviour Neel applied the Weiss molecular field theory in the mid-20^{th} century. The susceptibility χ increases as the temperature T is reduced and goes through a maximum at a critical temperature called the Neel temperature T_N. The substance is AF below T_N and paramagnetic above T_N. Another important temperature in antiferromagnetic materials is the blocking temperature T_B. The maximum blocking temperature T_B is usually defined as the temperature at which the exchange field goes to zero. The standard method to determine T_B is based on the measurement of the hysteresis loop of an exchange biased system with increasing temperature until the shift in the loop becomes zero [32]. Although Fernandez-Outon [33] followed another path and defined T_B as the median Blocking Temperature at which equal fractions of the AF are oriented in opposite directions and is a measure of the energy barriers to reversal within the AF.

The AF (antiferromagnetic) material used in this project was IrMn due to its fabrication characteristics and physical properties. The Neel temperature in disordered y-phase Ir_xMn_{1-x} alloys increases with increasing Ir content from 570K for x=0.08 to 730K for x=0.25 [32]. The material also exhibits high resistance to corrosion and high anisotropy of typical values of 10^7 erg/cm^3. Its main applications are in Giant Magneto-Resistance (GMR) and Tunnelling Magneto-Resistance (TMR) junctions on the read heads but it could potentially be used in the recording layer as well. Tsunoda et al. [34] showed that there is a strong relation between the exchange bias obtained and the relative percentage of iridium and manganese ions in the material. In Figure 2.14 is depicted the anisotropy constant and degree of order as a function of the Ir content for this specific AF material. It is shown that there is a broad peak from 15 to 35 % Ir above and below which anisotropy and consequently crystallographic ordering rapidly falls. As a result, for this range one can notice a stronger exchange bias effect.

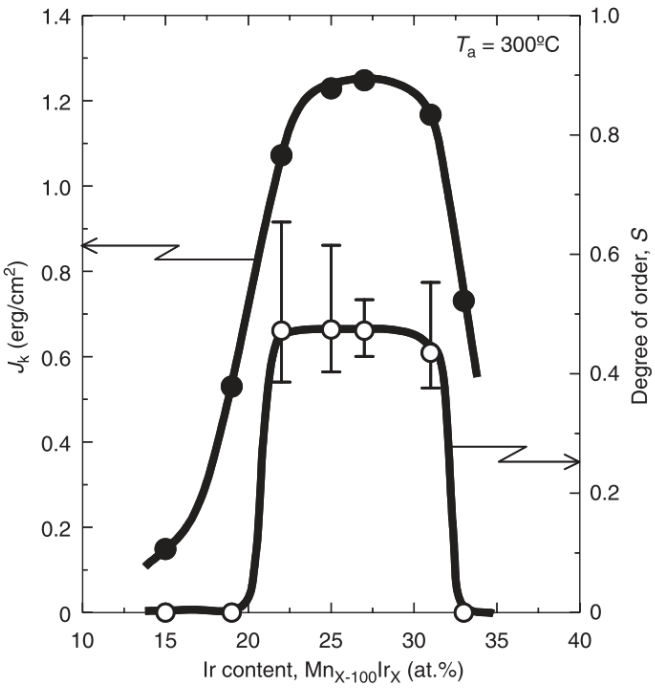

Figure 2.14: Unidirectional anisotropy constant J_K and degree of order S as a function of Ir content [34].

In our thin film production procedure, I used a target of IrMn with 25 at. % of Ir which is equivalent to $IrMn_3$. The target was not an alloy but instead consisted of stoichiometric powder-pressed mixture of Ir and Mn metals. The composition of the film is not necessarily

the same as that of the target because of the difference in binding energies of Ir and Mn. Since the binding energy of Ir is higher than that of Mn the atoms of the latter reach easier the surface of the substrate and as a result the layers are Mn reach which might mean that there is $IrMn_4$ which still is in the preferred range. In my samples though I have most probably the disordered phase which was confirmed by XRD measurements.

Neutron diffraction studies have been performed for single crystal samples of fcc IrMn [35]. These show the Mn spin moments lying in the (111) plane containing three sublattices pointing in the <112> directions which are separated by 120^0. These planes I am trying to take advantage of to achieve perpendicular exchange bias. In Figure 2.15(a) the arrangement of the unit cell is shown [35]. The solid circles represent Ir lattice sites and the open circles represent Mn lattice sites. The unit cell contains three Mn ions and one Ir ion. In Figure 2.15 (b) are depicted the three spin sublattices separated by 120^0 [35]. Nevertheless, this triangular spin structure was not observed experimentally in the polycrystalline films I used in my work and a more favourable formation was the disordered one.

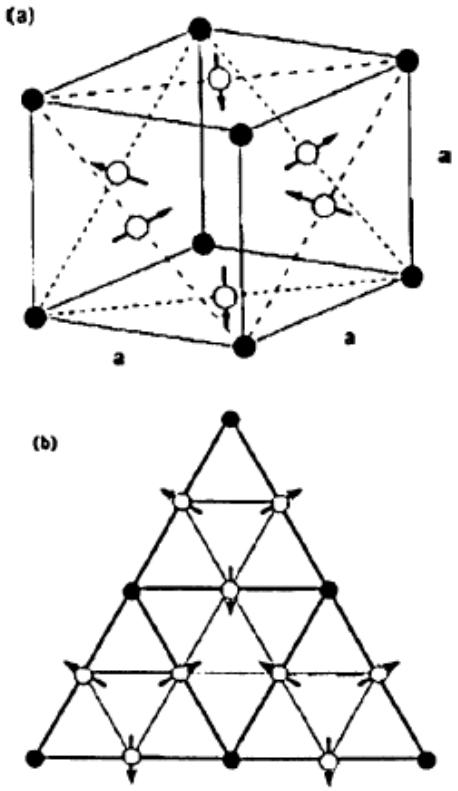

Figure 2.15: The spin structure of $IrMn_3$ in (a) the unit cell and (b) a section on a (111) plane according to neutron diffraction studies of bulk samples [35].

2.12 Exchange bias

The exchange bias phenomenon takes place in the interface between Ferromagnetic/Antiferromagnetic materials including thin films and it is defined by a characteristic displacement of the centre of the magnetic hysteresis loop along the field axis. The AF layer can cause the pinning of the ferromagnetic material to a preferred magnetisation direction. This induced anisotropy, or the loss of directional symmetry, results in the displacement of the centre of the hysteresis loop along the axis of the external field to a new position H_{ex}, the so-called exchange field (Figure 2.16). In addition, there is a change in the coercivity value, in particular a reinforcement. From Figure 2.8 one can estimate the exchange bias field after obtaining point P_1 and P_2 as:

$$H_{ex} = \frac{|H_{C1}+H_{C2}|}{2} \tag{2.12.1}$$

which corresponds to the distance of the centre of the loop from the origin of the axis where H_{C1} and H_{C2} can take either positive or negative values depending on how much the loop has been displaced to the negative values of the field axis and on the thermal and magnetic history of the sample.

To induce the exchange bias phenomenon in a bilayer material, one has to first heat close to temperatures as low as 475K for the IrMn case, but not as high as the Curie temperature of the FM material and then to cool it in the presence of a magnetic field H_{FC}, a process called as field cooling, to achieve the pinning of the magnetisation in the direction of the external field and the extra anisotropy (Figure 2.16). The setting process of the AF well below its Néel Temperature is achieved by the thermal activation of the orientation of the AF lattice within each grain as first described by Fulcomer and Charap [36].

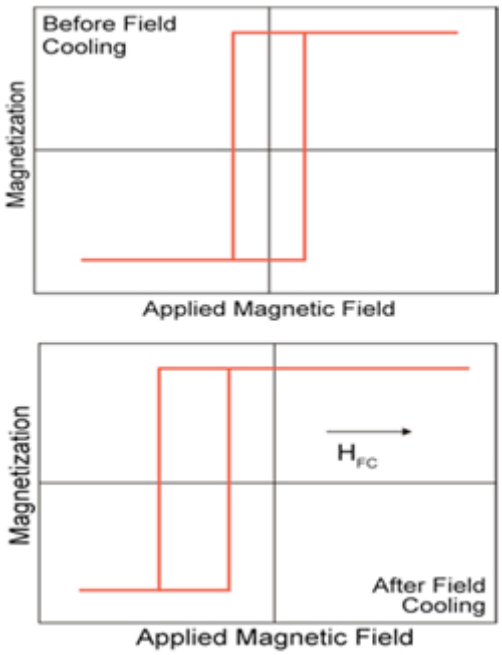

Figure 2.16: The characteristic hysteresis loop of a material before and after field cooling [23].

The process of pinning of magnetic moments can be explained as following: The thermal activation of the antiferromagnet over energy barriers is a process which causes the spin of the electrons of the AF material to have random orientation. An external field can then be applied to cause the spin of the electrons of the ferromagnetic material (FM) to align with it as the AF spins remain randomly oriented. If the sample is then cooled in the presence of the field, the spin of the AF at the interface will be ferromagnetically aligned with the adjacent FM electrons and the remaining AF electrons will return to their original AF arrangement. As in several common applications, here too, pinning takes place at a temperature well below the Néel temperature (this is called the blocking temperature T_B and is the temperature at which as the temperature at which equal fractions of the AF are oriented in opposite directions and is a measure of the energy barriers to reversal within the AF, [33]) . The AF layer will then remain pinned in this direction, making subsequently the ferromagnetic layer prefer that direction more than any other. Interfacial AF spins will continue to exert a torque at the interfacial FM spins to require a significantly larger field to magnetise the sample in the opposite direction to the initially applied cooling field (H_{FC}). This is what creates the negative displacement in the hysteresis loop regarding the direction of the original field during cooling.

2.13 Early models of exchange bias

In the early stages there have been many attempts to explain a variety of exchange bias systems so that have been categorized in three different categories. Following the Coehoorn [37] categorization the models are divided in macroscopic, mesoscopic and microscopic depending on the scale of the studied systems.

Macroscopic, are called those theoretical models that do not take into account the longitudinal magnetic ordering of the layers. In particular, these models assume that in the x-y plane the magnetisation of the layers is homogeneous. Thus, in most macroscopic models, a detailed description of the spin arrangement is found only in the z-direction of FM and/or AF material. The first theoretical approach developed to interpret the phenomenon of exchange bias was by Meiklejohn and Bean [38]. The two basic assumptions of this model are that the magnetisation rotates continuously, and that the easy axes of FM and AF are parallel. This is a representative macroscopic model and through this approach energy E per unit area S can be written [39] as:

$$E/S = -HM_{FM}x_{FM}\cos(\theta-\beta) + K_{FM}x_{FM}\sin^2(\beta) + K_{AF}x_{AF}\sin^2(\alpha) - J_{INT}\cos(\beta-\alpha) \qquad (2.13.1)$$

Here H is the applied field, M_{FM} is the saturation magnetisation of the F layer, x_{FM} and x_{AF} are the thicknesses of the ferromagnetic and antiferromagnetic layer respectively. K_{FM} and K_{AF} express the anisotropy of the two materials and J_{INT} is the exchange energy per surface unit of the interface. The three angles α, β and θ describe the angles between the favourable anisotropy axis (assumed to be the same for K_{FM}, K_{AF} as the system is considered collinear), and the magnetisation of the two materials as well as the applied field as shown in the figure 2.17.

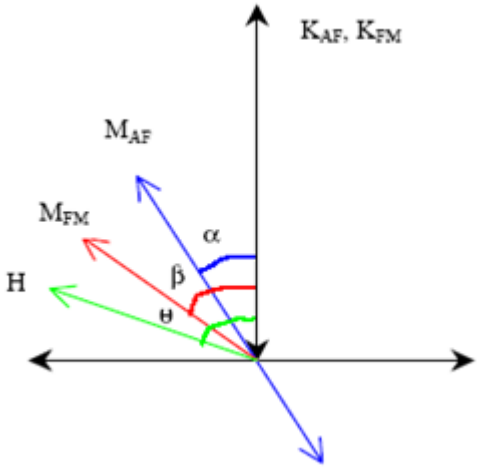

Figure 2.17: Diagram of the angles that are involved in an exchange bias system. Angles α, β, ϑ are the angles between the favourable anisotropy axis of a collinear system and the saturation magnetisations of the AF, of the FM and the external field H respectively.

The energy of the system, as derived from equation 2.12.1, depends on four factors, as shown by the four terms of which it is composed. The first term derives from the effect of the applied field on the ferromagnetic material, the second and the third term are involved due to the anisotropy of the ferromagnetic and antiferromagnetic material respectively, and the latter term results from the interface coupling of the two materials.

Assuming that the AF material exhibits a large anisotropy, the spins of the AF layer do not rotate depending on the field. This means that they remain arranged along the favourable axis of the AF material (Figure 2.18) such that $\alpha \sim 0$ and $\sin^2(\alpha) \sim 0$. Furthermore, since the magnetic field is applied along the favourable axis $\theta \sim 0$, the equation of energy becomes:

$$E/S = -HM_{FM}x_{FM}\cos(-\beta) + K_{FM}x_{FM}\sin^2(\beta) - J_{INT}\cos(\beta) \qquad (2.13.2)$$

Because $\cos(-\beta)=\cos(\beta)$ one can take:

$$E/S = -\left(HM_{FM}x_{FM} - J_{INT}\right)\cos(\beta) + K_{FM}x_{FM}\sin^2(\beta) \qquad (2.13.3)$$

That can be written as:

$$E/S = -(H - J_{INT}/M_{FM}x_{FM})M_{FM}x_{FM}\cos(\beta) + K_{FM}x_{FM}\sin^2(\beta) \qquad (2.13.4)$$

This expression can be associated with a system with uniaxial anisotropy, showing a hysteresis loop displaced by an amount: $H_{ex} = \frac{J_{INT}}{M_{FM} \cdot x_{FM}}$ (2.13.5)

where H_{ex} is the measured exchange field [40], J_{INT} is the exchange energy per area unit of the interface, M_{FM} is the saturation magnetisation and x_{FM} the thickness of the ferromagnetic layer. This model predicts values for H_{ex} by much greater than the experimental results by a factor of 20.

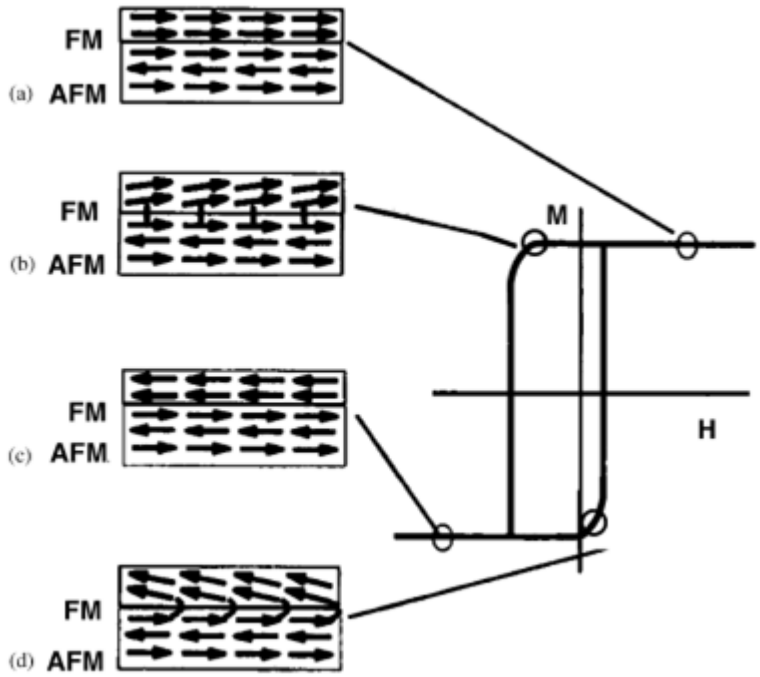

Figure 2.18: Schematic diagram of the spin arrangement in an FM-AF system at different stages of a displaced hysteresis loop due to the high K_{AF} of the system [40].

The mesoscopic model category includes those models that take into account in one way or another the probability that there are differences in the spin order within the x-y plane. The main model used as a typical example of a mesoscopic model is that of Malozemoff [41]. This model, based on the arguments developed by Imry and Ma [42] and using the Random Field Model for FM/AF exchange systems, included the possibility of an incomplete two-layer interface. The roughness of the material interface and possible imperfections in this region produce a field of random direction and intensity that leads to separation of the AF layer into areas (AF domains) that differ from the already mentioned ferromagnetic regions. These antiferromagnetic areas have walls that extend vertically to the interface with the FM (Figure 2.19) and have a wall size given by the relationship:

$$\delta_{AF} = \pi \left(\frac{A_{AF}}{K_{AF}}\right)^{1/2} \qquad (2.13.6)$$

with K_{AF} the anisotropy and A_{AF} the exchange stiffness of the antiferromagnetic layer.

The imbalance between the atomic magnetic moments at the interface of these regions, due to statistical distribution, creates free magnetic moments that are coupled to FM, resulting in the phenomenon of exchange bias with H_{ex} values smaller this time and closer to the experimental ones. Among the most important factors influencing exchange bias are the thicknesses of the thin film ferromagnetic layers. This model predicts that for very thin layers of AF material the intensity of the H_{ex} increases as the thickness x_{AF} of the antiferromagnetic layer decreases [41].

In addition, several studies to date [39], [43]–[45] have shown that both H_{ex} and the value of H_C in FM/AF bilayers give an inverse dependence on the thickness of the ferromagnetic layer. The original models predicted a linear dependence of H_{ex} on the inverse of the thickness of the ferromagnetic material [41] such that:

$$H_{ex} \propto \frac{1}{x_{FM}} \qquad (2.13.7)$$

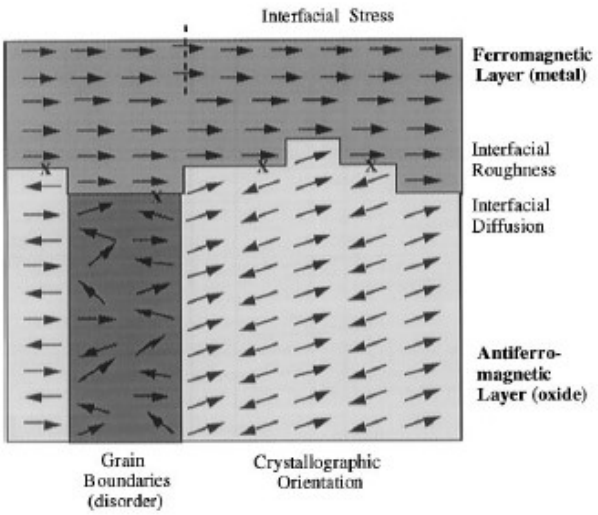

Figure 2.19: Illustration of individual defects and roughness at the AF-FM interface as well as the formation of areas in the AF layer (different shades). With x are noted the interfacial spins coupled in an antiferromagnetic way [46].

Finally, microscopic models are called those models that take into account in detail the spin configuration of each atom (or groups of atoms) separately within the volume of a system in the x, y and z directions. In this direction there are various kinds of approaches such as Monte Carlo simulations [47] and micro-magnetic computations [48]. One of the most pioneering theoretical modelling work of this kind was done by Koon [49].

Although a more important and more relevant model to our work is this from Fulcomer and Charap [36]. They undertook both experimental and theoretical studies of exchange bias in permalloy films by isolating the AF grains on the surface of the films through a treatment with acid vapour which progressively oxidised the nickel in the alloy. They observed a relation between the exchange bias of such systems with both the grain size and the number of grains of the AF material. In order to support their results, they performed simulations based upon a granular reversal model analogous to a Stoner–Wohlfarth system, which gave good agreement with experimental observations. In particular, Fulcomer and Charap predicted that the exchange field from FM acting on AF would result in thermally activated changes in the orientation of the AF sublattices causing variations in the observed value of H_{ex} [50]. One important feature of this model is that it considered a wide range of particle sizes and shapes within the AF resulting in a wide variation of anisotropy and coupling energies. The particle size distribution was assumed to be such that all values are equally probable up to some maximum and that there were no larger particles. They found that it was important to consider a distribution of particle size although the exact form of that distribution was not important. This model was able to predict the temperature dependence of H_{ex} and H_C over a wide range of temperatures even above T_N.

2.14 The York model of exchange bias

A later model that was introduced by O'Grady et al. with his review in 2010 [50] takes into account thermal effects in the exchange bias systems although original papers were published from 2006 [32],[21], [51]. Although not the first one it managed to achieve control of thermal activation both during measurement and prior to them [36],[52],[53]. By controlling the initial state of the AF film, allowed for highly reproducible measurements. It

managed to take into account the grain size distribution of the AF layer from which it derived the magnetic and thermal of the exchange systems. The energy required to reverse such an AF grain is:

$$\Delta E = K_{AF} V \left(1 - \frac{H^*}{H_K^*}\right)^2 \quad (2.14.1)$$

where K_{AF} is the anisotropy of AF, H^* is the exchange field from the FM layer and H_K^* is a pseudo anisotropy field[50]. The model also takes into account the relaxation time τ of the AF grain which is the mean time before the energy barrier is exceeded and is given by the Néel – Arrhenius law:

$$\tau^{-1} = f_o e^{-\Delta E/kBT} \quad (2.14.2)$$

where ΔE is energy barrier, k_B is the Boltzmann's constant, T is temperature and f_0 is an attempt frequency with a typically value of 10^{12} s^{-1} as shown by Vallejo Fernandez et al. [54]. The grain sizes considered in this approach are between 5 and 15 nm.

If the measurement time is much longer than the relaxation time then the magnetisation will flip several times during the measurement something which results in a superparamagnetic behaviour of FM). If on the other hand relaxation time is much less than measurement time t_m, the particle is blocked in its initial state and does not reverse. As a result, there is a time and also a temperature dependence of the reversal mechanism. Thus, the temperature at which the relaxation time equals the measurement time defines the so-called blocking temperature of a given grain given by:

$$T_B = \frac{\Delta E}{k_B \ln(t_m f_0)} \quad (2.14.3)$$

Due to the fact that the model is based on Stoner–Wohlfarth theory, for particles small enough to be single domain and $\frac{H^*}{H_K^*} << 1$ because for an ideal medium the anisotropy field H_K is maximised by increasing the total anisotropy K_U or reducing the saturation magnetisation M_S, the magnetic rotation is assumed to be coherent and activation barrier is given by:

$$\Delta E = K_{AF} V_g \quad (2.14.4)$$

where K_{AF} is anisotropy and V_g the grain volume of AF. Thus, for a given temperature one can estimate the grain sizes that will overcome the energy barrier to reversal as:

$$V_g = \frac{k_B \ln(t_m f_0) T}{K_{AF}} \quad (2.14.5)$$

Therefore, the thermal activation process used to set the AF layer is shown in Figure 2.20.

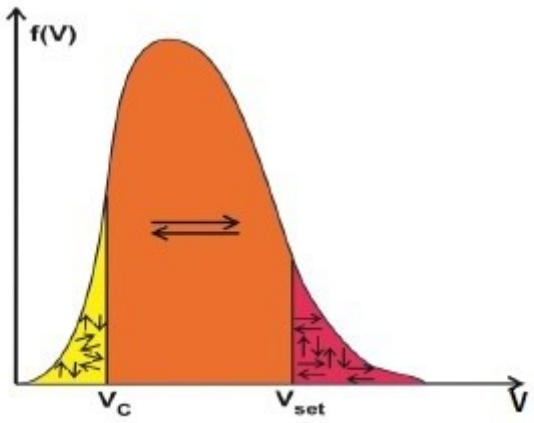

Figure 2.20: Schematic diagram of the AF grain volume distribution. In yellow and purple regions the grains are not set and only the main proportion of grains in the orange area are set [50].

After the sample is set at a setting temperature T_{set} over a time t_{set} it is cooled back to a measurement temperature T_{ms}. Some of the AF grains are not thermally stable and are labelled in yellow in Figure 2.20. The yellow region when $V<Vc$ is where the AF grains are too small and are not thermally stable. This is analogous to superparamagnetic particles, [50]. For the grains with $V>V_{set}$ the grain volume is too large and cannot be set by the exchange field from the F layer at the temperature T_{set}. Hence the AF grains that contribute to the exchange bias are those with $V_{set}>V>V_c$. H_{ex} is then given by [50]:

$$H_{ex} \propto \int_{Vc}^{Vset} f(V)dV \quad (2.14.6)$$

where V_c and V_{set} are calculated from 2.14.5 at T_{ms} and T_{set} respectively. There is another important temperature which one has to consider in the York protocol called non-activation temperature or T_{NA} which is lower than T_N of the bulk materials and above which all grains are thermally active. Below T_{NA} for a given timescale the AF film is not thermally active. The

existence of T_{NA} means that measurements at this temperature are highly reproducible and not dependent on the timescale.

Vallejo-Fernandez et al. [50] calculated the exchange bias as a function of the AF grain diameter. The grain volume varied by both lateral grain size and layer thickness. The AF grain volume distribution is shown in Figure 2.21a. This was achieved measuring more than 500 grains manually using an equivalent circle method. In Figure 2.21b the lines correspond to the theoretical values of H_{ex} which were calculated using Equation (2.14.6). The parameters used in this calculation were T_{ms} =293K, t_{ms}=1800 s, T_{set}=498K and t_{set}=5400 s. The points correspond to the experimental data. The experimental data shows an excellent fit.

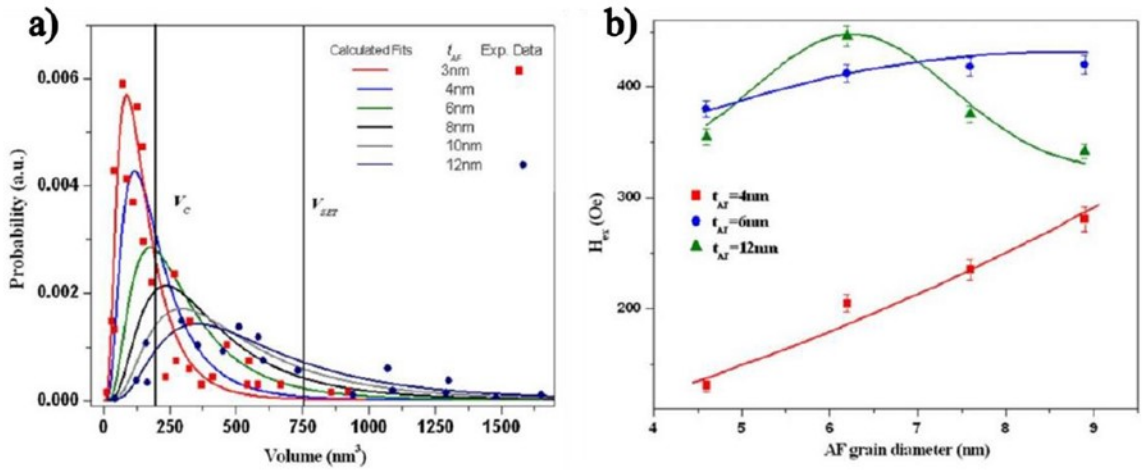

Figure 2.21: a) Grain volume distributions for the samples with different AF thickness and b) Exchange bias as a function of AF grain diameter for 3 different thicknesses of the AF layer [50].

Another approach was to plot the dependence of H_{ex} on grain volume with AF thickness and test if equation 2.14.6 predicted it. The samples were set using a positive saturation field of 1 kOe at 498K for 90 minutes. The hysteresis loops were then measured at room temperature where there was no thermal activation. The data points were fitted with theoretically using equation 2.14.6. The figure shows H_{ex} increases rapidly as the thickness of AF layer increases. The peak was found using a thickness of 8nm of AF layer and H_{ex} decreases using thicker AF layers. This result can be explained using Figure 2.21a. It can be seen that the

area under the 8 nm curves between V_c and V_{set} is the largest. Hence according to the model, the largest exchange bias was measured using 8 nm thick AF layer.

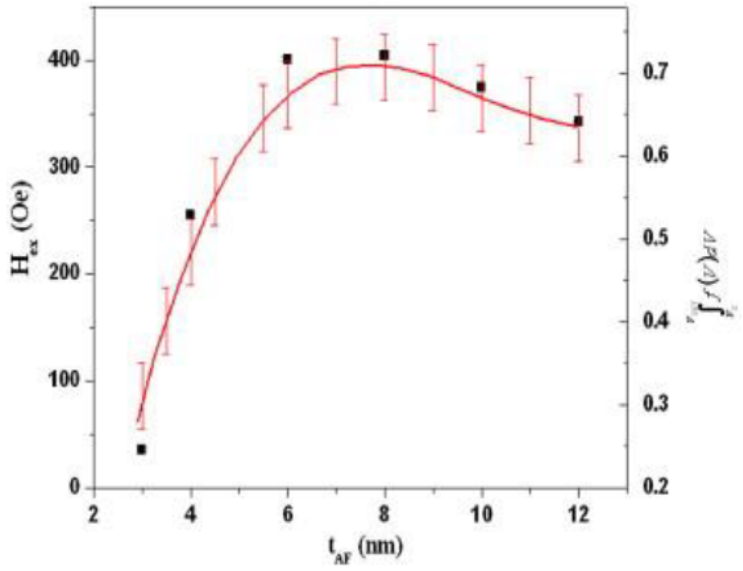

Figure 2.22: Experimental measurements and theoretical fitting of the dependence of H_{ex} and grain size on the different layer thickness as predicted from eq. 2.14.6 [50].

Another measurement process for the York model was developed by Vallejo-Fernandez to determine the anisotropy of AF [51]. Measurement of K_{AF} requires controlling how much of the AF layer is contributing to H_{ex} and accounting for the interface coupling. The sample is initially heated to a setting temperature T_{set} in an applied field for a time t_{set}. During the setting time the FM layer is saturated. The sample is then field cooled to a temperature T_{NA} where there is no thermal activation of the AF grains. The sample is then heated to thermal activation temperature T_{Act} in a reverse applied field for a time t_{Act} and finally cooled again to T_{NA} where the measurement of the hysteresis loop is being made starting from negative saturation to overcome the training effect. There is a point in figure 2.20 where $H_{ex}=0$ is satisfied by the following equation

$$H_{ex}(T_{act}) \propto \int_{T_{act}}^{\infty} f(T_B)dT_B - \int_{0}^{T_{act}} f(T_B)dT_B = 0 \qquad (2.14.7)$$

At this point a fraction of AF grains is thermally active in the opposite sense to the original setting process and this is where the median blocking Temperature exists $\langle T_B \rangle$ and as a result the grain volume is given by $\langle V_g \rangle$. Using equation 2.14.5 one can obtain:

$$K_{AF}(<T_B>)=\frac{\ln(tf_0)}{<V_g>}k_B < T_B > \quad (2.14.8)$$

The value of $<T_B>$ can be obtained by the so-called blocking curve where H_{ex} is plotted against T_{act} (Figure 2.23).

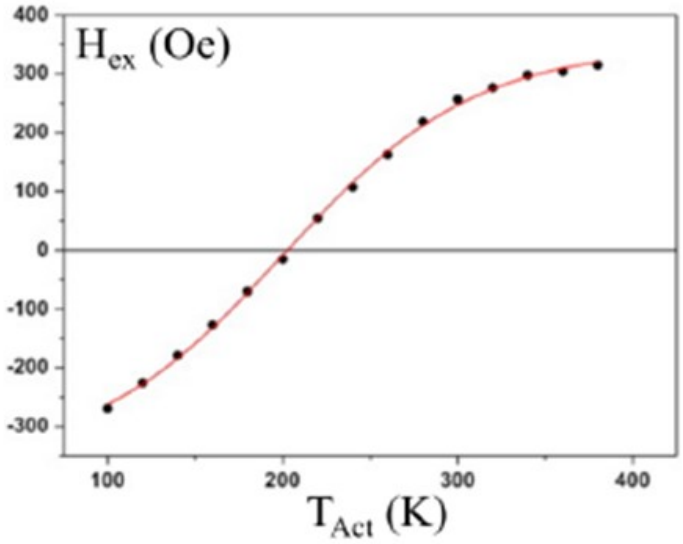

Figure 2.23: Characteristic curve used to measure the blocking temperature T_B. The point in which the curve crosses the 0 value of H_{ex} defines the T_B [50].

In Figure 2.23 the sample was set using a positive field. The curve is not flat at the beginning which indicates that the smaller AF grains were not thermally stable at T_{NA}. At the point where H_{ex} is equal to zero there are equal fractions of the AF grain volumes orientated in opposite directions. The blocking temperature shown in Figure 2.23 can be differentiated with respect to T_{Act} giving a Gaussian like distribution of $f(T_B)$.

2.15 Literature review of perpendicular exchange bias

Most of the literature in perpendicular exchange bias (PEB) is referring to multilayer systems but some of them have studied bilayer systems like CoPt/IrMn bilayer. In this specific work Tsai et al. [55] observed several unusual features:

i. The PEB was spontaneously established without any external magnetic field treatments and the shift was towards positive fields
ii. Single shifted loops were obtained rather than double shifted ones
iii. The films grown or subjected to post annealing under external magnetic field showed a reduction of the PEB effect from H_{ex} = 290 Oe to H_{ex}=197 Oe
iv. The spontaneous PEB effect reduction was accompanied by a reduction in perpendicular coercivity H_c from 1024 Oe to 632 Oe.
v. The thickness dependence of H_{ex} and H_C was studied showing that they were inversely proportional to FM layer thickness.

The results of X-ray diffraction revealed the formation of IrMn (111) texture. Figure 2.24 shows Out-of-plane hysteresis loops obtained at RT for the film samples with and without IrMn layer. It corresponds to the spontaneous perpendicular exchange bias effect since no field cooling process or any additional treatments were applied.

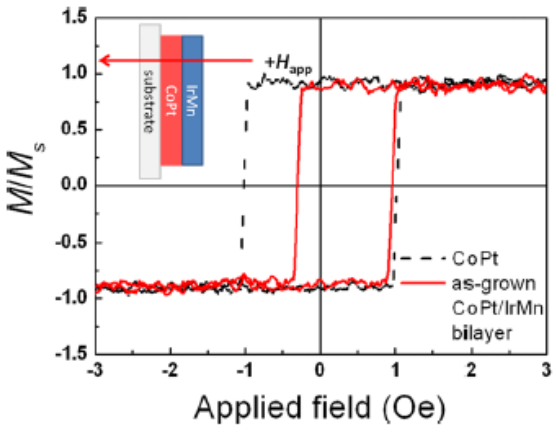

Figure 2.24: Picture showing the spontaneous PEB effect without the need for any field cooling [55].

Another bilayer studied for PEB was the CoFe/IrMn system by Chen et al. [56] They demonstrated a robust PEB effect as a function of AF layer. The samples were Ta (5 nm)/Pt (5 nm)/CoFe (0.8 nm)/IrMn (t_{IrMn})/Pt (2 nm) with $0<t_{IrMn}<12$ nm. The loops had both positive and negative loop shifts. The H_{ex} reached up to 1000 Oe. The texture of the IrMn was strongly induced along (111). When t_{IrMn} reached 3 nm thickness the PEB disappeared.

Another work which seems to be important for PEB was done by Srinivasan et al. [57] who studied the CoCrPt system coupled to IrMn. In this case he used a double Ru seed layer where the 2nd seed Ru layer was replaced by an AF IrMn layer of varying thickness between 3 and 7.5 nm but it was not subjected to field treatments to study the PEB. In order to grow the IrMn intermediate layer along the desired (111) plane normal 5nm Ta and 7.5 nm Ru were used below the AF layer. They found that the intergranular exchange coupling interactions decrease as the t_{AF} increased. The thermal stability factor (SF) of the recording layer (RL) increased as the thickness of IrMn increased. The coercivity achieved was over 4000 Oe and the average grain size was 6 nm. Figure 2.25(a) shows the Kerr hysteresis loops from the above media samples. Figure 2.25 (b) shows the plot of the change in coercivity H_C, negative nucleation field $-H_n$, and the hysteresis slope a at the coercivity point of the loop.

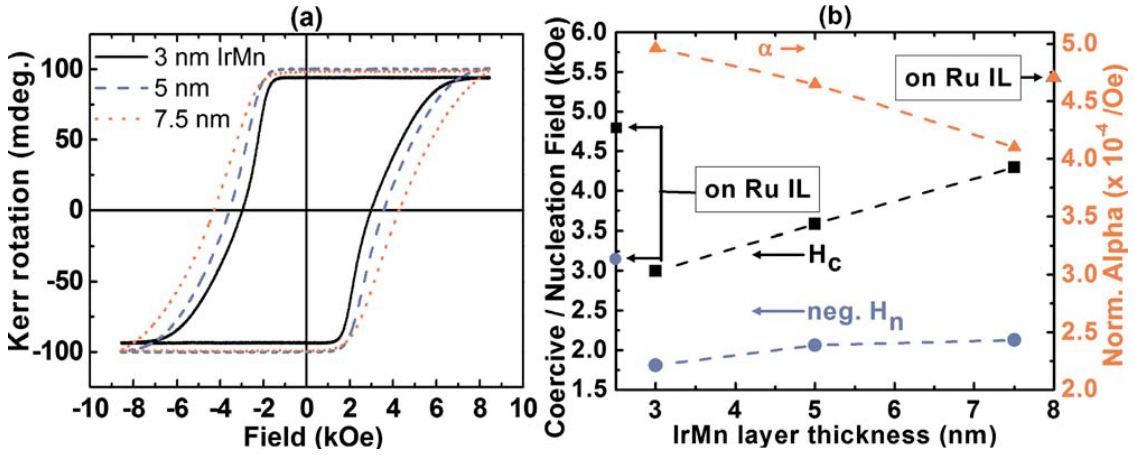

Figure 2.25: (a) Kerr Hysteresis loops and thickness dependence of IrMn with H_c, negative nucleation field H_n and hysteresis slope a [57]

Perpendicular exchange bias has been more extensively studied in multilayer systems and more particular in (Co/Pt) multilayers [58],[59],[60]. Wang et al [61] studied though the CoPt/CoO multilayer system. Here the as deposited multilayer showed strong perpendicular magnetic anisotropy up to a critical CoPt thickness of 4nm with no exchange bias. In particular the coercivity H_C was 525 Oe and the squareness was 0.9. In this case after perpendicular

field cooling the magnetic properties improved with H_C = 4930 Oe and squareness equal to unity. The exchange bias was measured H_{ex} = -1730 Oe. (Figure 2.26).

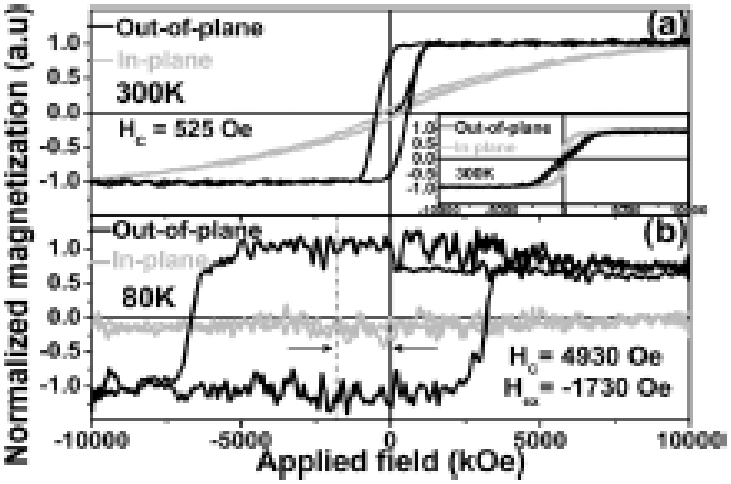

Figure 2.26: Room temperature and low temperature (80K) hysteresis loops of 8 stack multilayer system [61] .

The enhanced PMA after the field cooling was explained with two reasons: (a) due to the coupling of the interface moments and (b) due to the positive magnetoelastic energy because of the remarkable in plane tensile stress originating from the local epitaxial growth (Figure 2.27).

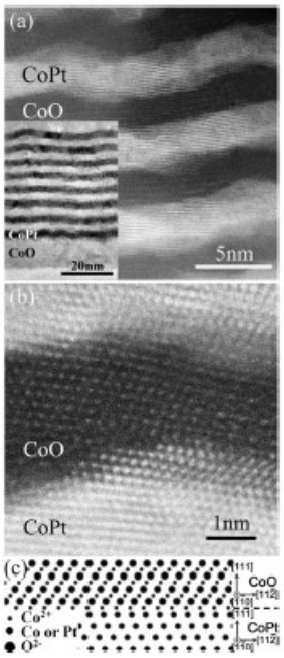

Figure 2.27: STEM image of the interfaces and representation of the epitaxial arrangements of the atoms in the interface [61].

A more application oriented paper was published by Takenoiri et al. [62] where a whole perpendicular hard disk drive was studied using Co-Fe as the recording layer. There, the an antiferromagnetic IrMn pinning layer was applied to reduce the spike noise that originates from domain walls in the Co-Zr-Nb soft magnetic top layer that is used in these discs. The full structure was: glass/Ta(5 nm)/NiFeCr(5 nm)/IrMn(5 nm)/CoFe(2 nm)/CoZrNb(100 nm). The media was heated above the blocking temperature T_B of IrMn and cooled rapidly in a magnetic field. H_{ex} reached a maximum value at Co-Fe thickness of 1.5 to 2.0 nm whereas the H_c value remained almost constant. Blocking Temperature was 285^0C and exchange coupling energy J_{ex}=0.22 erg/cm^2 was obtained by arranging CoFe layer between IrMn and CoZrNb films as calculated from the relation $Jex=M_{soft}t_{soft}H_{ex}$, where M_{soft} is the magnetisation of the soft CoFe layer and t_{soft} the thickness of the soft CoFe layer. In this way the total amount of noise generated from the soft magnetic layer decreased as the exchange bias field increased. Figure 2.28 shows the electrically measured surface of the medium that was heated above Blocking Temperature T_B and then cooled in the magnetic field after all layers had been deposited.

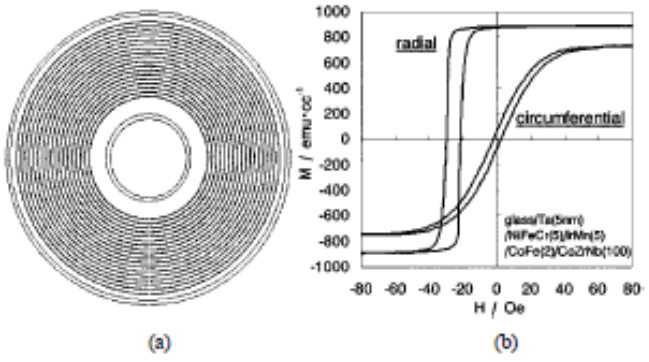

Figure 2.28: Electrically measured surface of the medium heated without recording film (a), and M–H loop of the part surrounded by a square in the left image (b). The SUL (soft under layer) is pinned by the AFM layer [62]

Finally Hashimoto et al. [63] and Hosoe et al. [64] studied the influence of various binary systems used as fcc bases for the nonmagnetic intermediate layer (NMIL) for granular perpendicular magnetic recording media. The stacking was glass/NiFeCr (20 nm)/NMIL (20 nm)/CoCrPt-SiO_2 (16 nm). In Figure 2.29 it is suggested that the increase in H_c and squareness achieved by Cr addition to fcc NMIL is related to an increase of the perpendicular magnetic anisotropy energy of the overlying medium.

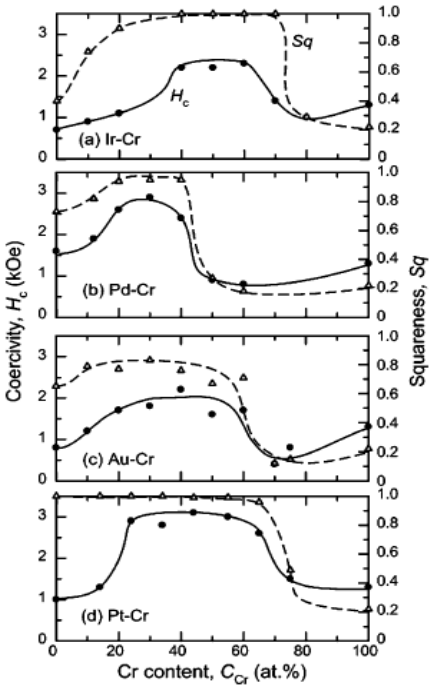

Figure 2.29: Dependence of Hc (solid line) and Sq (broken line) on Cr content of NMIL for glass/NiFeCr (20 nm)/NMIL (20 nm)/CoPtCr–SiO2(16 nm) film with (a) Ir–Cr, (b) Pd–Cr, (c) Au–Cr, or (d) Pt–Cr NMIL [63].

Finally, a more relevant and recent work regarding perpendicular exchange bias was done in the same lab by Elphick et al. [7] in 2016. Kelvin Elphick managed to take advantage of the texture of the IrMn be oriented in the perpendicular direction and using a Co interlayer in a multilayer structure like in Figure 2.30 managed to achieve H_{ex}= 450 Oe with both coercivities lying in the negative axis following a setting at 500K in a positive field of 20 kOe.

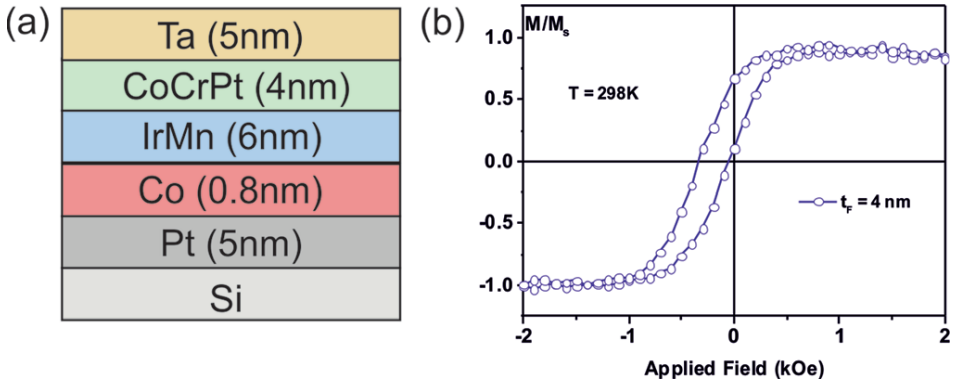

Figure 2.30: a) Sample structure and b) room temperature hysteresis loop for the system studied by Elphick et al. work [7]

Studies were done in order to achieve the optimum thicknesses of the FM and AF layers. In Figure 2.29 (a) the optimum thicknesses are used.

3. Experimental techniques

This chapter describes the method and techniques used in the current work to produce the thin film multilayer samples in one hand and to characterize them structurally and magnetically on the other hand. The production of the samples was done by a Plasma Quest Ltd. High Target Utilization Sputtering system (HITUS). The structural characterization was done by a Rigaku X-Ray diffractometer (XRD) to justify the presence of different layers and an additional operation of the same system as an X-Ray reflectometer (XRR) was used to measure the thicknesses of the different layers. The magnetic characterization was done with an Alternative Gradient Force Magnetometer (AGFM) initially to obtain quick loops in order to evaluate the samples qualitatively regarding the squareness and coercivity and for more detailed measurements a Lakeshore Vibrating Sample Magnetometer model 8600 (VSM 8600). For the study of the presence of perpendicular exchange bias a Microsense Ltd. VSM Model 10 was used which has some different characteristics that will be described in this chapter.

3.1 Sputtering of thin films

Sputtering is a well-established phenomenon and has been known for over 40 years [65]. The entire process is based on the natural process of removing atoms and molecules from a target material by bombarding the surface with ionized high-energy gas atoms. It is mainly used for the deposition of thin film materials. There are many different methods of sputtering thin films including direct current (DC) sputtering and radio frequency (RF) sputtering. A well-known method for sputter deposition is magnetron sputtering[66]. Placing magnets below the target, ensures the confinement of electrons near the target and improves drastically ionization probabilities. Then the positive Ar ions are led to the target with high kinetic energies and ion bombardment of the target follows which causes atoms or particles to detach and create a cloud. These atoms-molecules then diffuse to the area of the substrate and create a homogeneous film (Figure 3.1). The efficiency of the sputtering process depends on the energy of the ionic gases as well as on the mass of both the target material and the gas as well as on the energy connection of atoms to the solid. A series of targets can be placed

in the airtight chamber, making it possible to manufacture multilayer composite materials, including ferromagnetic and antiferromagnetic materials. An important advantage of sputter deposition is that even materials with very high melting points are easily sputtered while evaporation of these materials with other techniques is problematic or impossible. Sputter deposited films have a composition close to that of the source material. The difference is due to different elements spreading differently because of their different mass (light elements are deflected more easily by the gas) but this difference is constant. Sputtered films typically have a better adhesion on the substrate than evaporated films. A target contains a large amount of material and is maintenance free making the technique suited for ultrahigh vacuum applications. Sputtering sources contain no hot parts (to avoid heating they are typically water cooled) and are compatible with reactive gases such as oxygen. Sputtering can be performed top-down and advanced processes such as epitaxial growth are possible.

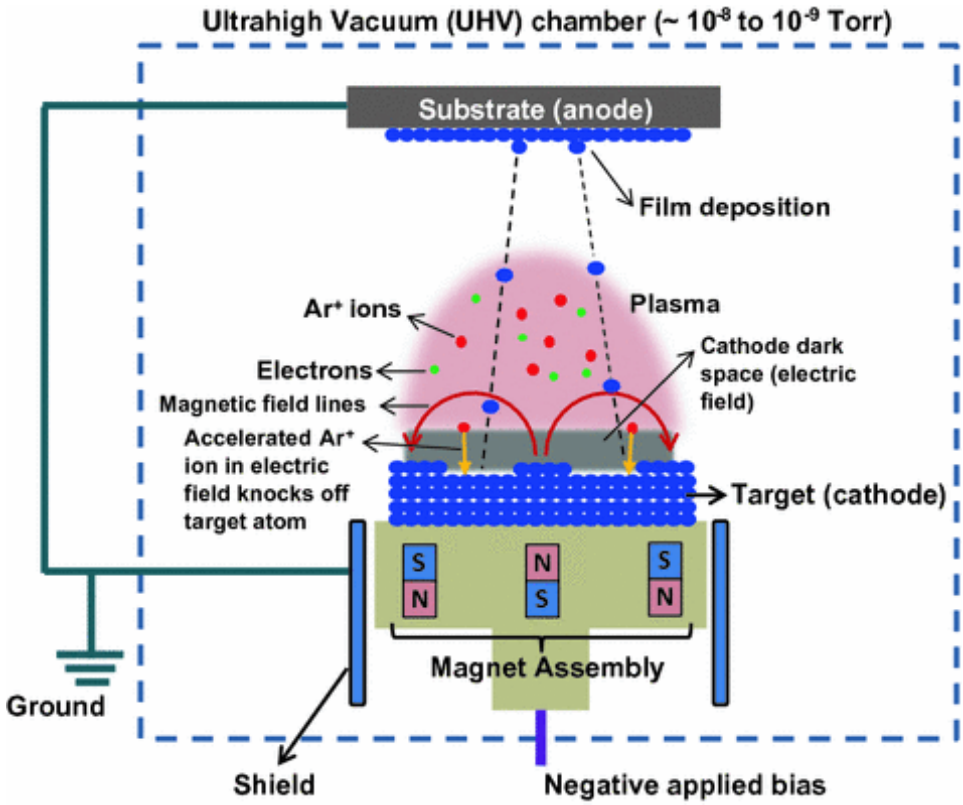

Figure 3.1: Schematic representation of the sputtering process of thin films including ionization, impact of secondary electrons and confinement by magnetic flux [64]

3.2 High Target Utilisation System (HITUS)

A more modern and efficient approach of sputtering is through the HITUS system. One of the basic characteristics that differentiate it from traditional sputtering methods is that the production of the plasma is done in a separate small chamber away from the targets which simplifies the problem of economic use of targets and the control of the plasma beam. Inside the side chamber is placed a RF antenna of 3 KW power output and 13.56 MHz frequency operation through a 3 turn coil which generates an inductively coupled plasma[21]. As shown in Figure 3.2 there are two pairs of electromagnets on this system the launch and steering electromagnets.

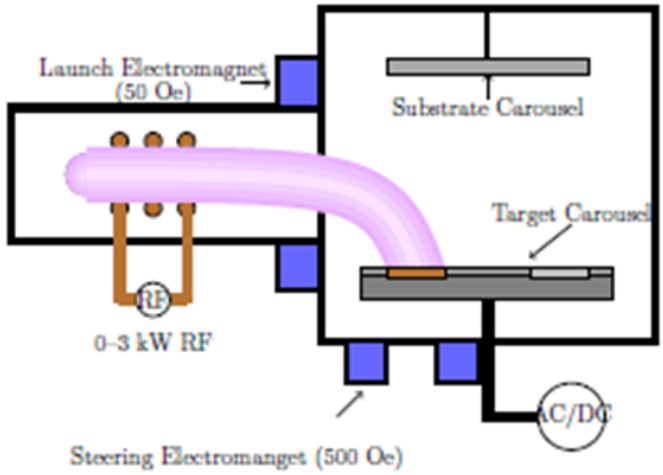

Figure 3.2: Schematic illustration of the HiTUS system with the 2 pairs of electromagnets and the RF antenna in a separate chamber [18].

The first one helps to accelerate the electrons of the plasma in a helical motion leading to a large number of ionising collisions resulting in highly dense beam. For this reason, the field of the launch magnets is 50 Oe applied coaxially to the coil. The second pair of magnets produce a steering DC magnetic field of 500 Oe which confines the plasma into a beam and drives it to the targets with a beam area of 20 cm^2 covering approximately 95% of the target. But still the energy of the plasma directed to the targets is not significant enough to cause detachment of atoms and molecules from the target. This can be achieved by applying a negative bias voltage to the target of the range of -1 to -1000 V. As shown in Figure 3.3 at bias voltages below 100 V one can achieve significant sputtering as the target current saturates

and becomes independent of the bias voltage as shown. But as the bias voltage increases the energy of the ions increase and leads to an increased sputtering rate. Another way to influence the sputtering rate is by varying the RF power applied to the Ar gas or by adjasting the process pressure of the Ar gas.

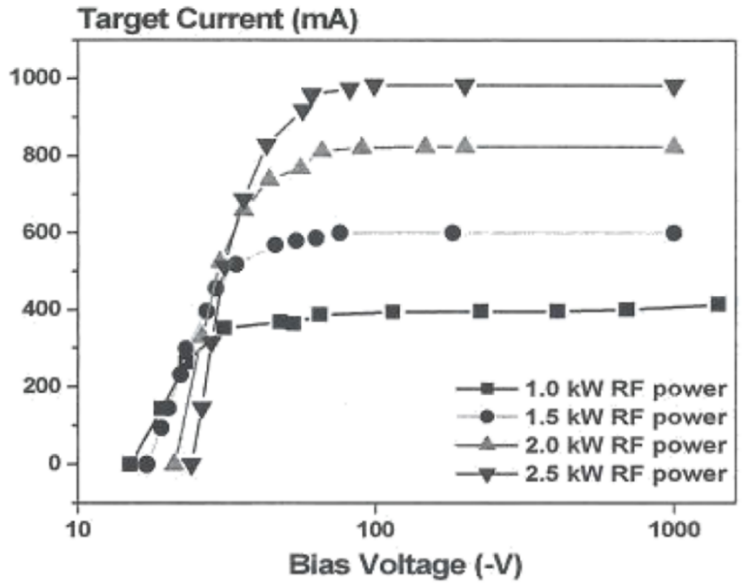

Figure 3.3: Target current vs bias Voltage for different RF powers causing different sputtering rates for the same material [67].

By influencing the sputtering rate in these 3 ways one can control the median grain diameter D_m as shown in Figure 3.4. By increasing the RF power, bias voltage or the process pressure the energy density of the plasma will grow, increasing the deposition energy. This leads to more mobile atoms and molecules being deposited onto the substrate increasing the size. The ionization energies achieved by this system are of the order of 10^{12} ions/cm^3 compared to the typical magnetron plasma which is 2 order of magnitude lower (10^{10} ions/cm^3) [67].

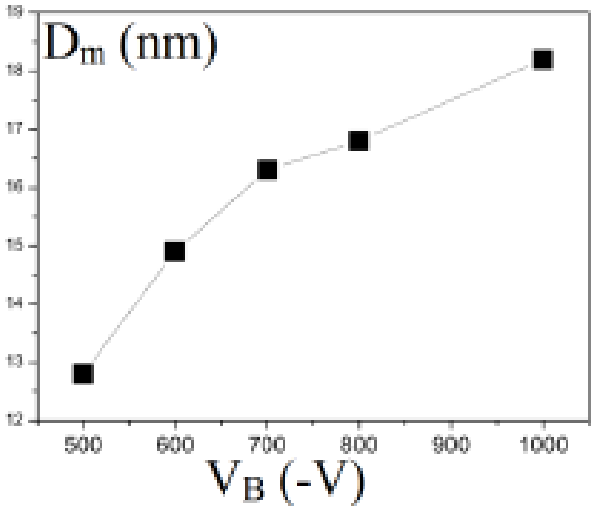

Figure 3.4: Dependence of median grain diameter on bias voltage showing control of grain size through the HITUS system [21].

Eight different targets can be placed on the multiple target carousel, which is driven by a stepper motor. As shown in figure 3.2 there is a substrate carousel above which can hold up to six different holders consisting of maximum 4 substrates and 2 TEM grids each[67]. The large spacing of 30 cm between the target and substrate offers several advantages. Firstly, a large cone of sputtered material is produced covering a wide area. As a result, the deposition at the substrate carousel is so uniform that TEM grids grown alongside a Si substrate will exhibit exactly the same grain size distribution. Secondly, the deposition temperature is kept near room temperature, allowing for controlled deposition. The whole process is monitored by a thermocouple.

There are several steps before the actual deposition including target and substrate cleaning. First the targets are sputtered for 60 seconds to remove any possible oxidised layers and contaminants from the surface of the targets. Then one can switch off the steering magnet and allow the plasma to diffuse into the chamber allowing the cleaning of the Si substrates, whose picture in figure 3.5 is showing their size which was 5 mm×5 mm.

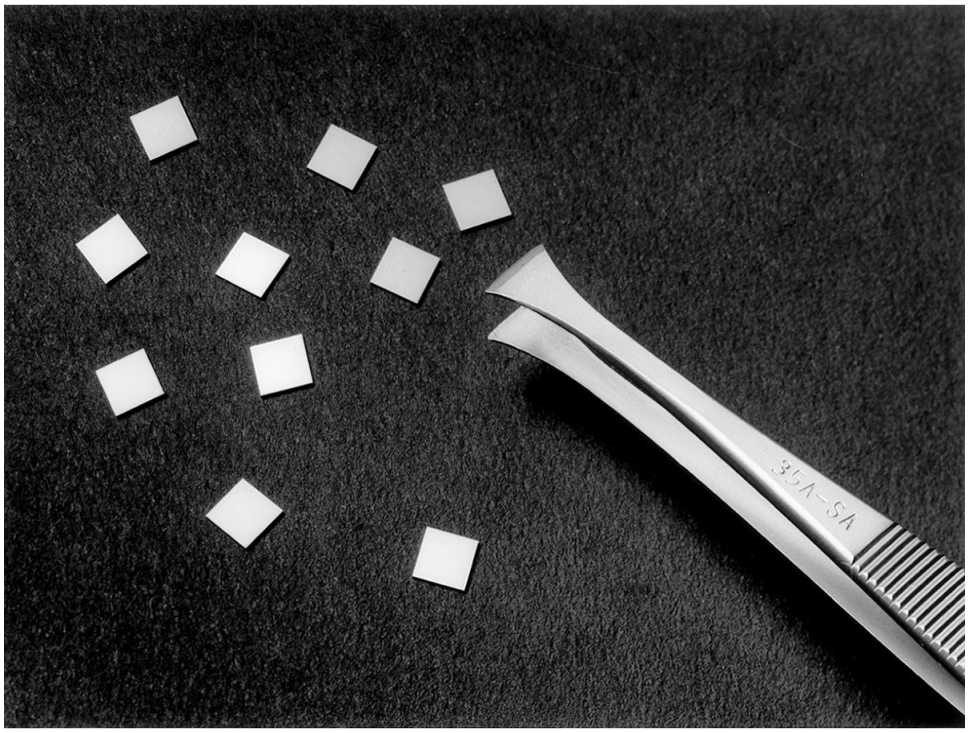

Figure 3.5: A picture showing the silicon substrates of size 5 mm × 5 mm used in the lab.

The shutter opens and each holder is exposed to the plasma for 60 sec. Before the deposition starts the plasma is conditioned for 20 seconds to achieve stabilization of the Ar pressure. The flow of the Ar gas is controlled by a Mass Flow Controller with pressures in our study ranging between 1.86 – 30 mTorr. A further 10 seconds of pre- sputtering is used to make sure the target is ready and clean. After that the shutter is opening, allowing the material to flow on the substrate surface.

A heater is placed behind the substrate carousel allowing the deposition temperatures to be varied up to 500^0C. The sample can be heated before during or after the growth process allowing control over crystallinity, roughness and grain size.

3.3 X-ray Diffractometer (XRD)

X-rays are electromagnetic radiation with wavelengths of Å, which in the electromagnetic spectrum extend between the gamma ray and ultraviolet regions. The X-ray energy region is perhaps the most used for solid characterisation and structural studies. In addition to diffraction, the main ways of using X-rays falling under the scope of spectroscopy are emission and absorption.

Generally, the interaction of an X-ray not of particularly high energy with a particle gives a result of in-phase elastic scattering, which is perceived as a secondary beam in all directions with maximum intensity in the direction of the incident. With a solid material, however, the situation is different. There the primary beam is scattered simultaneously by many particles and the secondary beams can in some directions within the mass of the solid contribute constructively. This happens if the solid is characterised by a periodic structure. In this case, atomic diffraction phenomena are observed.

Bragg approached the matter by considering that the layers of atoms in a material form crystalline planes that behave as translucent mirrors in X-ray radiation. When an incident X-ray beam of a particular wavelength λ interacts with the crystalline lattice of a material, then through the diffraction phenomenon those reflected rays that satisfy Bragg's law will be amplified while the rest will undergo a destructive contribution. The law of Bragg is [68]:

$$2d \sin\theta_B = n\lambda \qquad (3.3.1)$$

where *n* is the order of the diffraction, λ is the wavelength of the incoming radiation, *d* is the lattice plane spacing and ϑ_B is the angle at which diffraction occurs.

The lattice spacing *d* in a cubic structure is given by:

$$d = \sqrt{\frac{a^2}{h^2+k^2+l^2}} \qquad (3.3.2)$$

where *a* is the lattice constant and *h*, *k* and *l* are the Miller indices specifying the lattice plane. In Figure 3.6 the geometry of the diffraction is given. For each crystalline material with a

particular crystalline structure, a characteristic diffraction pattern results. If the system in which the material is crystallised is known, the Miller indices (hkl) corresponding to the levels where X-rays are reflected can be found, resulting in the peaks in the diffraction pattern.

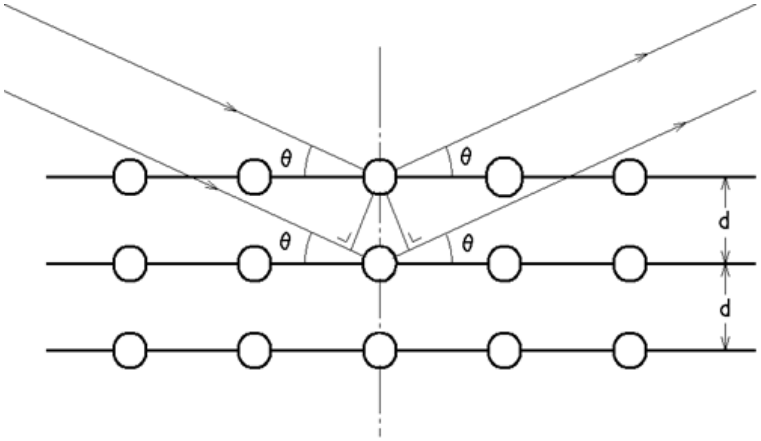

Figure 3.6: Schematic representation of the diffraction of an X-Ray from successive parallel atomic planes. In order for the two rays to be in phase their 2dsinϑ travel distance must be a multiple integer of the wavelength λ_0 of the beam radiation.

The X-Rays used in this work come from a Cu-K_{a1} source with a wavelength of λ= 0.154059 nm. A tungsten (W) cathode is used to generate an electron beam that is accelerated toward a rotating Cu anode whereby electrons interact with the Cu and generate X-rays. A Ge crystal monochromator is used to achieve optimum monochromatic conditions achieving a resolution of 0.01^0.

The device used in this work is a Rigaku Smartlab XRD with a geometry like in Figure 3.7. The system can perform high resolution θ-2θ scans.

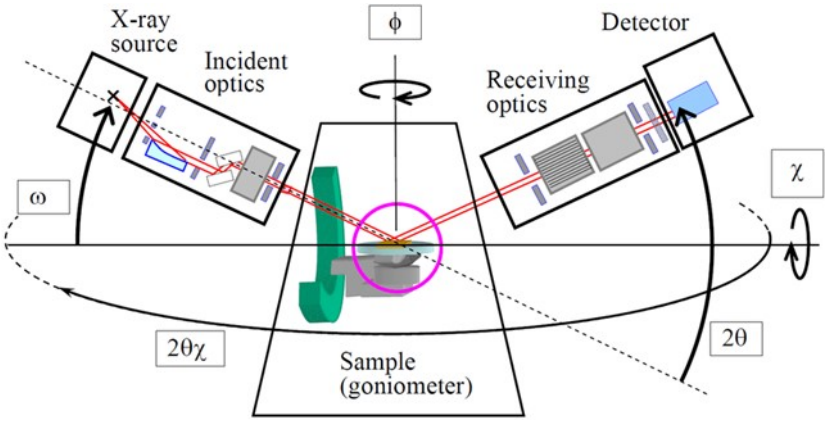

Figure 3.7: Schematic illustration of Rigaku XRD geometry, showing the source, the sample goniometer with relevant geometry and the detector [69].

3.4 X-Ray reflectometry (XRR)

The same Rigaku instrument has another additional operation as an X-Ray reflectometer. From an XRR scan one can obtain information about the density, thickness and roughness of individual layers in multilayer thin films. Apart from the refracted beams in a material the phenomenon of reflection of X-rays occur between different layers. In Figure 3.8 one can see the incident, refracted and reflected X-ray beams in the interface between two layers. The profile of the reflectivity scan depends on the aforementioned factors.

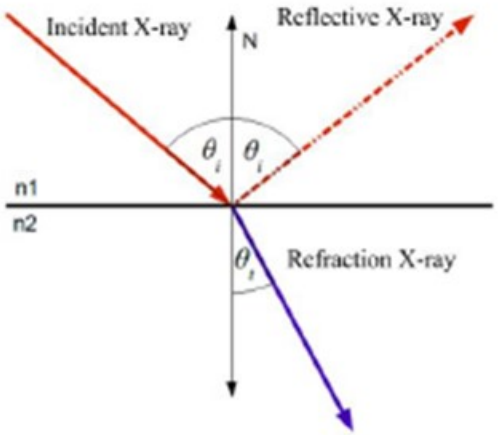

Figure 3.8: Illustration of the important angles in an interface between different materials for incident, refractive and reflective beams [22]

When an incident X-ray reaches the interface below the critical angle a proportion of it is refracted and the rest is reflected with a refractive index in a solid material given by:

$$R^* = 1 - \delta_{R^*} - i\,\beta_R, (0 \leq \delta,\beta) \qquad (3.4.1)$$

where δ_{R*} and β_{R*} can be calculated from the wavelength of the incident X-rays, the composition and density of the material. For normal materials the values of δ_{R*} and β_{R*} are approximately 10^{-6} rad.

When the incident X-ray is at an angle smaller than a critical angle, total reflection occurs. Therefore, the intensity of the reflected X-ray is equal to that of the incident X-ray. However, when the incident angle is larger than the critical angle, refraction and reflection occur. Hence the intensity of the reflected X-rays decreases. An oscillation is observed in the intensity of the X-rays reflected from multilayer samples. This is due to the interference between two reflected X-ray components of the multilayer. The incident angle and reflected

X-ray intensity are then used to measure the composition or density of the materials. Figure 3.9 shows a typical reflectivity scan for a multilayer sample. It also shows the fitting reflectivity profile with relation to different structure parameters after the Gen-X simulation. The period of oscillation represents the thickness of the films. The amplitude of the oscillations depends on the density differences between the films and the substrate and finally the roughness of the film dictates the rate of intensity decrease at the critical angle.

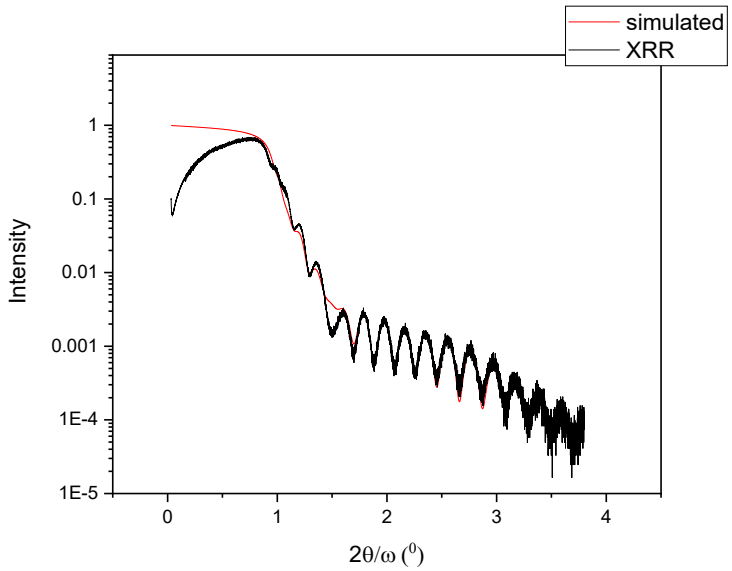

Figure 3.9: An example of reflectivity scan and fitting profile in a multilayer thin film.

After the reflectivity profile of our multilayer is obtained, one can estimate the density, roughness and thickness of each individual layer from a software like GenX through a fitting process calculation. I create a stack in the software with our desired materials and enter different parameters like scattering length of the material and the ones I want to fit. Firstly, I simulate the material and then start the fitting process where the software tries to fit exactly the given profile by changing the values of roughness, density and thickness of each layer. In this way I made the calibration of the HITUS by depositing a monolayer and a bilayer of desired thickness and known materials and then simulating it with GenX to see if the thicknesses were right. Moreover, it was used to estimate the parameters of different series of samples where the magnetic properties differed for each other. Fitting a curve requires a function usually called figure of merit (FOM). It measures the difference between measured curve and simulated curve, and therefore, lower values are better. When fitting, the

measurement and the best simulation are typically represented in logarithmic space. From mathematical standpoint, the χ^2 fitting error function takes into account the effects of Poisson-distributed photon counting noise in a mathematically correct way:

$$FOM = \sum_i \frac{\left(x_{simul,i} - x_{meas,i}\right)^2}{x_{meas,i}} \quad (3.4.2)$$

However, this χ^2 function may give too much weight to the high-intensity regions. If high-intensity regions are important (such as when finding mass density from critical angle), this may not be a problem, but the fit may not visually agree with the measurement at low-intensity high-angle ranges. Many times, the data can be fitted more easily and more robustly if another FOM is chosen like the logarithmic one used in our fittings:

$$FOM_{log} = \frac{1}{(N-p)} \times \sum_i |\log_{10}(Y_i) - \log_{10}(S_i)| \quad (3.4.3)$$

where the merged data set consisting of all data sets that are marked for use is denoted as Y and the corresponding simulation is denoted as S. A single element of these arrays is indicated by a subscript i. Finally the total number of data points is given by N and p is the number of free parameters in the fit.

3.5 Alternating gradient force magnetometer (AGFM)

The alternating gradient force magnetometer (AGFM) was initially a development of a conventional force magnetometer in which an alternating magnetic field gradient was used to produce an alternating force on a sample with a net magnetic moment [70]. The force, or the displacement produced by the force, can be converted to a voltage by a piezoelectric bimorph and analysed using a lock-in amplifier to distinguish the signal against unwanted background noise. A noise base of better than 2×10^{-8} emu can be achieved with a time constant of 1 sec. This system allows routine measurements to be taken quickly and easily. Figure 3.10 illustrates the basic parts of AGFM.

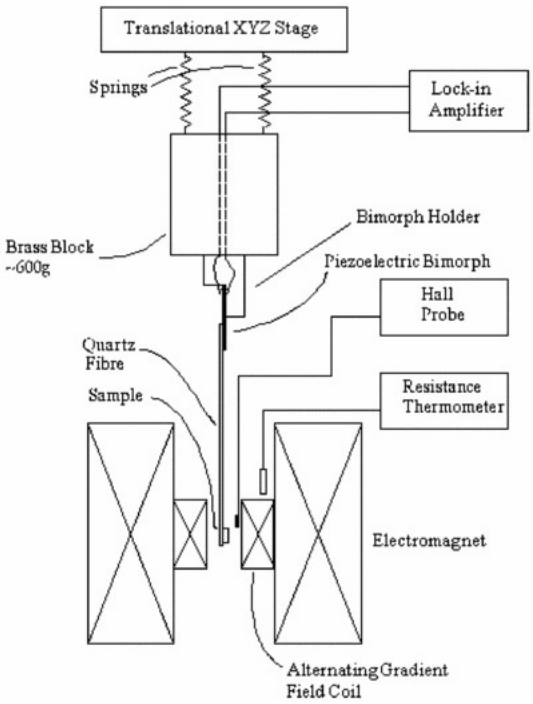

Figure 3.10: Illustration of basic parts of an AGFM including the electromagnets and the piezoelectric bimorph [71].

Apart from the DC field that is generated by an electromagnet to make the actual measurements and can be up to 22 kOe an alternating gradient field is generated by two small coils within the poles of the electromagnet separated by a 12.5 mm distance as shown in the previous figure. The magnitude of the gradient can be set to 0.04, 0.4 and 4 Oe/mm. Due to the nature of the design the probes for in-plane and out-of-plane geometries are different. For in-plane measurements two legs can be attached to the bimorph, one on each side, in order to apply the torque. However, for out-of-plane geometries, which I used in the current work there can only be one fibre and the fibre must be indented into the bimorph itself. The difference between the two is shown in Figure 3.11:

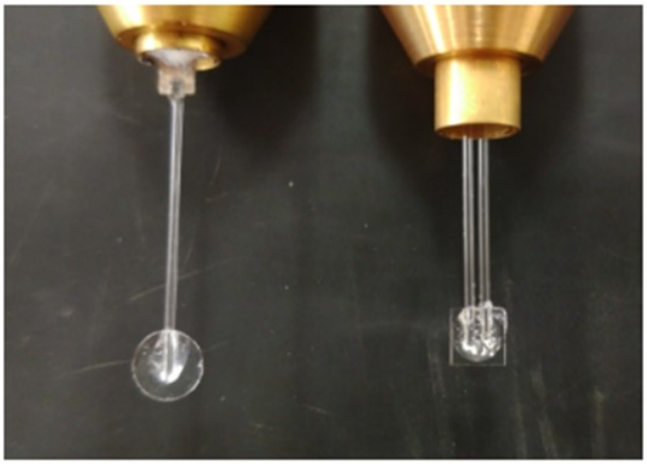

Figure 3.11: Picture of the two different kinds of probes used for perpendicular (left) and parallel (right) measurements respectively [72].

A Model 2900 Princeton Measurement System AGFM was used in this study. I basically wanted to evaluate quickly the squareness and coercivity of our samples so I did not need to calibrate beforehand the instrument although in some cases I did. When the thicknesses varied, I needed the calibration with a 5 mm^2 Pd sample to see how saturation magnetisation varied with thickness while when I just varied the deposition pressures I did not. For the simple case of a quartz cantilever the resonance frequency is given by [73]:

$$f = \frac{1}{2\pi}\,\frac{t}{l^2}\left(\frac{Y}{\rho}\right)^{1/2} \qquad (3.5.1)$$

where t and l are the thickness and length of the cantilever (m), Y is the elastic modulus of the cantilever (Pa), and p is the density (kg/m^3). The mechanical resonance quality factor Q determines the quality of the measurement. In order to make the measurements the probe should have a Q factor above 20.

3.6 Vibrating sample magnetometer (VSM)

For more detailed magnetic measurements in this study I used a vibrating sample magnetometer. Its principle of operation is quite simple while it is based on Faraday's law of induction. For that reason, a magnetised sample by an electromagnet is vibrated vertically near a pair of detection coils. The change in the magnetic flux through the coil induces a change in voltage of the coil according to:

$$E = -N_c \frac{d\Phi}{dt} \tag{3.6.1}$$

where E is the electromotive force, N_c is the number of turns in the coil, Φ is the magnetic flux through the coil for time t. Because of the fact that the total magnetic flux through the coil is a result both of the magnetisation $\vec{M}$ and applied field $\vec{H}$ one can calculate:

$$\Phi = \left(\left|\vec{H}\right| + \left|\vec{M}\right|\right)A_c = \vec{B}\,A_c \tag{3.6.2}$$

where A_c is the area of the detection coil. Thus, the total voltage induced in a coil is:

$$\int E\,dt = -N_c A_c \left|\vec{M}\right| \tag{3.6.3}$$

where there is only the magnetisation M contribution since the external field H is invariant with time t.

In this study I used two different VSMs: a Microsense Model 10 VSM and a Lakeshore 8600 VSM which although they are based on the same principle described above, they have some different characteristics which help us make different kinds of operations and measurements.

The Microsense Model 10 (figure 3.11) has an open circuit continuous flow cryostat that allows measurement from 100 to 700 K using N_2 and Ar. The pole pieces of the electromagnet can create up to 2 Tesla applied field. Moreover, it uses eight detection coils arrayed in four pairs. They are assembled in such a way that they form the x-coils and y-coils, allowing 2 dimensional measurements of magnetisation. The signal from the coils is amplified by two separate lock-in amplifiers. Another characteristic of the Model 10 is that the pole pieces can rotate by ± 540^0 with an accuracy better than 0.1^0. The sample is vibrated by a linear actuator at a frequency of 75 Hz.

Figure 3.12: Picture of a Model 10 Microsense VSM [74].

The 8600 Lakeshore VSM is a more conventional VSM on the contrary. It has a removable cryostat that allows measurement from 4.5 K with He and up to 450 with N_2. A Dewar where the liquid N_2 is stored is used to connect through some pipelines which are pumped down before the use. The pole pieces are stable and can generate a field of up to 2 Tesla. The detection is done by 2 coils with a sensitivity of 15nemu. An advantage is that it can measure much faster loops than the Model 10 with measurement speed of 10 ms/pt but when I try to stabilize it at certain temperatures it takes much more time, around 1 hour more than the model 10, because the cryogenics operation is made both by a PID controller and manually.

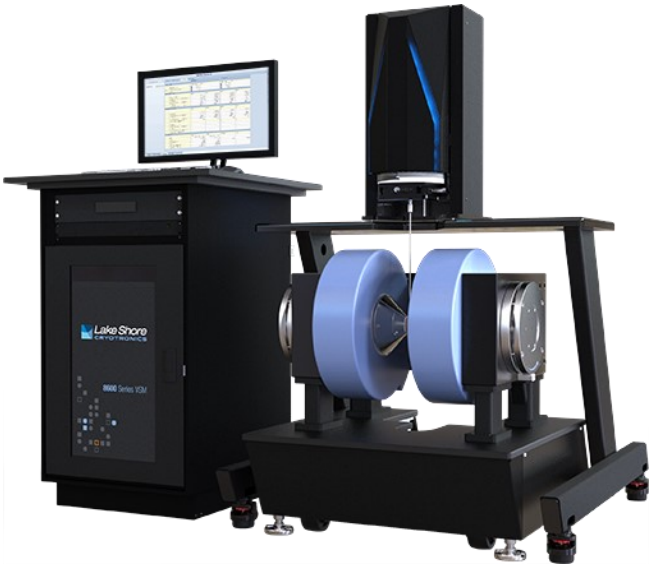

Figure 3.13: Picture of a lakeshore 8600 VSM [75].

4. Experimental Results

4.1 HiTUS Calibration

Before starting any deposition of thin films and measurements, in order to control accurately the thickness of the deposited films, the thickness rate monitor in the HiTUS system was calibrated properly and the indications on the deposition rate monitor were checked to be the right ones. In this case a single layer of Ru 20nm was deposited followed by a bi layer of CoFe 20 nm and Ru 10 nm for reflectivity measurements to be made on them. XRR was used to determine the thickness of the deposited samples and a software called GenX to identify whether the results were fitted properly or not. As a result, Figures 4.1 and 4.2 show the experimental results and calculated fits.

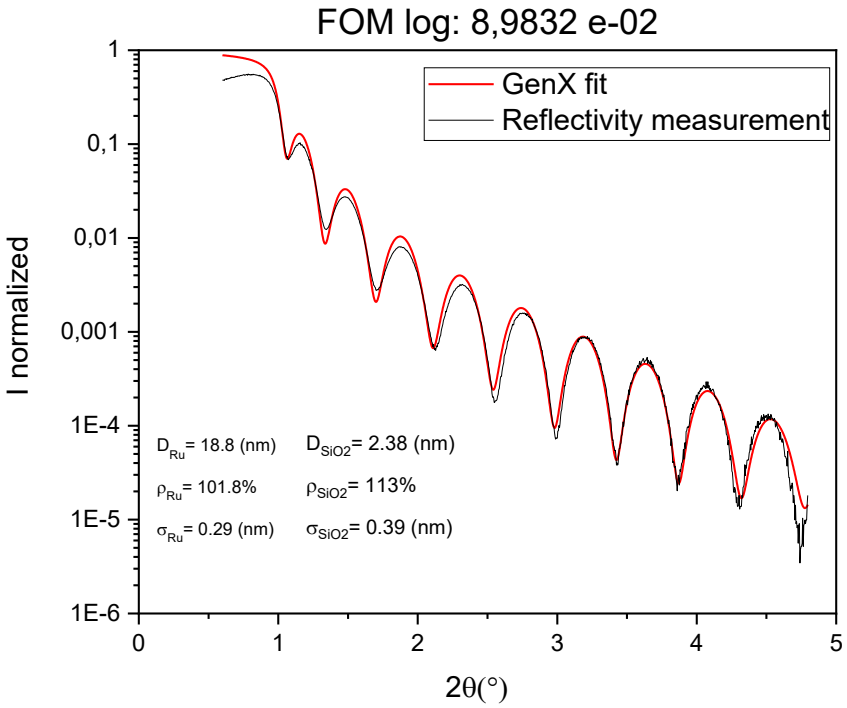

Figure 4.1: Calibration of HITUS through GenX calculations for a known thickness of single Ru layer.

The reflectivity scan was fitted and the values for 3 parameters were estimated. D which is thickness, ρ which is density and σ which is the layer roughness. In the calculation a SiO_2 layer was added at the bottom with the assumption that an oxide layer could form on top of the Si substrate. I got a D_{Ru}=18.8 nm and D_{SiO2}= 2.38 nm which in total are very close to the required value of 20 nm with densities of ρ_{Ru}=101.8% of the theoretical value and

ρ_{SiO2}=113% of the theoretical one. Roughness was small as it was estimated at σ_{Ru}=0.29 nm and σ_{SiO2}=0.39 nm. The results are shown in the following table:

Layer	SiO_2	Ru
D thickness (±0.2nm)	2.38	18.8
ρ density (±2% of theoretical value)	113	101.8
σ roughness (±0.02nm)	0.39	0.29

Table 1: Results for the three parameters of the single Ru layer estimated by the GenX fit.

The figure of merit for the first fitting was FOM_{log}: 8.9832 e-02

The second estimation was done in figure 4.2 as:

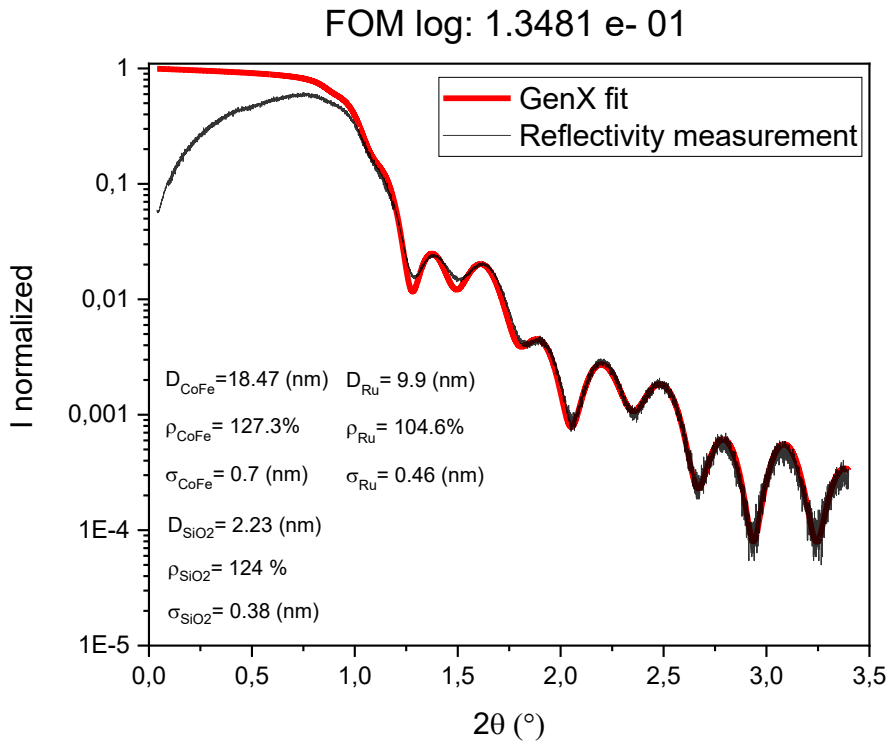

Figure 4.2: Calibration of HiTUS through GenX calculations of a known dual CoFe-Ru layer thickness.

The same process was repeated for a dual layer of CoFe 20 nm and Ru 10 nm and I estimated the 3 parameters for the 2 layers and an additional SiO_2 layer as follows. The fitting was very good and it gave values of thicknesses of D_{CoFe}=18.47 nm D_{Ru}=9.9 nm and D_{SiO2}=2.23 nm with small roughness and a little higher deviation in densities for CoFe. Again, the total thickness is very close to the initially desired of 30 nm. In both cases the densities estimated by the fit are higher than that of the bulk material. A possible explanation for this is that in reflectivity measurements, total reflection is achieved below the critical angle. This critical angle is directly related to electron density which itself is proportional to the average film density. Errors in system alignment can result in a shift of the critical angle which results in errors in density estimations. The Figure of merit for the second fit was estimated as FOM_{log}: 1.3481 e-01.

Layer	SiO_2	CoFe	Ru
D thickness (± 0.2nm)	2.23	18.47	9.9
ρ density (± 2% of theoretical value)	124	127.3	104.6
σ roughness (±0.02nm)	0.38	0.70	0.46

Table 2: Results of the three parameters given by the GenX fit for the dual CoFe-Ru layer used for calibration

As a result, I came to the conclusion that the instrument was well calibrated and ready for depositing the desired multilayer structures. In the following table the comparison between the desired and achieved thickness is given and the deviation in %.

Nominal thickness (nm)	Measured Thickness ± 0.5 (nm)	Deviation (%)
20	21.2	6%
30	30.6	2%

Table 3: Comparison between deposited and measured thickness and calibration deviation factor in % from XRR.

4.2Multilayer Structure preparation

In the current work a series of samples was produced in order to prepare a structure which could be used as a perpendicular exchange biased thin film media. Initially the first deposited layer is a Ta buffer layer to promote amorphous structure so that the next layers can be deposited following independent growth structure from the Si substrate crystal habit. The thickness of the buffer layer is typically 5 nm with deposition pressures of 3 mTorr. The next two layers are the seed layers. The seed layers are deposited at two different process pressures where the process pressure of the second layer is much higher than the first one. This happens for the first layer in order to achieve the desired crystallinity and for the second layer to achieve grain segregation. Thornton's zone [76] model best describes the final morphology of the deposited films in terms of the Ar pressure and the ratio of substrate temperature to the melting point of the sputtered material. Thornton pointed out that low mobility deposition condition (high Ar gas pressure) by sputtering tend to create polycrystalline film, which corresponds to the "zone 1" structure in the well-known Thornton microstructure zone diagram, and leads to fine columnar grains with voided grain boundaries (Figure 4.3). On the other hand, a high mobility deposition condition (low Ar gas pressure) tends to promote a continuous structure of morphology [77].

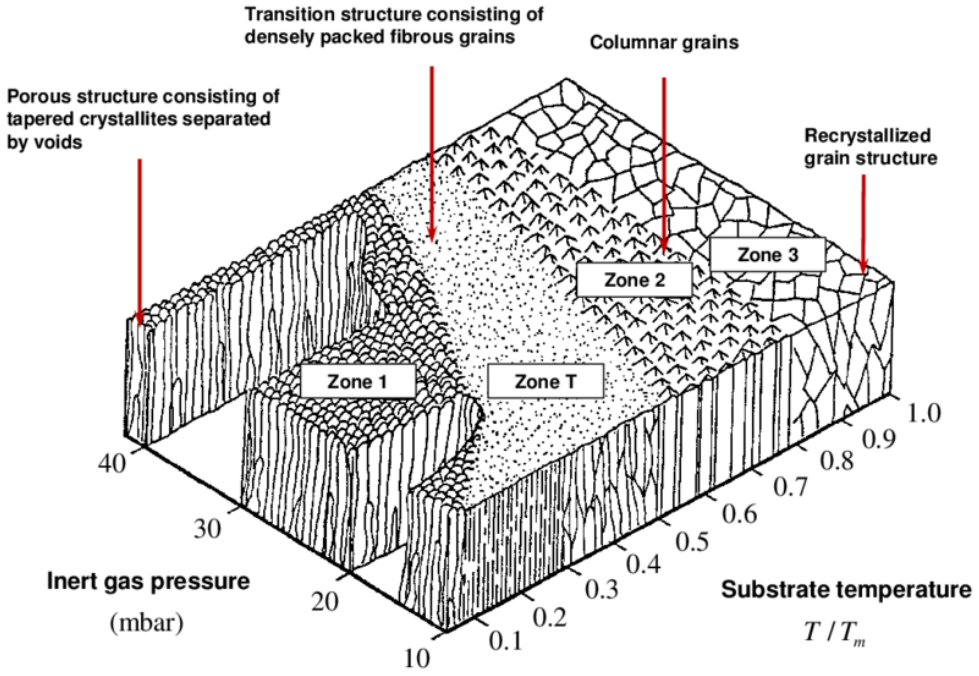

Figure 4.3: Thornton structure zone model. Adapted from Thornton (1977) showing surface structure dependence on Inert gas pressure and Substrate Temperature [78].

Different seed layers were examined in this work including Ru, Pt and Cu. The thickness of the 1st layer was 8 nm with pressure of 3 mTorr and the second layer was 12 nm with pressures in this work varying from 5 to 30 mTorr. An AF layer was deposited immediately after the second Ru layer. The antiferromagnet used was IrMn because of its high anisotropy constant and effective coupling to the Ferromagnet. The thickness and pressures of the IrMn was varied to study if I could achieve the phenomenon and the (111) planes formed at perpendicular direction were taken into consideration. Then the FM was deposited with high perpendicular anisotropy and hexagonal structure which is CoCrPt-SiO_2. Silica tends to segregate to the grain boundaries creating the voided structure. The thicknesses and pressures of this layer was varied as well accordingly. In some cases when the desired exchange bias was not achieved a Co interlayer was inserted between the seed layer and the antiferromagnet. The concept of this idea was that the 2 atom thick Co interlayer could induce a perpendicular spin orientation on the Mn ions of the IrMn [19] which would then couple to the CoCrPt inducing an exchange bias in the conventional storage layer. After the FM a Ta capping layer was deposited of 5 nm thickness and 3 mTorr pressure to protect the media from oxidation. The full stack is shown schematically in Figure 4.4

Capping layer	5 nm	3 mTorr
Recording layer	varied	varied
Antiferromagnetic layer	5,6 nm	15,20,30 mTorr
Seed layer high pressure	12 nm	30 mTorr
Seed layer low pressure	8 nm	3 mTorr
Buffer layer	5 nm	3 mTorr
Substrate	-	-

Figure 4.4: Typical multilayer structure produced by sputtering to be studied as perpendicular recording exchange biased media.

4.3 Deposition pressure optimisation

The first step in the attempt to produce the desired multilayer structures was to optimize the deposition pressure for the second Ru seed layer so as to get squared loops and segregated structure. The initial structure was like Figure 4.5:

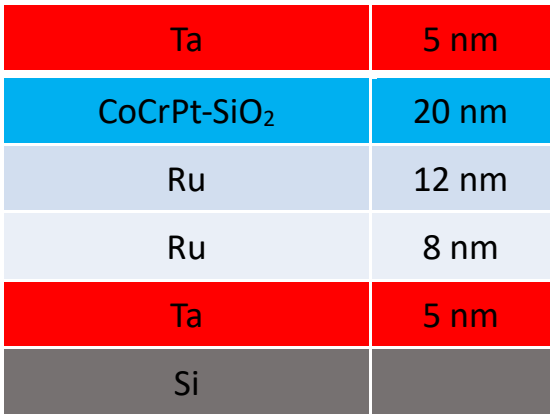

Figure 4.5 Schematic diagram of the initial structures of samples

The deposition was repeated four times to ensure the reproducibility of the results. The two important criteria for perpendicular recording media when studying the hysteresis loops are coercivity and squareness. High coercivity, more than 10 kOe, is required for HAMR applications because of the relationship between the magnetocrystalline anisotropy constant K_U and thermal stability. As K_U increases the grain size can be reduced and therefore a high density can be achieved. High squareness is required to generate a high output signal. For abbreviation, the data gathered and the loops from one deposition are presented, which show the dependence of deposition pressure on the properties of the loop. Room temperature hysteresis loops were taken with an AGFM to have a quick qualitative estimation of the properties. All four depositions showed that the optimum pressure was 15 mTorr.

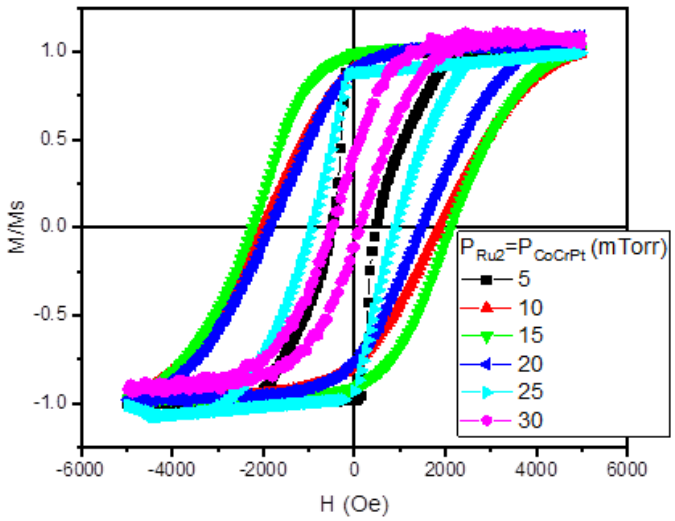

Figure 4.6: AGFM room temperature hysteresis measurements to estimate the optimal deposition pressure for both 2nd Ru layer and FM layer.

Sample	S4.1	S4.2	S4.3	S4.4	S4.5	S4.6
Pressure (±1mTorr)	5	10	15	20	25	30
Deposition Rate of CoCrPt (±0.01nm/sec)	0.1	0.08	0.05	0.03	0.02	0.01
H_c (±5Oe)	485	1940	2170	1670	918	312
Squareness (±2%)	97.2	90.6	99.2	90.6	87.5	42.6

Table 4: Magnetic properties of samples with structure shown in figure 4.4

As shown in Table 4 the squareness remains high for all deposition pressures except for the 30 mTorr where it collapses. This is because the deposition rate was very low, almost 0.01 nm/sec, resulting in a poor crystallisation of the FM. As it can also be seen from Table 1 the process pressure of Ar gas is inversely proportional to the sputtering rate. For 15 mTorr squareness reaches its maximum with 99.2% which means that the induced perpendicular anisotropy is almost perfectly oriented at the c-axis of the hexagonal structure of the CoCrPt-SiO_2 layer. The segregation is achieved as mentioned earlier by the voided structure of the second Ru layer, since the deposited Ru atoms are more scattered at higher process pressures resulting in a decrease in the migration energy and migration distance. With good segregation and low RKKY coupling, the level of cooperative reversal is reduced increasing the coercivity. This seems to be the dominating mechanism for the samples deposited at 10, 15 and 20 mTorr, in figure 4.6. The smaller slope of these loops indicates also this exchange de-coupling

because of the silica between the grains. The 15 mTorr though seems to have a little stronger coupling than the other two. On the other hand, when segregation is not perfect, intergranular exchange coupling will tend to keep the grains aligned parallel while dipolar effects will have the opposite effect. The role of exchange coupling in the hysteresis loops is complex. Initially, grains are kept aligned by this coupling which results in an increase in the squareness of the loops. However, when one grain reverses, maybe because of low anisotropy, this results in cooperative reversal as the grains are coupled. This increases the remanence but reduces the coercivity and happens for samples with higher deposition pressures like the one with 25 mTorr deposition pressure. After that at the 30 mTorr the perpendicular anisotropy and squareness collapse as mentioned before. These results are complementary to previous work by Kelvin Elphick [22], showing optimum pressures of 30 mTorr for the FM layer mainly because the work was done in the Hitus system several years ago and some settings on the chamber might have changed.

4.4 FM thickness optimisation

The thickness of the FM layer was optimised next. So, in this deposition the pressure of the 2nd Ru layer was kept at 30 mTorr to achieve the desired segregation and of the FM at 15 mTorr and the thickness of the FM was varied at t_{FM}= 20, 15, 12, 10, 6 and 4 nm. The initial loops were obtained with an AGFM and for this set of measurements the characteristic table for the values is given. This series of samples was also characterized with an XRD for the structural properties to be studied and whether the CoCrPt was layered properly above the 2nd Ru layer creating a match of the c-axis. The structure of the samples was the same as Figure 4.5.

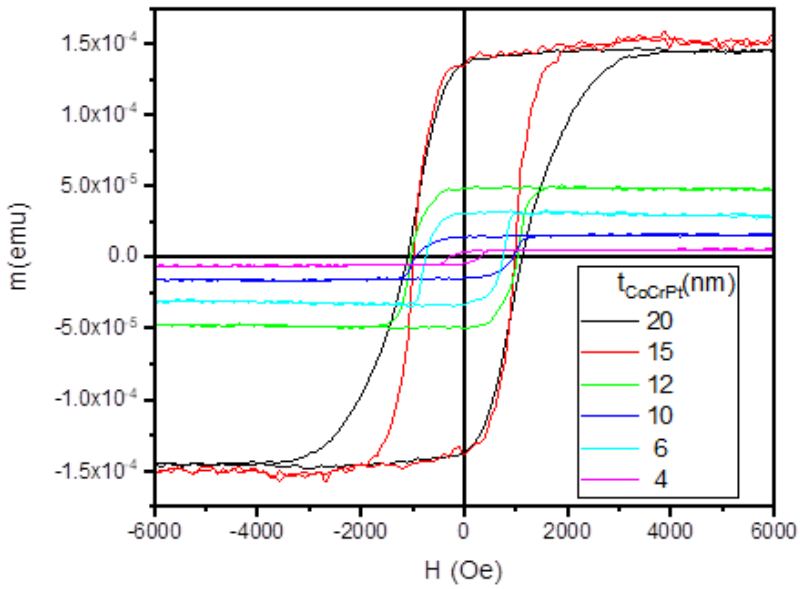

Figure 4.7: Hysteresis loops for different thicknesses of the FM showing a dependence of the saturation on the FM thickness.

Sample	8.1	8.2	8.3	8.4	8.5	8.6
t_{CoCrPt} (±0.2nm)	20	15	12	10	6	4
H_c (±5Oe)	1110	979	1030	947	748	305
Squareness (±2%)	93.8	90.7	97.6	87.7	98.8	72.1
M_S (±0.05×10^{-4} emu)	1.45	1.51	0.47	0.163	0.302	0.056

Table 5: Magnetic properties of samples of figure 4.4 with variation of thickness of the FM layer.

As it can be seen from Table 5 by reducing the FM layer thickness, a reduction of the saturation magnetisation M_S was noticed, as one could expect because the FM grains become smaller and smaller although there are still some anomalies in the measurements such as that the 15 nm sample Ms is the same with that of the 20 nm and the 6 nm is higher than the 10 nm but the general trend is clear. On the other hand, the squareness remained at acceptable high levels, above 90% even for the 6 nm. This means that the perpendicular anisotropy for the thin layers was not lost. A possible critical thickness was the 4 nm where the properties vanished. The shape of the loops also in some cases look different despite having the same coercivities. From the shapes of the loops one can get valuable information for the dominant reversal mechanism in the films. As mentioned previously in Theory chapter 2.10 when the grains are perfectly segregated reversal of each single domain grain is described by the

Stoner-Wohlfarth theory as the silica results in exchange decoupling between grains and this happens for films with lower thicknesses. The reversal then is dominated by the grains with the lowest energy barriers. On the other hand, if there is exchange coupling between grains in a magnetic thin film, the reversal is dominated by domain wall processes which changes the shape of the loop, giving higher slopes and this is the case for the films with higher thicknesses. Reversal proceeds via the initial nucleation of one or more domains followed by a fairly quick propagation impeded by domain wall pinning. The main factor affecting the coercivity will be the nucleation of the reverse domains which is controlled by many factors.

The structural properties were also studied at this series of samples with an XRD graph given in figure 4.8. As one can see from the figure, I focused at the pick around 42^0 where a merge of the two picks of Ru and CoCrPt is observed. Based on the International Centre for Diffraction Data (ICDD) the Ru (002) pick of its hexagonal structure should be located at 42.2^0. The (002) peak for CoCrPt-SiO_2 hexagonal structure is located at 42.8^0. As it can be seen from figure 4.8 for all thicknesses of FM a broad pick was observed from the merging of the 2 peaks at 42.2^0 indicating that the FM followed the texture of the underlying Ru layer developing its structure along the c-axis. Another observation is that as the thickness decreases the peak gradually reduces its intensity as expected.

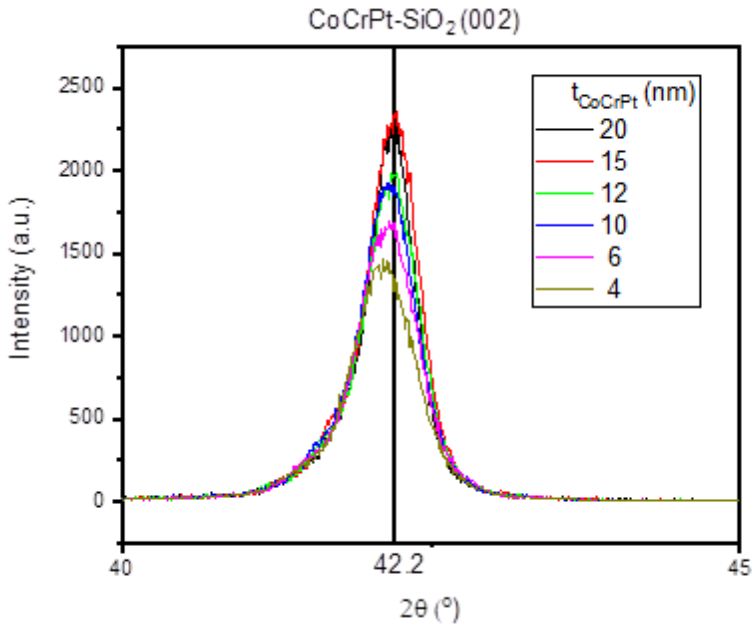

Figure 4.8: XRD graph focusing on the 42.2^0 peak with varying the thickness of the FM layer. A small shift is noticed for smaller thicknesses, which is though below 0.1°.

A further structural analysis can be made from figure 4.8 through the Scherrer equation, which gives for the grain size:

$$D_{grain} = \frac{0.9\,\lambda_0}{\beta cos\theta}(nm) \qquad (4.4.1)$$

where 0.9 is a shape factor, λ_o= 0.154059 nm the Xray wavelength β is the full width half maximum (FWHM) of the peak in radians, and θ is the Bragg angle. So, through the analysis one can get the following table for the different thicknesses of the FM layer.

sample	t_{CoCrPt} (nm)	θ (°)	β (°)	β (rads)	Dgrain (nm)
8,1	20	21,1	0,43	0,007501	19,81
8,2	15	21,1	0,48	0,008373	17,75
8,3	12	21,1	0,53	0,009246	16,07
8,4	10	21,1	0,55	0,009594	15,49
8,5	6	21,1	0,57	0,009943	14,95
8,6	4	21,1	0,59	0,010292	14,44

Table 6: Table for the analysis of grain size diameter from the data obtained from figure 4.8 and its dependence on FM layer thickness

As it can be seen there is an almost linear reduction of the median grain size of the FM layer with the reduction of its thickness respectively. The estimation of the grain diameter though doesn't agree with previous work where the median grain size was estimated from TEM and was found to be around 7 nm [22], meaning it was previously found reduced by half. Smaller grains though with reduction of thickness means they can switch more easily, something which agrees with the reduction of coercivity from Figure 4.7.

4.5 Testing Pt as a seed layer

The next step in the attempt for the desired structure to be created and studied for any possible alternatives, was to study the Pt as a seed layer. Pt is known for its face cubic centered (fcc) structure which can easily replace the hcp structure of Ru. This is due to the fact that the basal plane of the hexagonal (hcp) (002) is identical to the fcc (111) plane as shown in Figure 4.9.

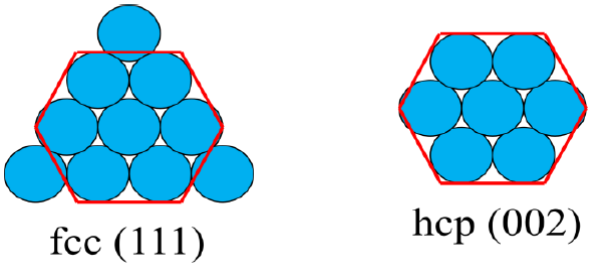

Figure 4.9: Schematic diagram of the two complementary structures used as seed layers[22].

Firstly, the procedure of the pressure optimization was repeated like in the Ru case with a structure of the multilayer given by figure 4.10

Ta	5 nm
$CoCrPt\text{-}SiO_2$	20 nm
Pt	12 nm
Pt	8 nm
Ta	5 nm
Si	-

Figure 4.10: Schematic diagram of the multilayer studied for optimization of Pt as a seed layer

In this case the optimum pressure was found to be 30mTorr with the loops obtained by AGFM for a quick qualitative estimation. In Figure 4.10, the normalized loops are given to be easier to compare them. The pressure of Ta and 1st Pt seed layers was chosen to be at 3 mTorr while the CoCrPt-SiO_2 was kept steady at 15mTorr and the 2nd Pt layer was varied from 5 to 30 mTorr with a step of 5 mTorr.

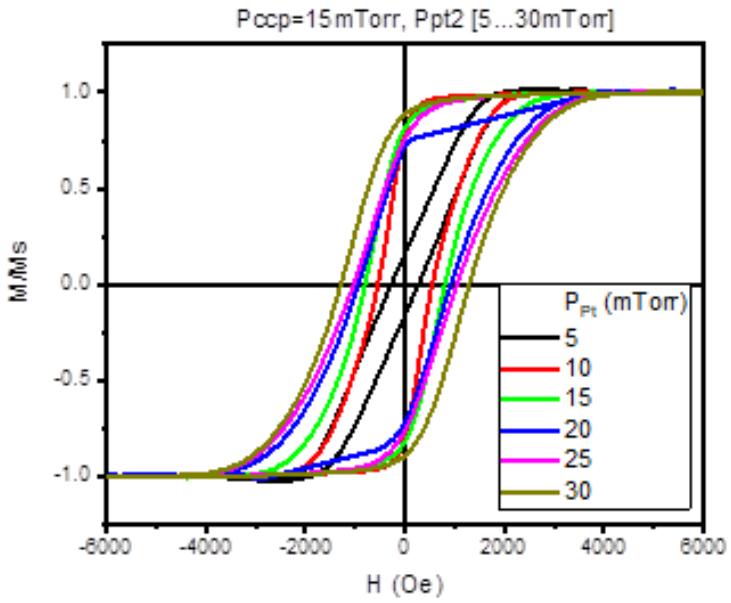

Figure 4.11: AGFM hysteresis loops for different deposition pressures of 2nd Pt layer in structure given by Figure 4.9

Table 7 shows the results indicating squareness becoming higher with pressure increase and coercivity following the same trend although the values are lower comparing to the Ru results. This is because the structures of seed layer and FM are not perfectly aligned since the structure is transcending from fcc to hcp. From the shape of the loops in this case, one can conclude that the exchange coupling between the grains, mainly because of RKKY coupling reduces with deposition pressure increase. The level of cooperative reversal, due to the segregation from the silica in the boundaries of the grains, is reduced resulting in higher coercivities. The dominating reversal mechanism appears to be the Stoner-Wohlfarth independent grain reversal as the slopes decrease. For 5 and 10 mTorr deposition pressures the perpendicular anisotropy cannot build up yet for the Pt seed layer while the 30mTorr seems to have the optimum characteristics as mentioned before.

Sample	9.1	9.2	9.3	9.4	9.5	9.6
Ppt_2(± 1mTorr)	5	10	15	20	25	30
H_c (± 5Oe)	276	546	803	931	1040	1290
Squareness (± 2%)	16	79.4	81.8	72.4	75.8	89.1

Table 7: Values of Squareness and coercivity for different deposition pressures of the 2nd Pt seed layer

After that, the same step as with the Ru case was made, by producing a series of samples with different thicknesses of the FM while keeping the deposition pressure of the 2nd Pt layer constant at its optimum value meaning 30 mTorr. There were observed two peaks in this case one at 39.6^0 for Pt (111) and one at 42.2^0 for CoCrPt-SiO_2 as before. The latter peak was broader and for lower thicknesses almost flat as seen in figure 4.12.

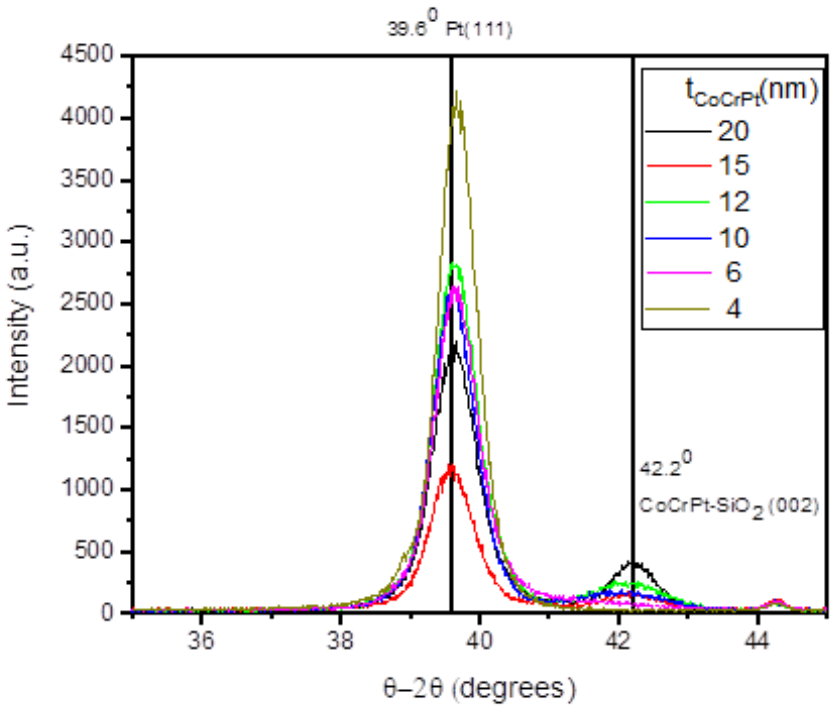

Figure 4.12: XRD graph for peak detection of FM and Pt seed layers as the thickness of the CoCrPt decreases.

The two trends noticed in this graph is that while I increase the thickness of the FM layer, in one hand the (002) peak of the ferromagnet increases as well but the texture of the Pt (111) seems to be supressed by the higher thicknesses of the FM overlayer resulting at lower intensities. In order to evaluate further the magnetic properties of this series of samples

I took quick AGFM loops showing a slight decrease of coercivity with thickness reduction which is normal as the grains become smaller and an increase on the other hand of squareness. Table 8 shows the results synoptically and figure 4.13 shows the trend in absolute magnetisation terms m (emu).

Sample	10.1	10.2	10.3	10.4	10.5
t_{CoCrPt} (± 0.2nm)	20	15	12	10	6
H_c (± 5Oe)	908	836	807	673	447
Squareness (± 2%)	52.5	64	82	85.2	83.5

Table 8: Values of coercivity and squareness with reducing FM layers thickness for the Pt seed layer case.

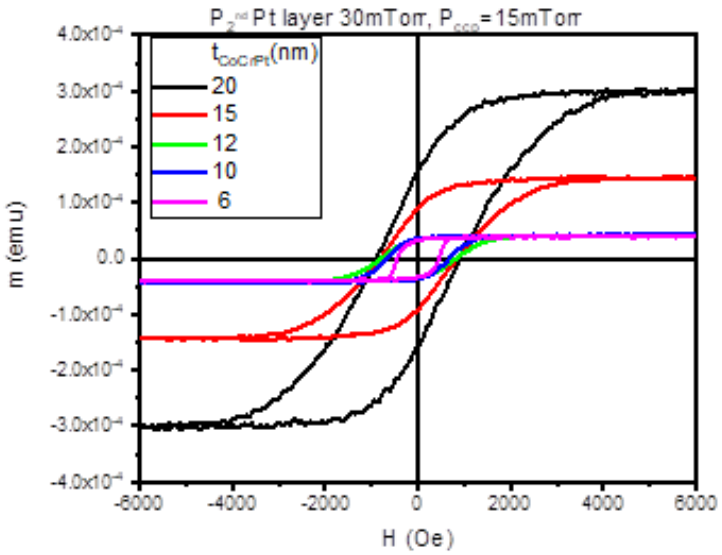

Figure 4.13: AGFM hysteresis loops for different thicknesses of the FM layer as the pressures of 2nd Pt layer and FM layer are kept steady at 30 and 15 mTorr respectively.

Regarding the shape of the loops here, although that the coercivity remains similar for all thicknesses, as the pressures remain the same, the slope of the loops seem to decrease with lower thicknesses transcending from domain wall processes, steeper transitions in higher thicknesses, to Stoner-Wohlfarth independent grain reversal with the ideal ones being the 10 and 12 nm.

4.6 Adding the antiferromagnetic layer

After the testing of complementary seed layers, the AF layer was added to the stack. The main issues I had to examine in this case was if the segregation would continue from the 2nd seed layer through the AF layer and then to the FM layer and secondly if the magnetic properties of the FM layer would remain intact with the perpendicular exchange bias (PEB) phenomenon possibly present. For that reason, a series of 6 samples was created with the thickness of the FM layer and the pressure of the AF layer as follows:

Ta	5 nm	3 mTorr
CoCrPt-SiO_2	6,10 nm	15 mTorr
IrMn	5 nm	15,20,30 mTorr
Pt	12 nm	30 mTorr
Pt	8 nm	3 mTorr
Ta	5 nm	3 mTorr
Si	-	-

Figure 4.14: Schematic diagram of stack studied for perpendicular exchange bias with different thicknesses and pressures.

In this case firstly the samples were examined structurally to see if all peaks can be observed for the present materials in the graph and 2 representative samples were taken with different thicknesses in the FM layer and pressure of AF layer at 20 mTorr. As shown in Figure 4.15 for the 10 nm FM layer there is a stronger peak for (002) CoCrPt while the Pt (111) peak is more supressed than that of the 6 nm FM thickness. Both results agree with the previous measurements. On the other hand, the (111) peak of the IrMn which was expected at 41.4^0 was not observed. This might be because when I did the θ-2θ scan the instrument was sensitive only to the planes parallel to the surface and not to the ones oriented vertically which were used for the PEB.

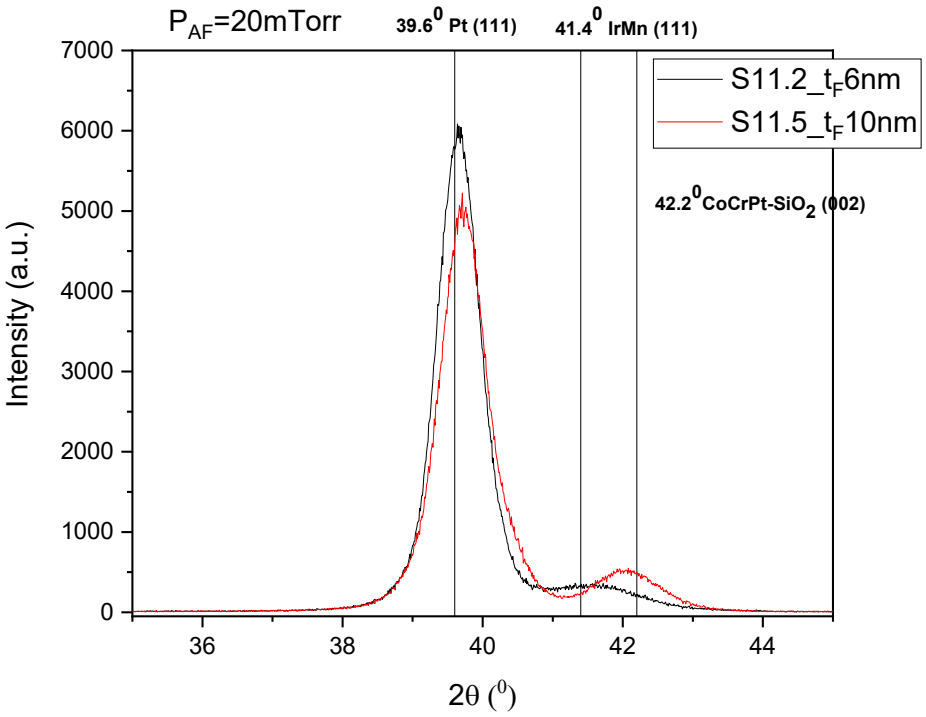

Figure 4.15: XRD graph for two representative samples of multilayer films with structures given by Figure 4.13

After that, a Lakeshore VSM 8600 was used to try to induce the perpendicular exchange bias to the system. The recipe in order to measure the perpendicular exchange bias was as follows:

The samples were heated to 450K in the presence of a 10 kOe out of plane magnetic field for 60 minutes. They were then field cooled to 100K and a hysteresis loop measured. Actually, the steps taken were first to rotate the sample to 90 degrees then to set the field to 10 kOe, then go to the temperature of 450K while the field was applied, wait for 60 minutes to set the antiferromagnet, then field cool the sample to 100K where the hysteresis loop was measured.

In the following graph I present the graph obtained from measurement of the six samples. It seems that the deposition pressure of the antiferromagnetic layer does not have an effect on the properties of the ferromagnet on top. This means that almost identical loops were obtained for the same FM layer thicknesses despite having different AF deposition pressures. If one focuses on each curve, one can observe that there is a difference of around -200 Oe between H_{c1} and H_{c2} for the 6 nm thickness than the 10 nm which is expected since

there is a dependence of $H_{ex} \sim 1/x_{FM}$ from equation 2.13.7. There could also be a small EB for the 10 nm thickness but since there are several points crossing the x axis, this difference could be within the error gap of ±100 Oe due to the high noise, because of the fact that the temperature that these measurements were obtained was at 100K. This temperature was not actually steady but was varying by ± 10K during the measurement, resulting in these noisy loops. The coercivity is higher for bigger thicknesses of the FM layer which is also expected as the grains are larger. After the introduction of the AF layer there is a reduction of squareness to 60% a reduction of around 30% from the multilayer without the AF layer. This is expected as the introduction of extra layers between the seed layer and the FM layer damages the perpendicular induced anisotropy.

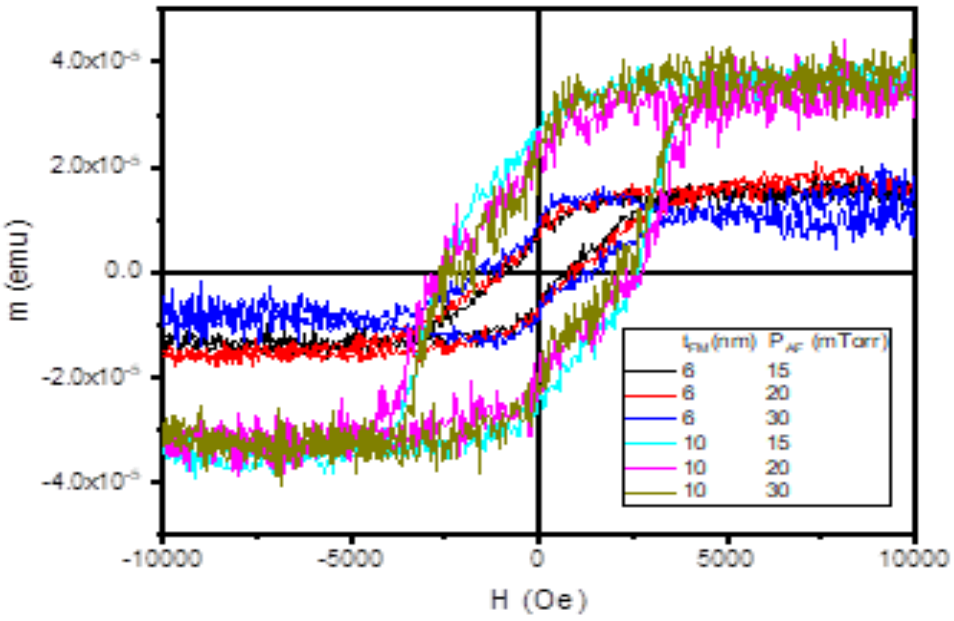

Figure 4.16: Hysteresis loops obtained at 100K after setting for 1 hour at 450K for samples with structure on figure 4.13.

On the table 9 the values of H_{C1}, H_{C2}, H_C and Hex from eq. 2.8.3 and 2.12.1 for each loop with different thickness of FM and pressure of AF is given. Regarding the shape of the loops and the coercivity one can see again that the dominant reversal mechanism in the films is better described by the Stoner-Wohlfarth theory for almost perfectly segregated grains. In particular the samples with lower thickness (6nm) of the FM layer have smaller slope than that with the 10nm thickness meaning that they are better segregated as expected. So, the

de-coupling of the grains is more effective and the grains do not reverse in an immediate manner but separately. The different pressures don't seem to have an effect on the squareness and the shape of the loops as they remain very similar. Although coercivity and exchange field seem to differ with deposition pressures variations.

Sample	S11.1	S11.2	S11.3	S11.4	S11.5	S11.6
t_{FM} (±0.2 nm)	6	6	6	10	10	10
P_{AF} (±1 mTorr)	15	20	30	15	20	30
H_{C1} (±100 Oe)	-1192	-973	-1767	-2583	-2611	-2611
H_{C2} (±100 Oe)	766	830	1146	2491	2302	1962
Hc (±100 Oe)	979	902	1457	2537	2457	2287
H_{ex} (±100 Oe)	213	72	311	46	155	325

Table 9: showing values of HC1, HC2 and Hex for the loops of figure 4.16

4.7 Mixed Ru-Pt seed layers

Another investigation during the materialization of this work was if it was possible to partially or completely replace the second layer in our system by combining two different materials. In the first attempt I used Ru and Pt layers as follows producing three samples:

Ru (8 nm)/ Ru (3 nm)/ Pt (9 nm), Ru (8 nm)/Pt (12 nm), Ru (8 nm)/Ru (9 nm)/ Pt (3 nm).

The Pressures of the triple seed layer were P (3, 15, 30 mTorr) respectively. The rest of the stack was similar to that of figure 4.14 with AF thickness = 6 nm and FM thickness = 10 nm. In the next figure I present analytically the stack:

Ta	5 nm	3 mTorr
CoCrPt-SiO_2	10 nm	15 mTorr
IrMn	6 nm	15 mTorr
Pt	(9,12,3) nm	30 mTorr
Ru	(3,0,9) nm	15 mTorr
Ru	8 nm	3 mTorr
Ta	5 nm	3 mTorr
Si	-	-

Figure 4.17: Schematic diagram with thickness and deposition pressures for the triple seed layer and full stack studied for that reason.

The samples were set at 450K for 1 hour and then measured at 100K with the Lakeshore VSM 8600. The recipe followed was the same as in section 4.6. Although no perpendicular exchange bias was noticed the results on that series of samples showed that I can safely combine these two materials as seed layers without damaging the magnetic properties of the stack. The transition from hcp Ru structure to fcc Pt structure came naturally as it was proved in previous sections while the combination of these elements results in a perfectly aligned structure, do not have a large effect on the properties of the FM and the AF underlayer and the squareness and coercivity remain at acceptable values. More particularly squareness is around 70% and coercivity around 1800 Oe which means that by using Ru as a seed layer instead of Pt and partially replacing it with Pt, better properties can be achieved. In figure 4.18 the three loops are shown.

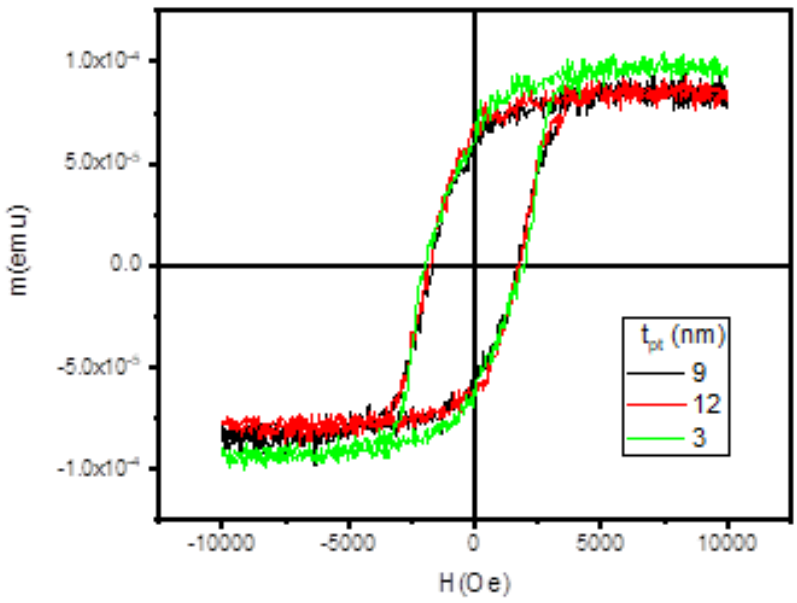

Figure 4.18: Hysteresis loops for alternating the thicknesses in a combined Ru/Ru/Pt triple seed layer

4.8 Mixed Ru-Cu layers

The same procedure was followed in order to test another supplementary seed layer and more specifically Cu. The three samples produced had again the structure:

Ru (8 nm)/Ru (3 nm)/Cu (9 nm), Ru (8 nm)/Cu (12 nm), Ru(8 nm)/Ru (9 nm)/Cu (3 nm) with pressures of 3/15/15 mTorr respectively. The 15mTorr was chosen as a deposition pressure for Cu as the 30 mTorr had a rate of 0.1 A/sec to 0.0 A/sec and it was not possible to sputter at this rate the layer. The stack followed the structure of Figure 4.16 but instead of Pt there was Cu with same thicknesses and with its fcc (111) structure. Again, the recipe followed for the measurements was given by section 4.6 with the loops being obtained at 100K. I obtained the graph 4.18 and, in this case, the magnetisation was normalised in order to be able to compare more easily coercivity and squareness. A change in coercivity was observed with the change in Cu thickness and specifically for the Ru (8 nm)/Cu (12 nm) dual layer an improvement on the properties. One can observe a small perpendicular exchange bias with results given in table 10. The values of H_C and H_{ex} were calculated by equations 2.8.3 and 2.12.1 respectively.

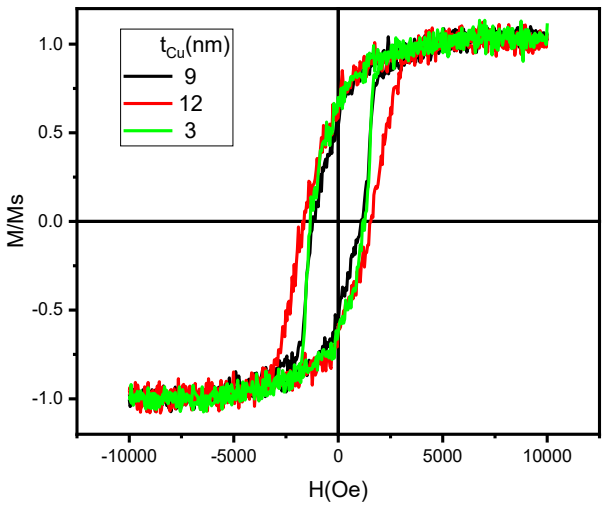

Figure 4.19: Hysteresis loops of three samples with alternating thicknesses of the triple seed layers Ru/Ru/Cu

Sample	S13.1	S13.2	S13.3
Cu thickness (±0.2nm)	9	12	3
Ru_2 thickness (±0.2nm)	3	0	9
Hc (±5Oe)	1164	1589	1290
Hex (±5Oe)	62	35	50
Squareness Ratio (±2%)	54	60	67

Table 10: Magnetic properties of a series of samples with alternating the thicknesses of a triple seed layer

The reduction of the squareness below 70% means that somehow the perpendicular anisotropy is lost when mixed seed layers are deposited and specifically the Cu on top of Ru meaning that the moments follow a more random orientation and they are not aligned perfectly perpendicular to the plane. An explanation for that is that by depositing many different materials one on top of the other might cause structural defects. The coercivity is smaller than in the mixed Ru-Pt case meaning that replacing Ru with Pt might be more favourable than with Cu.

4.9 Addition of Co interlayer

A final attempt to see if there was any perpendicular exchange bias was to introduce a Co interlayer between the 2nd seed layer and the antiferromagnetic layer so that the 2 atom thick Co interlayer could induce a perpendicular spin orientation on the Mn ions of the IrMn which would then couple to the CoCrPt inducing an exchange bias in the conventional storage layer as mentioned before. The resulting structure was as that in Figure 4.19 which consisted in total of seven layers. Several attempts were made to produce different series of samples with different thickness and deposition pressure of the Co interlayer. Both Pt and Ru were used as seed layers and the thicknesses of AF and FM ferromagnetic layers remained at optimum as mentioned in previous work by Kelvin Elphick [22].

Ta	5 nm	1.86 mTorr
$CoCrPt\text{-}SiO_2$	4 nm	1.86 mTorr
IrMn	6 nm	1.86 mTorr
Co	(0.6, 0.8) nm	1.86, 5 mTorr
Ru, Pt	12 nm	30 mTorr
Ru, Pt	8 nm	3 mTorr
Ta	5 nm	1.86 mTorr
Si	-	-

Figure 4.20: Multilayer structure including the Co interlayer for an attempt to establish the perpendicular exchange bias

In order to measure these systems, I used the Microsense Model 10 VSM because it was able to arrange the desired recipe for the measurement and measure at different temperatures faster. In order to see if there was any exchange bias, I measured at room temperature and 100K after setting the ferromagnet at 498K for 1 hour. The recipe followed to measure these samples were as follows:

The samples were heated to 450K in the presence of a 10 kOe out of plane magnetic field for 60 minutes. They were then field cooled to 298K and 100K and a hysteresis loop was measured. Actually, the steps taken here again were first to rotate the sample to 90 degrees then to set the field to 10 kOe, then go to the temperature of 450K while the field was applied, wait for 60 minutes to set the Antiferromagnet, then field cool the sample to 298K or 100K where the hysteresis loop was measured.

The loops showed a reduction in coercivity and squareness after the introduction of the Co interlayer and a small displacement of the loop was noticed. An example of the kind of loop obtained is given in the following figure:

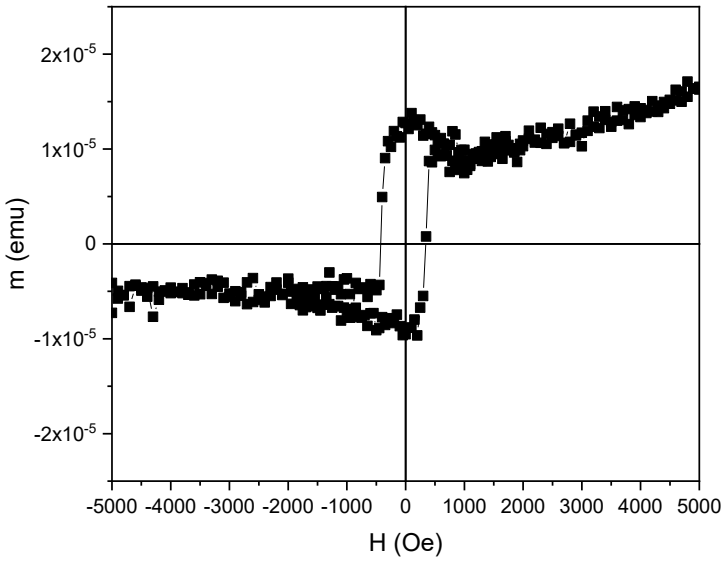

Figure 4.21: Example of hysteresis loop obtained at RT after the insertion of the Co interlayer

As one can see the squareness of the loop cannot be properly deducted from the loop as the diamagnetic component of the sample was large and after the deduction a small slope in saturation still remained. After that an estimation of around 96% squareness, can be made which seems very good for a sample with seven layers, meaning that the anisotropy remained oriented perpendicular to the plain and transferred from the seed layers through the Co layer and the AFM IrMn layer to the FM recording layer without particular losses. On the other hand, coercivity H_C and exchange field H_{ex} were determined by the values of H_{C1} and H_{C2} and calculated by the relations 2.8.3 and 2.12.1 respectively.

Sample	S15.2
H_{c1} (±5Oe)	-428
H_{c2} (±5Oe)	348
H_C (±5Oe)	388
H_{ex} (±5Oe)	40
Squareness Ratio (±2%)	96

Table 11: An estimation of the main parameters of the loop obtained after the introduction of the Co Interlayer in the multilayer film.

Comparisons with the samples before the Co addition are difficult to be made because the thickness of the FM recording layer was 4 nm which differed from that in section 4.6 and

the measurement was done with different instrument the Model 10 instead of the Lakeshore. Although some rough estimations can be given, considering that the squareness seemed to improve with the Co addition and the coercivity was reduced mainly because the thickness was reduced from 10 and 6 nm to only 4 nm. Moreover, exchange bias although smaller than the measurements without the Co interlayer it is of considerable amount taking into account that the measurement was done in room temperature and not at 100K. Finally, from the shape of the loop it can be estimated that the Co interlayer adds to the exchange coupling of the grains making the reversal more immediate and the slope almost 90 degrees. This doesn't mean though that the grains of the FM overlayer are not segregated but the Co atoms when reversed cause a steeper transition mechanism.

5. Conclusions and future work

The basic conclusions excluded from this work are regarding mainly the optimization of the structure and the efforts to detect the perpendicular exchange bias. The optimum deposition pressure for the ferromagnetic CoCrPt layer was found to be 15 mTorr. The thickness of the FM that was chosen to study the Exchange bias was 6 and 10 nm. Pt and Cu were proved to be good candidates for replacing the 2nd Ru seed layer either partially or completely. After adding the IrMn layer, there was a reduction in the values of coercivity and squareness although a maximum exchange bias of H_{ex}=325 Oe was detected at low temperatures (100K) without the need of the Co interlayer but this needs further investigation. The multilayer structures seemed stable and the properties of the FM reproducible. After the addition of the Co interlayer a small shift was detected with a perpendicular exchange bias of H_{ex}=40 Oe at room temperature but it is possible that at 100K the effect might be bigger as a proof of principle has been already introduced by Elphick et al [22]. Future work that could be undertaken in our laboratories is that the level of shearing of the loop and in fact the degree of shift of the loop, could be significantly enhanced by the insertion of a monolayer of Mn between the F and AF layers. It is possible that the use of such a Mn layer may have a similar effect on the systems under study here. It should be noted that the mechanism by which Mn causes this effect is not well understood. There are two possibilities, the first being that the Mn replaces a compositional deficiency in the IrMn arising from diffusional effects and the second being that the presence of the high moment Mn atoms leads to a magnetically stiffer interface with a stronger coupling between the FM and AF layers. However, this phenomenon was not observed in this study. Therefore, the interfacial effect of the Mn layer should be further investigated in future.

References

[1] D. Weller *et al.*, "A HAMR media technology roadmap to an areal density of 4 Tb/in2," *IEEE Trans. Magn.*, vol. 50, no. 1, 2014.

[2] Wikipedia, "Heat Assisted Magnetic Recording." [Online]. Available: https://en.wikipedia.org/wiki/Heat-assisted_magnetic_recording.

[3] M. L. Plumer, J. van Ek, and W. C. Cain, "New Paradigms in Magnetic Recording," vol. 67, no. 1, pp. 3353–3355, 2012.

[4] C. B. Rong *et al.*, "Size-dependent chemical and magnetic ordering in L10-FePt nanoparticles," *Adv. Mater.*, vol. 18, no. 22, pp. 2984–2988, 2006.

[5] D. Suess *et al.*, "Fundamental limits in heat-assisted magnetic recording and methods to overcome it with exchange spring structures," *J. Appl. Phys*, vol. 117, p. 163913, 2015.

[6] Y. Tanaka and H. T., "Perpendicular recording with high squareness CoPtCrO media," *J. Magn. Magn. Mat.*, vol. 235, pp. 256–258, 2001.

[7] K. Elphick, G. Vallejo-Fernandez, T. J. Klemmer, J.-U. Thiele, and K. O'grady, "HAMR media based on exchange bias," *Appl. Phys. Lett*, vol. 109, p. 52402, 2016.

[8] Wikipedia, "Segregation (materials science)." [Online]. Available: https://en.wikipedia.org/wiki/Segregation_(materials_science).

[9] J. J. Shea, *Modern magnetic materials - principles and applications [Book Review]*, 2000th ed., vol. 21, no. 4. New York: Wiley-Interscience Publications, 2005.

[10] P. S. Keatley, "Time-Resolved Magneto-Optical Investigations of Picosecond Magnetisation Dynamics in Arrays of Non-Ellipsoidal Ferromagnetic Nano-Elements," no. June, 2008.

[11] M.N.Rudden and J.Wilson, *Elements of Solid State Physics*. Nedw York: Wiley-Interscience Publications, 1993.

[12] D. C. Jiles, *Introduction to Magnetism and Magnetic Materials*, Second. .

[13] J. R. Hook and H. . Hall, *Solid State Physics*. New York: Wiley-Interscience Publications, 1991.

[14] M. M. Kane, "Fabrication and characterization of perpendicular magnetic anisotropy thin-film CoCrPt grown on a Ti underlayer," MIT, 2015.

[15] N. A. Usov, "Ferromagnetic resonance in thin ferromagnetic film with surface anisotropy," *J. Magn. Magn. Mater.*, vol. 474, pp. 118–121, 2019.

[16] S. M. Rezende, J. A. S. Moura, F. M. De Aguiar, and W. H. Schreiner, "Ferromagnetic resonance of Fe(111) thin films and Fe(111)/Cu(111) multilayers," *Phys. Rev. B*, vol. 49, no. 21, pp. 15105–15109, 1994.

[17] R. Mattheis and G. Quednau, "Determination of the anisotropy field strength in ultra-thin magnetic films using longitudinal MOKE and a rotating field: the ROTMOKE method," *J. Magn. Magn. Mater.*, vol. 205, no. 2, pp. 143–150, 1999.

[18] W. Frost, “Perpendicular Anisotropy in Heusler Alloy Thin Films for CPP-GMR Devices,” 2018.

[19] S. Emori and G. S. D. Beach, “Optimization of out-of-plane magnetized Co/Pt multilayers with resistive buffer layers,” *J. Appl. Phys.*, vol. 110, no. 3, p. 033919, 2011.

[20] C. W. Barton and T. Thomson, “Magnetisation reversal in anisotropy graded Co/Pd multilayers,” *J. Appl. Phys*, vol. 118, p. 63901, 2015.

[21] M. Vopsaroiu, G. Vallejo Fernandez, M. J. Thwaites, J. Anguita, P. J. Grundy, and K. O’grady, “Deposition of polycrystalline thin films with controlled grain size,” *J. Phys. D Appl. Phys. J. Phys. D Appl. Phys*, vol. 38, pp. 490–496, 2005.

[22] K. Elphick, “Heat Assisted Magnetic Recording Media Based on Exchange Bias,” 2016.

[23] G. Manginas, “Study of Exchange bias in submicron structures of the NiFe/IrMn system,” NTUA, 2007.

[24] E. Fields, “The Hysteresis Loop and Magnetic Properties,” 2017. [Online]. Available: https://www.nde-ed.org/EducationResources/CommunityCollege/MagParticle/Physics/HysteresisLoop.htm.

[25] B. . Cullity, *Introduction to magnetic Materials*. Addison-Wesley Publishing, 1972.

[26] M. A. RUDERMAN AND C. KITTEL, “Indirect Exchange Coupling of Nuclear Magnetic Moments by Conduction Electrons*,” vol. 96, no. 3, pp. 72–75, 1954.

[27] T. Kasuya, “A Theory of Metallic Ferro- and Antiferromagnetism on Zener’s Model,” *Prog. Theor. Phys.*, vol. 16, no. 1, pp. 45–57, 2006.

[28] R. W. C. and K. O. G. J Chureemart, P Chureemart, R Evans, “Magnetic orientation in advanced recording media,” *J. Phys. D Appl.*, vol. 44, pp. 455002–455006, 2011.

[29] H. Eleuch, *Magnetoresistance of ultrathin Co / Au (111) multilayers*, no. January 2010. 2014.

[30] E. C. Stoner and E. P. Wohlfarth, “A mechanism of magnetic hysteresis in heterogeneous alloys,” 1947.

[31] S. Fähler and L. Schultz, *Encyclopedia of Materials: Science and Technology*. 2001.

[32] G. V. Fernandez, “Grain Size Effects in Polycrystalline Exchange Biased Systems by,” no. December, 2006.

[33] L. E. Fernández-Outón, K. O’Grady, and M. J. Carey, “Thermal phenomena in IrMn exchange biased systems,” *J. Appl. Phys.*, vol. 95, no. 11 II, pp. 6852–6854, 2004.

[34] M. Tsunoda, K. ichi Imakita, M. Naka, and M. Takahashi, “L12 phase formation and giant exchange anisotropy in Mn3Ir/Co-Fe bilayers,” *J. Magn. Magn. Mater.*, vol. 304, no. 1, pp. 55–59, 2006.

[35] I. Tomeno, H. N. Fuke, H. Iwasaki, M. Sahashi, and Y. Tsunoda, “Magnetic neutron scattering study of ordered,” *J. Appl. Phys.*, vol. 86, p. 3853, 1999.

[36] E. Fulcomer and S. H. Charap, “Temperature and frequency dependence of exchange anisotropy effects in oxidized NiFe films,” *J. Appl. Phys.*, vol. 43, p. 4184, 1972.

[37] R. Coehoorn, *Handbook of Magnetic Materials*, vol. 15. Amsterdam, 2003.

[38] W. H. Meiklejohn, “Exchange Anisotropy—A Review,” *J. Appl. Phys.*, vol. 33, no. 3, pp. 1328–1335, Mar. 1962.

[39] I. K. Schuller and J. Nogués, “Exchange bias,” *J. Magn. Magn. Mater.*, vol. 192, pp. 203–232, 1999.

[40] J. Nogués *et al.*, “Exchange bias in nanostructures,” *Phys. Rep.*, vol. 422, no. 3, pp. 65–117, 2005.

[41] A. P. Malozemoff, “Random-field model of exchange anisotropy at rough ferromagnetic- antiferromagnetic interfaces,” *Phys. Rev. B*, vol. 35, no. 7, pp. 3679–3682, 1987.

[42] I. Yoseph and M. Shang keng, “Random-Field Instability of the Ordered State of Continuous Symmetry~,” *Phys. Rev. Lett.*, vol. 35, no. 21, pp. 1399–1401, 1975.

[43] M. Kiwi Tichauer, “Topical Review: Exchange Bias Theory,” vol. 234, pp. 584–595, 2001.

[44] M. D. McMichael and S. R., “Temperature dependence of exchange bias in polycrystalline ferromagnet-antiferromagnet bilayers,” *Phys. Rev. B - Condens. Matter Mater. Phys.*, vol. 60, no. 18, pp. 12950–12956, 1999.

[45] M. D. Stiles and R. D. McMichael, “Model for exchange bias in polycrystalline ferromagnet-antiferromagnet bilayers,” *Phys. Rev. B - Condens. Matter Mater. Phys.*, vol. 60, no. 18, pp. 12950–12956, 1999.

[46] A. E. Berkowitz and K. Takano, “<Exchange Anisoropy a Review.Pdf>,” vol. 200, pp. 552–570, 1999.

[47] H. Kanso, R. Patte, V. Baltz, and D. Ledue, “Influence of finite-size and edge effects on the exchange-bias properties of ferromagnetic/antiferromagnetic nanodots: Granular Monte Carlo investigation,” *Phys. Rev. B*, vol. 99, no. 5, pp. 1–7, 2019.

[48] D. V. Dimitrov, K. Unruh, G. C. Hadjipanayis, V. Papaefthymiou, and A. Simopoulos, “Defect clusters in Fe1−xO and their ferrimagnetic properties,” *J. Appl. Phys.*, vol. 87, no. 9, pp. 7022–7024, 2002.

[49] N. C. Koon, “Calculations of Exchange Bias in Thin Films with Ferromagnetic–Antiferromagnetic Interfaces,” pp. 4865–4868, 1997.

[50] K. O’Grady, L. E. Fernandez-Outon, and G. Vallejo-Fernandez, “A new paradigm for exchange bias in polycrystalline thin films,” *J. Magn. Magn. Mater.*, vol. 322, no. 8, pp. 883–899, 2010.

[51] G. Vallejo-Fernandez, L. E. Fernandez-Outon, and K. O’Grady, “Measurement of the anisotropy constant of antiferromagnets in metallic polycrystalline exchange biased systems,” *Appl. Phys. Lett.*, vol. 91, no. 21, pp. 1–4, 2007.

[52] H. Xi, “Theoretical study of the blocking temperature in polycrystalline exchange biased

bilayers," *J. Magn. Magn. Mater.*, vol. 288, pp. 66–73, 2005.

[53] M. Grimsditch, A. Hoffmann, P. Vavassori, H. Shi, and D. Lederman, "Exchange-Induced Anisotropies at Ferromagnetic-Antiferromagnetic Interfaces above and below the Néel Temperature," *Phys. Rev. Lett.*, vol. 90, no. 25, p. 4, 2003.

[54] and K. O. G. Vallejo-Fernandez, N. P. Aley, J. N. Chapman, "Measurement of the attempt frequency in antiferromagnets," vol. 222505, no. December, pp. 1–4, 2010.

[55] C. Y. Tsai, J. H. Hsu, P. Saravanan, and K. F. Lin, "Study on the occurrence of spontaneously established perpendicular exchange bias in Co49Pt51/IrMn bilayers," in *Journal of Applied Physics*, 2014.

[56] J. Y. Chen, N. Thiyagarajah, H. J. Xu, and J. M. D. Coey, "Perpendicular exchange bias effect in sputter-deposited CoFe/IrMn bilayers," *Cit. Appl. Phys. Lett.*, vol. 104, p. 7717, 2014.

[57] K. Srinivasan, S. N. Piramanayagam, and R. Sbiaa, "Antiferromagnetic iridium manganese based intermediate layers for perpendicular magnetic recording media," *Appl. Phys. Lett*, vol. 93, p. 72503, 2008.

[58] K. Elphick, K. O'Grady, and G. Vallejo-Fernandez, "Perpendicular Exchange Bias in $(Co/Pt)_n$ Multilayers," *IEEE Trans. Magn.*, pp. 1–6, 2019.

[59] G. M. B. Castro, L. C. C. M. Nagamine, J. Geshev, E. B. Saitovich, and J. E. Schmidt, "Perpendicular exchange bias in IrMn/Pt/[Co/Pt] 3 multilayers with cone magnetization," 2011.

[60] Qintong Zhang *et al.*, "Perpendicular Exchange Bias of $[Pt/Co]_5$/IrMn Multilayers on Self-Organized Hexagonally Patterned Nanodots," *IEEE Magn. Lett.*, vol. 6, pp. 1–4, 2015.

[61] J. Wang, T. Omi, T. Sannomiya, S. Muraishi, J. Shi, and Y. Nakamura, "Strong perpendicular exchange bias in sputter-deposited CoPt/CoO multilayers," *Appl. Phys. Lett*, vol. 103, p. 42401, 2013.

[62] S. Takenoiri, K. Enomoto, Y. Sakai, and S. Watanabe, "Exchange-coupled IrMn/CoZrNb soft underlayers for perpendicular recording media," *IEEE Trans. Magn.*, vol. 38, no. 5 I, pp. 1991–1993, 2002.

[63] A. Hashimoto, S. Saito, N. Itagaki, and M. Takahashi, "Improvement of magnetic properties of granular perpendicular recording media by using a fcc nonmagnetic intermediate layer with stacking faults," *Appl. Phys. Lett*, vol. 89, p. 262508, 2006.

[64] H. Yuzuru, "Pt-Cr alloy intermediate layer for CoCrPt-SiO2 granular perpendicular recording media," *IEEE Trans. Magn.*, vol. 42, no. 10, pp. 2336–2338, 2006.

[65] B. G., *Sputtering by particle bombardment*. 1982.

[66] R. D. A. P.J. Kelly, "Magnetron sputtering: a review of recent developments and applications," *Vacuum*, vol. 56, pp. 159–172, 2000.

[67] K. O. M. Vopsaroiu*, M. J. Thwaitesa, G. V. Fernandez, S. Lepadatu, "Grain size effects in metallic thin films prepared using a new sputtering technology," *J. Optoelectron.*

Adv. Mater., vol. 7, no. 5, pp. 2713–2720, 2005.

[68] P. W. H. Bragg and W. L. Bragg, “The Reflection of X-rays by Crystals,” vol. 17, pp. 428–438, 1913.

[69] K. Inaba, S. Kobayashi, K. Uehara, and A. Okada, “High Resolution X-Ray Diffraction Analyses of (La , Sr) MnO 3 / ZnO / Sapphire (0001) Double Heteroepitaxial Films,” *Adv. Mater. Phys. Chem.*, vol. 3, no. April, pp. 72–89, 2013.

[70] K. O’grady, V. G. Lewis, D. P. E. Dickson, R. Goldfarb, and D. P. E. Dickson@, “An alternating-gradient magnetometer (invited,” *Sample Magnetom. Rev. Sci. Instruments*, vol. 73, p. 548, 1993.

[71] P. J. Flanders, C. D. Graham, G. R. Ashcroft, and I. Terry, “Resonant properties of a Flanders alternating gradient field magnetometer: influence of temperature and magnetic moment Related content DC and low-frequency magnetic measuring techniques Resonant properties of a Flanders alternating gradient field magnetometer: influence of temperature and magnetic moment,” *Meas. Sci. Technol*, vol. 17, pp. 2263–2268, 2006.

[72] W. Frost, “Probe Repair for the AGFM,” pp. 1–3.

[73] P. J. Flanders, “Versatile and Sensitive Vibrating-Sample Magnetometer Review of Scientific Instruments,” *Cit. J. Appl. Phys.*, vol. 63, p. 4740, 1988.

[74] “Microsense VSM model 10 Picture.” [Online]. Available: https://www.azosensors.com/images/equipments/EquipmentImage_334.jpg.

[75] “Lakeshore VSM Series 8600.” [Online]. Available: https://www.lakeshore.com/products/categories/overview/material-characterization-products/vsm-systems/8600-series-vsm.

[76] T. J, “Influence of apparatus geometry and deposition conditions on the structure and topography of thick sputtered coatings,” *J. Vac. Sci. Technol*, vol. 11, no. 4, p. 666, 1974.

[77] J. Z. Shi *et al.*, “Influence of dual-Ru intermediate layers on magnetic properties and recording performance of CoCrPt-SiO2perpendicular recording media,” *Appl. Phys. Lett.*, vol. 87, no. 22, pp. 1–3, 2005.

[78] J. J. Fernandez, “Tuning the thermal conductivity of polycrystalline lms via multiscale structural defects and strain Jury :,” vol. 33, no. 1, 2015.